

DIAGENESIS AND FORMATION STRESS IN FRACTURE CONDUCTIVITY OF SHALY
ROCKS; EXPERIMENTAL-MODELLING APPROACH IN CO₂-ROCK INTERACTIONS

A Dissertation

Submitted to the Graduate Faculty of the
Louisiana State University and
Agricultural and Mechanical College
in partial fulfilment of the
requirements for the degree of
Doctor of Philosophy

in

The Craft & Hawkins Department of Petroleum Engineering

by

Abiola Olukola Olabode
B.S., Obafemi Awolowo University, 2008
M.S., Louisiana State University, 2012
December 2017

To my mother, Adeyinka, who lived but for a while

ACKNOWLEDGEMENTS

My sincere gratitude goes to the following; Dr. Craig M Harvey for graciously serving as chair of my doctoral research committee; my committee members, Dr. Mayank Tyagi, Dr. Paulo Waltrich, Dr. Dandina Rao and the graduate school Dean's Representative Dr. Chao Sun for their invaluable contributions and criticisms that have given shape to this work. I want to specially thank the Craft and Hawkins Department of Petroleum Engineering for availing me the multi-year resources that made this project a success. I appreciate Wanda LeBlanc, LSU AgCenter, Donmei Cao, and the LSU SIF staff members for assisting with post experimental data analysis. I also thank George Ohrberg for helping with computing needs in data acquisition and Fenelon Nunes for helping with laboratory ware purchases and maintenance. The financial support of the SPE and the GDL Foundation is kindly acknowledged. Thanks to LSU Graduate School for the Dissertation Year Fellowship that saw me through my final semesters.

I am appreciative of colleagues with whom I shared and gained useful ideas. They include Nnamdi Agbasimalo, Chukwudi Chukwudozie, Wei Wang, Gbola Afonja, Paulina Mwangi, Louise Smith, Arome Oyibo, Darko Kupresan, Kolawole Bello, Ruixuan Guo and Hui Du to mention a few.

Special thanks to my wife, Omoefe Kio-Olabode, for her unrelenting support throughout my graduate studies. Your children shall call you blessed. To our son, Mark Olayinka, thanks for beaming light on to our world at this junction in our lives.

I deeply appreciate the fervent prayers and support of my father and siblings; Oladepo Olabode, Titilola Akinyemi and Motunrola Olaiya. Thanks to my uncle, Jinmi Olabode and cousin, Tolu Olabode for always checking on us all these years. Also, special thanks to the Chapel on Campus for the edification of my inner man since I arrived at LSU.

G.1: Data for differential pressure across 25µm fractured core for flow-through experiment using Mancos shale	188
G.2: Data for differential pressure across 25µm fractured core for flow-through experiment using Marcellus shale	189
G.3: Data for differential pressure across 25µm fractured core for flow-through experiment using Pottsville shale.....	190
G.4: Data for differential pressure across 25µm fractured core for flow-through experiment using Wilcox shale	191
G.5: Data for differential pressure across 150µm fractured core for flow-through experiment using Mancos shale	192
G.6: Data for differential pressure across 150µm fractured core for flow-through experiment using Marcellus shale	193
G.7: Data for differential pressure across 150µm fractured core for flow-through experiment using Pottsville shale	194
G.8: Data for differential pressure across 150µm fractured core for flow-through experiment using Wilcox shale	195
H.1: Steps, equations and assumptions were made in calculating the fracture conductivity of the cores used during the experiments	196

A.14: Crushed shale samples, post-flooding with CO ₂ -brine; Marcellus	169
A.15: Crushed shale samples, post-flooding with CO ₂ -brine; Pottsville	169
A.16: Crushed shale samples, post-flooding with CO ₂ -brine; Wilcox	169
A.17: Recovered effluent precipitates, post-flooding with CO ₂ -brine; Mancos	170
A.18: Recovered effluent precipitates, post-flooding with CO ₂ -brine; Marcellus	170
A.19: Recovered effluent precipitates, post-flooding with CO ₂ -brine; Pottsville	170
A.20: Recovered effluent precipitates, post-flooding with CO ₂ -brine; Wilcox	170
A.21: Process schematics of experimental setup showing materials and equipment used for CO ₂ -brine flooding and composite core conductivity measurement	171

ABSTRACT

In large scale subsurface injection of carbon dioxide (CO₂) as obtainable in carbon sequestration programs and in environmentally friendly hydraulic fracturing processes (using supercritical CO₂), long term rock-fluid interaction can affect reservoir and seal rocks properties which are essential in monitoring the progress of these operations. The mineralogical components of sedimentary rocks are geochemically active particularly under enormous earth stresses, which generate high pressure and temperature conditions in the subsurface. While geomechanical properties such as rock stiffness, Poisson's ratio and fracture geometry largely govern fluid flow characteristics in deep fractured formations, the effect of mineralization can lead to flow impedance in the presence of favorable geochemical and thermodynamic conditions. Simulation results suggested that influx-induced mineral dissolution/precipitation reactions within clay-based sedimentary rocks can continuously close micro-fracture networks, though injection pressure and effective-stress transformation first rapidly expand the fractures. This experimental modelling research investigated the impact of in-situ geochemical precipitation at 50°C and 1,000 psi on conductivity of fractures under geomechanical stress conditions. Geochemical analysis were performed on different samples of shale rocks, effluent fluid and recovered precipitates both before and after CO₂-brine flooding of crushed shale rocks at high temperature and pressure conditions. Bulk rock geomechanical hardness was determined using micro-indentation. Differential pressure drop data across fractured composite core were also measured with respect to time over a five a day period. This was used in estimating the conductivity of the fractured core. Three experimental runs per sample type were carried out in order to check the validity of observed changes. The results showed that most significant diagenetic changes in shale rocks after flooding with CO₂-

brine reflect in the effluent fluid with calcium based minerals dissolving and precipitating under experimental conditions. Major and trace elements in the effluent fluid (using ICP-OES analysis) indicated that multiple geochemical reactions are occurring with almost all of the constituent minerals participating. The geochemical composition of precipitates recovered after the experiments showed diagenetic carbonates and opal (quartz) as the main constituents. The bulk rock showed little changes in composition except for sharper peaks on XRD analysis, suggesting that a significant portion of amorphous content of the rocks have been removed via dissolution by the slightly acid CO₂-brine fluid that was injected. However total carbon (TOC) analysis showed a slight increase in carbon content of the bulk rock. Micro-indentation results suggested a slight reduction in the hardness of the shale rocks and this reduction appear dependent on quartz content. The differential pressure drop, its 1st derivative and estimated fracture conductivity suggests that reactive transport of dissolved minerals can possibly occlude fracture flow path at varying degree depending on equivalent aperture width, thereby improving caprock integrity with respect to leakage risks under CO₂ sequestration conditions. An exponential-natural logarithm fit of the fracture conductivity can be obtained and applied in discrete fracture network modelling. The fit yielded lower and upper boundary limits for fracture conductivity closure. Higher temperature and pressure conditions of experimental investigations may be needed to determine the upper limit of shale rock seal integrity tolerance, under conditions that are similar to sequestration of CO₂ into deep and hot sedimentary rocks.

Geomechanical, geochemical and hydrological impact of engineered CO₂ storage into these geological storage options have been well researched with the conclusion that accurate estimation of maximum sustainable injection pressure plays a significant role on wellbore stability, wettability parameters, possible dormant fault reactivation among other concerns. The presence of impurities in the CO₂ stream raises the question of possible underground water and aquatic life contamination. This requires factoring the effects of trace impurities from large emission sources into CO₂ transport, injection and storage modeling [41-43].

While appreciable efforts have been expended in the scientific evaluation of CO₂ storage feasibility in conventional underground repositories, significant experimental research efforts are yet to be devoted to the seal rocks that cap most of these reservoirs. The reason might be their complexity, not just in terms of mineralogy and fluid flow behavior but also due to the lengthy laboratory measurements required for meaningful investigation. The rock-fluid interaction processes that are observed in most conventional CO₂ repositories with high permeability and porosity are to a limited extent applicable to sedimentary caprocks. Most effective caprock lithologies are fine-grained siliciclastics (clay-based rocks) and evaporites (anhydrites, gypsum, halites). An effective caprock usually has capillary entry pressure that exceeds the upward buoyancy pressure exerted by an underlying hydrocarbon or CO₂ column [33, 44, 45]. The capillary pressure of the caprock is largely a function of its pore sizes and this may be laterally variable. The buoyancy pressure is determined by the density of the reservoir fluid and column height. A caprock of extremely small pore size, in the order of nanometers, is required to prevent the buoyant rise of an underlying gas column [39, 46, 47]. The injection of CO₂ leads to CO₂-water-rock interactions that result in the precipitation and dissolution of minerals which in turn

risks result mostly from abandoned wells and faults, poorly characterized for carbon storage, and from defective well completions and surface spills during oil and gas production [68]. Future deployment of geologic sequestration technology on a significant scale could result in water-management challenges, ranging from increases in water demand for power plants to need of disposal space for pressure management to possible water-contamination issues. An analysis of the spatial adequacy of potential pressure-relief wells would enhance synergy between carbon sequestration and other subsurface operations.

In natural systems multiple minerals and other phases (such as organic carbon), gradients in pore size distributions and other components create potentially other complicating factors that reduce our ability to discern what is occurring in these systems[69]. Nanopores may contain the largest deviations from bulk-like reactivity, and at the same, may constitute the majority of pores in a rock. A sometimes overlooked set of effects of precipitation in pores are geomechanical [69]. That is, when rocks, cements or other porous materials have fluids circulate through them that induce crystallization, the precipitated material exerts a pressure on the rock itself and vice versa. As advances in experimental and imaging techniques allow for improved characterization of pore-scale processes, modeling approaches are being challenged to incorporate the textural and mineralogical heterogeneity of natural porous media, in particular with regard to their treatment of interfaces [69, 70]. The chemical transformation of iron-bearing minerals to form iron carbonates could impact the geochemistry of carbon sequestration and the presence of carbonate adsorbates does not impede the reduction of ferric iron to ferrous forming siderite. Through leaching, the chemical constituent of shale can cause a slight increase in porosity that may be available for sequestering CO₂.

The geochemical composition of shale caprock plays a significant role in its ability to perform effectively as a regional seal. The chemical reactivity of shale has been shown by several researchers to affect its petrophysical characteristics though the multiple reaction mechanisms and kinetic rates are not clearly defined and still needs to be investigated. Different mineral compositions ranging from quartz, calcite, anorthites, and feldspar to muscovite, chlorite, illite, kaolinite and smectite have been reported for shale. Mineral dissolution, re-precipitation and redistribution could affect transport properties of shale. Post experimental fluid analysis in a shale/water/CO₂ batch mixing experiment showed that the aqueous concentration of major elements such as Ca, Mg, Fe, Al and K increased and that the release rate of Fe and SiO₂ were more pronounced in solutions reacted with CO₂-brine when compared to reactions with CO₂-free brine. The use of isotopic species have been suggested in tracing diagenetic changes in shale caprock due to CO₂ sequestration. But the cost implication of monitoring the isotope partition coefficients effectively as a control tool is yet to be determined. For example in hydraulically fractured shale for the oil and gas production purposes, tracer tests faced challenges of dissolution and loss of concentration. This was for high flow paths which are different in carbon sequestration cases of lower injectivity and with no flowback expected. Monitoring wells will be difficult to maintain.

1.3 Problem Definition

Subsurface carbon dioxide leakage risk assessments to date tended to use risk scenarios, the major ones being related to wellbores, large faults and an unspecified leaking caprock. Those related to the caprock either ignore fracture networks or do not explicitly consider them in detail.

Shale caprocks are heterogeneous compaction of naturally occurring minerals and are important caprocks in oil, gas and subsurface storage (e.g CO₂ sequestration, nuclear waste disposal). Recently these rocks have become valuable hydrocarbon reserves. Given the fact that shale rocks are geochemically active minerals in the presence of aqueous fluids such as CO₂ saturated brine and high pH fracturing fluid and most shale rocks have natural fractures or are induced (hydraulic fracturing). Mineralization can affect the conductivity of fractures. Diagenetic processes involving a host of sedimentary siliciclastic minerals can play significant role in enhancing or degrading caprock integrity over the long term. Temperature and pressure play an enormous extrinsic control on these subsurface processes. The geochemical interaction of these subtle fracture networks with formation minerals has not been quantified under confining stress conditions. This is needed in long term assessment of CO₂ sequestration efficiency and possibly in loss of conductivity in hydraulically fractured tight reservoirs [71]. This phenomenon is a multi-faceted problem involving low pH fluid transport, geochemistry and geomechanics that needs be investigated experimentally along with analytical, theoretical and geologic simulation modelling.

1.4 Objective of Research

As most effective tight lithologies are either fine-grain siliciclastics (clay-based rocks e.g. shale) or evaporite (anhydrites, gypsum, halite), it is important that they provide effective hydraulic barriers in the subsurface for underground storage. Effective tight/caprocks have capillary entry pressure or displacement pressure that exceeds the upward buoyancy pressure exerted by an underlying hydrocarbon or CO₂ column; assuming no inherent deformation with lithologies that are varying in mineralogy, porosity, permeability, natural fracture distribution and wettability

parameters. Shale caprocks which are preferably of low ductility, lateral geologic continuity and thick depth of burial were used in this experimental investigations. The aim of this research project is to qualify and quantify how (micro-) fracture conductivity in shaly rocks can be impacted by diagenesis, particularly with respect to CO₂ sequestration and containment. The objective is to investigate the impact of in-situ geochemical precipitation on conductivity of open fractures under geomechanical stress conditions using laboratory and analytical modeling tools. This will provide meaningful and predictive insight on long term storage of CO₂ in shale capped reservoirs with intrinsic natural fractures and or large scale injection induced fractures.

CHAPTER 2

LITERATURE REVIEW

2.1 Diagenesis of Sedimentary Rocks

Diagenesis is the process of physical and chemical changes in sediment, after deposition that converts it to consolidated rock. Classical diagenesis is considered to be a slow process occurring over centuries, but in fact, the reactions occur fairly rapidly, requiring fractions of years at reservoir conditions [56, 57, 60]. The centuries of time normally associated with diagenesis is the time required to bury sediment deep enough to reach the pressure and temperature conditions conducive to diagenetic change. Common minerals, dissolved in or precipitated from an aqueous phase can be grouped into those that are relatively reactive or inert in that their dissolution or precipitation rates are fast or slow, respectively, relative to the flow rate of the aqueous phase [72]. Multiple investigators have outlined the consequences of variations in reaction rates relative to flow rate of the fluid in which the minerals are reacting [56, 57, 59, 60, 72]. These minerals can be further grouped according to simple and complex stoichiometry. Those minerals with complex stoichiometry are much less likely to reach the solubility equilibrium than those with simple stoichiometry. For example, it is well known that simple ionic solids with high solubilities (such as halite, mirabilite, and carnallite) will reach solubility equilibrium more quickly than complex solids with a much more covalent character and low solubility [57]. Since calcite is a reactive mineral and has simple stoichiometry, it is considered as an example of water-rock reaction problem whenever it is present in substantial amounts. Calcium carbonate minerals can become insoluble at high pH and exposure to acidic fluid can reverse it. Generally, diagenesis of carbonate rocks includes all the processes on the sediments after their initial deposition [73].

In general, most researchers suggested that reaction trends are very difficult to identify at any temperature. This is not to say that no reaction occurred but the complex natural mineralogical composition envelops all reactions [65, 70]. In other experiments on the same formation and using an image analysis technique, an illitization of the illite-smectite components was identified, as well as the formation of gypsum. But similarly, these reaction paths are very difficult to identify using standard bulk measurements such as X-ray diffraction (XRD). With such difficulties in identifying reaction paths, the reaction kinetics is obviously out of reach [33, 61, 93].

Previous experimental research works have documented evidences of pore structure alteration in CO₂ flooded shale caprocks. The previous section (section 2.2) describes in detail some properties of the injected fluid in these experiments.

2.3.1 Geochemical Dissolution/Precipitation.

The instability of clays in the presence of low-pH fluids has also been observed when using hydraulic fracturing fluid. Low-pH fluids are capable of dissolving clays and silicates. As temperature increases, the solubility of silici-clastic minerals is significantly increased especially in low-pH environment [94, 95]. These findings are often observed when immersion tests are run on cores in the laboratory. This type of fluid-mineral reactions is dynamic processes that involve many effects: complex fluid flow, pore space changes, surface chemistry, and the mineral composition. Several clays have been observed swelling rapidly in the presence of depressed pH and elevated temperature including sloughing or disappearance of swelling clays [32, 94]. After minerals are dissolved in the low-pH fluids, they can precipitate in the formation pores, restricting fluid flow and leading to scaling and progressive geochemical aggregation [57, 69]. Clay solubility

It has also been showed that mineral dissolution can be understood through the same mechanistic theory of nucleation developed for mineral growth [108]. The derived dislocation model can predict variation of the normal aluminosilicate dissolution rate (R_n) with degree of under-saturation (σ). It is argued that two-dimensional nucleation dominates rates measured at higher temperatures 150°C – 200°C. In contrast, the 80°C data for kaolinite is predicted by the dislocation defect model. Nonetheless, this model has not been further developed for clay minerals other than kaolinite.

Implementation of base case dissolution model has gained terrain as real-time microscopic observations of reacted mineral surfaces offer new insights into the dissolution mechanisms [108]. Also, the validity of the TST-based rate laws to be sufficient to explain mineral dissolution kinetics as a function of distance from equilibrium has been questioned, mainly based on the fact that TST allows a relation between the forward and reverse rate constants but only of an elementary reaction [112, 113]. The adequacy of simple surface adsorption models to explain the complexity of the three-dimensional lattice and its participation in the dissolution process is also argued. Previous works showed that the use of a stochastic approach that treats crystal dissolution as a many-body problem has led to the development of the step-wave model and some in-depth exploration of the dissolution mechanism [114].

As it has been extensively discussed in the literature, most of the descriptions and interpretations of the clay dissolution kinetics are at the moment, TST-based. Therefore, TST is further discussed. The terms integrated in equation 2.8 above other than the $f(\Delta G_r)$, account for the effect of different environmental variables on clay dissolution rates.

and precipitation of clay minerals (and phyllosilicates) occur preferentially at the edge. Lack of correlation between the total and the edge surface area of smectite makes the smectite BET surface area an ineffective proxy for its reactive surface area. This conclusion may be extrapolated to all clay minerals which form layered particles. Hence, it is suggested to use AFM measurements of the specific edge surface area as an alternative proxy for the reactive surface area of smectite and other clay minerals [116, 120-122]. However, the recent VSI and AFM experiments with muscovite indicate that basal/edge surface area ratios are highly variable and change continuously over the progression of the reaction, thus obviating their utility as characteristic parameters defining mica reactivity [108].

2.3.2.4 Catalysis/Inhibitors

Aluminum (Al) and organic matter (OM) can be used as proxy for measuring catalytic and inhibiting phenomenon in clay rich shaly rocks [108, 123]. It has been showed strong Al inhibition of kaolinite dissolution reaction under very-far-from-equilibrium conditions at 150°C and pH = 2. The reaction order of this inhibition was -1. It was proposed that Al-silicate dissolution is controlled by a Si-rich precursor complex formed by the exchange of Al for protons at the surface [116, 124]. Due to differences in the surface properties of different minerals, there is a significant variability in their tendencies to adsorb organic matters. Among the naturally abundant minerals, the most effective adsorbents are clay minerals and oxides [25, 110, 125]. Although both inhibition and enhancement of clay mineral dissolution rates were observed, the latter effect is much more common. Low molar mass organic acids (e.g., oxalate, malonate, citrate, salicylate, o-phthalate, and gluconate) through ligand-promoted dissolution at mineral surfaces and

the stress generated by the volume increasing process is large enough to create a fracture network that will enable continued fluid flow. Reaction-induced fracturing is particularly relevant during fluid migration into high-grade metamorphic and slowly cooled magmatic rocks with very low initial porosity, but may also be important during reactive transport in more porous rocks where growth processes within the pore space exerts forces on the pore walls [20, 144] and fracture propagation. Spheroidal weathering is an example of a process where reactions produce pronounced fracturing under the low confining pressures that prevail near the Earth's surface. This kind of weathering has been described for most rock types in a wide range of climate zones. Although spheroidal weathering, per definition, involves surface-parallel fracturing and spalling of layers at the margin of rock blocks, which become progressively rounded (core stones), the progress of this mode of weathering and the fracture patterns produced are sensitive to the initial porosity of the rock type [145]. Fluid flow in fractures is assumed to be effectively instantaneous compared to the rate of other relevant processes [146, 147]. In a natural system, the progress of the fluid-driven, volume-increasing reactions, is controlled by two main parameters: rock porosity, and the shape of the initial domain undergoing volatilization [148, 149]. For circular domains, porosity variation will control both the relative rates of reaction kinetics and transport, often expressed by the dimensionless *Damkohler* or *Peclet-Damkohler* Number, and the amount of the mobile reactant that the rock can contain [70, 150]. Although reactions may produce fractures and porosity, mineral growth in pores may also lead to clogging. This may significantly decrease the permeability and therefore fluid migration through initially porous rocks, and through rocks that are initially fractured due to tectonic and thermal processes. When fluid consuming reactions occur synchronously with tectonic deformation, the externally imposed

stress may completely control the reaction rate and progress if permeability is generated at a faster rate than the infilling of pores by reaction products. On the other hand, if the precipitation rate is fast compared to the rate of fracturing and permeability generation, the progress of reaction may be modest even in extensively fractured rocks [151].

Replacement reactions mediated by a fluid phase take place through a coupled dissolution–precipitation reaction. When fluid comes into contact with the reactive mineral, dissolution takes place at the mineral surface [138]. This immediately creates a supersaturated solution with respect to the replacing mineral, which will then precipitate in the immediate vicinity of the dissolving surface. A nanometer-scale confined fluid film between the parent and daughter phases will allow the reaction to continue. If the supersaturation with respect to the precipitating phase is high, there will be enough chemical energy available for the precipitating material to exert a mechanical stress on the reacting grain, and cause fracturing, when precipitation is confined within dissolution pits and wedges [151].

A well-established example of the use of the continuum approach for interfacial reactive processes is that of reactive transport in fractures. In fractured media, there is a sharp contrast—with a clear separation of scales—between the porosity in the fracture and in the rock matrix [135]. As a result, the fracture is modeled as a fast flow path, where transport is dominated by advection, and the rock matrix, where transport is dominated by diffusion. Heterogeneous reactions take place within the porous rock matrix or the layer of precipitate that coats the surface [152]. To simulate flow in discrete fractures in Darcy-scale models, the cubic law is often used to obtain a fracture permeability under the assumption of parallel smooth walls [153]. However, this model does not typically provide an accurate estimation of fracture hydrodynamic

properties at realistic fracture roughness. Mineral rates measured in laboratory experiments are often several orders of magnitude faster than those estimated from natural systems [154]. These differences in rates have been attributed to a variety of factors including, among others, reactive surface area accessibility in natural porous media, limitations on flow and transport in heterogeneous material, or transport, rather than interface control of rates. Microfracture-scale modeling can be used to address some of these hypotheses by explicitly accounting for the rate-limiting effect of transport, and by incorporating mechanistic descriptions for the evolution of reactive surface area [155, 156].

Applications of direct numerical simulation of pore-scale processes in subsurface materials are growing in part due to the computational advantages of well-established computational fluid dynamics (CFD) methods [70, 151]. Availability of high-level, open-source libraries such as *OpenFOAM* or *Chombo* have also facilitated implementation of models into new simulation capabilities [157]. In reactive systems, the ability to calculate the heterogeneous reaction rates at the fluid–solid interfaces makes direct numerical simulation a suitable tool to mechanistically model processes that are not captured by models at larger scales, especially when well-mixed assumptions are made [158, 159]. In multiscale problems, direct numerical simulation has typically been performed using continuum methods rather than strictly using pore-scale methods. In these methods surface reactions and transport processes are not explicitly calculated at the interface and are upscaled from the pore scale [160]. Upscaling of strongly coupled non-linear processes is not straightforward and the solution of macro- and micro-scale problems is coupled. It is ultimately the combination of new microscopic characterization, experimental, and modeling approaches that presents the opportunity to provide mechanistic

One of the most important mechanisms of diagenetic processes is chemical reaction between minerals and migrating fluids. The hydraulic isolation of a porous medium by a caprock layer provides an environment amenable to several uses of the underlying porous formation. When the porous medium is under artesian pressure, it serves as a ready source of water supply. With sessile groundwater conditions, such porous formations are looked upon favorably for deep geologic disposal of contaminants and other forms of hazardous waste in liquid form. Hydrodynamic and stratigraphic trapping represents the primary phase of containment of the fluidized CO₂ and it is assumed that this will ensure longevity of the retention of CO₂ in the storage formation. This environment would enable the initiation of other time-dependent trapping mechanisms, including solution, mineral and residual phase trapping that can occur at time scales varying from the time of injection to a million years.

It can be assumed that the caprock fracture is stationary and that its dimensions are uninfluenced by the pressures of injected fluids. This is hardly the case in many oil and gas operations that are related. Fractures are nearly ubiquitous in rocks that have experienced even slight deformation and most of these are mineral filled [175]. Their presence indicates that: (1) dilation of the rock took place for fractures to be both open and provide pathways for fluid flow and (2) fluid was present and perhaps moving during and after the deformation event, and it carried sufficient mass of fracture constituents in solution to precipitate in the observed fracture void space [176, 177]. Pressure solution and compaction mechanism as a result of enormous formation stress is a driver for the diagenetic loss of fracture conductivity and adjoining formation permeability [59, 178, 179]. Pressure solution and compaction of quartz materials have been extensively studied and models have been developed that relate the rate of

A crystal growing in a pore will stop growing when the stress on the crystal surface approaches the maximum crystallization pressure [137]. However, if the stress is sufficient to open a fracture, the stress on the crystal surface will decrease, thus enabling further growth. When strain rates are slow, as can be the case during precipitation in pores and cracks, fracture propagation takes place through a kinetic process known as subcritical crack growth [167, 180]. Previous works have demonstrated how to couple the rates of crystal growth and fracture propagation when a crystal grows from a supersaturated solution inside the aperture of a fracture [181]. As long as there is an unlimited supply of supersaturated solution, fracture propagation causes the stress on the crystal surface to decrease and the rate of fracture propagation will accelerate until complete failure takes place [182]. Few researchers have developed precipitation/dissolution models for the flow in finite parallel plates that represent single fractures [183]. The idea behind such models is to approximate the description of a variable fracture aperture, surface reaction, and diffusion by a set of parameters and simple rules governing the alteration of fractures [184, 185]. Fracture aperture can either grow or shrink as chemical reaction proceeds at the fracture surface. This sometimes involves mass conservation equations for the components of aqueous and solid phases simultaneously and shows the fracture aperture size distribution with time. Calcite cementation is a form of precipitation that can be modelled and incorporated. It has been shown that to replicate the lower permeability that typify tight gas shale requires the superimposition of systematic cement filling that preferentially plugs fracture tips and other narrower parts of the fracture pattern [15, 146, 186]. Additional challenge for natural fracture characterization is quantifying the effective permeability of fracture networks. A benefit of the mechanics-based analysis is that fracture aperture is an intrinsic part of the solution; a result of boundary

days of high P_{CO_2} (8.3 MPa) injection, followed by 50 days of no-flow. During fluid injection, the aqueous concentrations of Ca, Si and Sr decreased, while Mg increased. After the 50 days without flow, a second injection period was started with an injection rate 10 times the original one. This rate was later lowered to 2 times the original rate, thereby completing an increase-decrease sequence simulating uplift followed by burial. All the steady state concentrations decreased after the injection rate was increased, whereas decreasing the injection rate again led to increasing concentrations in a step-like manner. The overall higher concentrations of Mg and Ca compared to Si were attributed to a well-known decrease in reactivity from dolomite and calcite to quartz [65].

Furthermore, injected CO_2 at 200°C and 20 MPa into an aquifer-aquitard system composed of Arkosic sandstone and shale, respectively. The injection period lasted for 80 days, and the purpose was to examine fluid-rock interactions with focus on carbonate mineral precipitation [43, 149]. This was done by investigating reaction textures on aquifer and aquitard minerals, carbonate minerals precipitated and changes in brine chemistry. In addition to precipitated magnesite, amalcine mica and clay minerals, their results showed textures on silicate minerals which indicated significant reactions. The arkosic sandstone serving as the aquifer was composed of equal amounts of quartz, oligoclase and microcline. On the edges of pits and open fractures of the quartz grains, abundant clay minerals were observed using SEM. Smectites not present on the initial oligoclase were present in abundance on the surfaces and cleavages of the CO_2 exposed oligoclase grains. While it was observed that there were differential etching on the microcline surfaces, the same phenomenon was not observed for the oligoclase. For the shale (mostly composed of quartz and clay minerals), they saw clay coatings draping across surfaces and small

S-wave velocities can be used to separate the effect of pore pressure increase from the combined effect of pore pressure build up and increasing CO₂ saturation. This can possibly be used to separate between reservoir zones with CO₂ and high pressure zones without CO₂ [75].

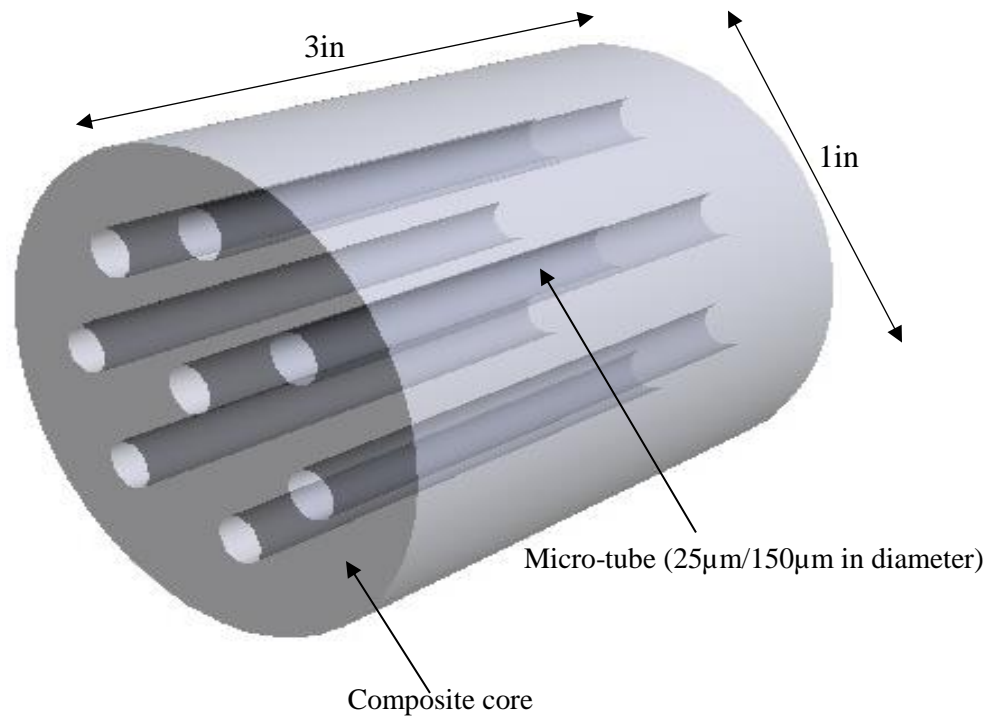


Figure 3.2: Visual design of composite core made of kaolinite, cement and micro-tubes (magnified) using SolidWorks®.



Figure 3.3: Visual sample design of composite core made of kaolinite, cement and polymer PEEK micro-tubes which are not evenly distributed as envisage through SolidWorks®.



Figure 3.4: Multiple samples of composite core made of kaolinite, cement and polymer PEEK micro-tubes to mimic fractures.

for a time frame of 5 days per run. The shale rock was comminuted (crushed) to predetermined dimensions that are suitable for use in analytical instrument. See figures in appendix A. Particle sizes in the packed-beds were of the order of 1mm - 2mm in dimension. A single flow cell was used with designs similar to a packed-bed. This exposed as much surface area of the crushed shale as possible to CO₂-brine. Each experimental run holds an average of 350g of shale caprock samples with different mineralogy which are dependent on basins and formations type. Multiple representative samples were analyzed and compared to corresponding control samples. All instrument and process devices are of stainless steel and PEEK (Polyether Ether Ketone) material. This ensured that metallic corrosion processes do not interfere with critical measurements during the experiment. PEEK and stainless steel materials are generally resistant to CO₂-brine induced corrosion. Ceramic/stainless steel micro-filters (50µm limit) and circularly-cut filter papers (5µm limit) were used to prevent fines migration within tubings and packed-bed respectively.

3.2 Experimental Setup

The experimental set-up consisted of a core flooding unit (CFS-200), an automated Oven, a heating tape, a stainless steel pressure cell, a syringe pump (and a piston pump for backup), a back pressure regulator (BPR), accumulators (glass beaker), multiple transducers, three pressure gauges, PEEK and stainless steel tubings, National Instruments data acquisition device, two ceramic filter to prevent fines carry over (larger than 50 μm) and a computer system. PEEK polymers were used because it has high resistance to corrosion as a result of low pH or high temperature and pressure conditions. Schematics of the CO₂-brine flooding of shale caprock and composite fractured core injection are shown in Figures 3.1 and 3.2. The packed-bed was mounted vertically in the oven for temperature control with aqueous CO₂ flowing from the top to the bottom of the experimental fixture. This is to prevent particulate fluidization were it to be the other way round i.e. bottom to top. Also the effect of gravity is assumed to be negligible. A schematic of the experimental setup is shown in figure 3.3. Figure A.1 in Appendix A has pictures of the physical components of the experimental setup among other equipment and consumable.

3.3 Experimental Shale Rocks Geology

The approach used in the design of experiments required multiple shale rock samples to be used such that geographical and mineralogical variations are factored into the experimental matrix configuration. Table 3.1 below shows the geological properties of the shale samples that were used in the flooding experiment. This consist of Mancos, Marcellus, Pottsville and Wilcox shales. These shales are found in different geographic regions of the United States with potentials for energy fluid extraction or storage of carbon dioxide.

The X-ray source sends the signal and receives a response. Each mineral has a characteristic response. Computer software determines the type of mineral and outputs peak versus intensity plots for the minerals present in the core sample. Since XRD can only determine crystalline substances, amorphous materials present cannot be identified by XRD. XRD analyses were conducted on the control sample and the CO₂-brine contacted samples at the LSU's Shared Instrumentation Facility (SIF) using a Siemens Kristalloflex D5000 X-Ray Diffractometer. This technique was used in the mineralogical analysis of the shale caprock- inorganic mineral composition.

- 2) **SEM-FIB Imaging with EMPA:** Scanning Electron Microscopy with Focused Ion Beam (SEM-FIB) is a technique that was used to examine physical changes on the surface of the shale particles providing useful information at high magnification and resolution. Portions of CO₂-brine contacted and uncontacted crushed shale caprock samples were imaged using SEM for microstructural characterization. SEM was deployed to further investigate the nature of altered surfaces at a much finer scale and under low vacuum conditions in order to obtain clearer images during the analysis. Micro-porous spaces can be identified from the captured images. The SEM images were obtained using an EDAX model electron microscope at the Center for Material Characterization, in the LSU Mechanical Engineering Department. Light microscopy images were obtained using a Leica microscope at the LSU Sustainable Energy and Environmental Laboratory. These techniques were used to examine physical changes on the surface of the shale particles providing useful information on structural morphology at high magnification and resolution. Thin sections slides are the appropriate samples to use.

- 3) **Micro-indentation:** This was a complimentary analysis that can provide useful information on chemo-geomechanical changes in the flooded shaly rocks. The material hardness characterization technique was used to analyze polished customized samples. The micro-hardness test uses an established method where a diamond indenter tip with a known geometry is driven into a specific site of the sample by applying an increasing normal load. Nanovea® MicroHardness Tester, which was used, is based on the standards for instrumented indentation, ASTM E2546 and ISO 14577. The indenter tip with a known geometry (Vickers' Diamond) is driven into the shale sample to be tested, by applying an increasing normal load. When reaching a pre-set maximum value, the normal load is reduced until partial or complete unloading of the sample occurs. For each loading/unloading cycle, the applied load value is plotted with respect to the corresponding position of the indenter. Six-spot indentation was done in a form of a 3-line profile, on every sample ranging from outer pipe position to the inner region of the shale specimen, covering its entire cross-section (more than 20 indentation points in total). The following set of conditions was used in all the indentation experiments: the maximum force used was 20 N; the loading and unloading rates were kept the same at 20 N/min; the pause at maximum load as 30 seconds; the contact load was 30 mN. The hardness was obtained with computation method from Oliver and Pharr [219]. The indenter type was Vickers diamond with the Poisson coefficient of 0.07.
- 4) **ICP-OES Analysis of influent/effluent:** Analysis of influent/effluent fluid included metallic mineral evaluation of the influent and the effluent which established the expected geochemical alterations in the rock with CO₂-brine depletion. Inductively Coupled Plasma-

Optical Emission Spectroscopy (ICP-OES) is a method which was conducted to determine metallic cation contents in the fluid. The fundamental characteristic of this process is that each element emits energy at specific wavelengths peculiar to its atomic character. By determining which wavelengths are emitted by a sample and their intensities, the analyst can determine the elements from the given sample relative to a reference standard qualitatively and quantitatively. The samples were analyzed in the LSU's School of Plant, Environmental and Soil Sciences. During the experiments, effluent brine samples were monitored for pH and collected daily while samples were selected for ICP-OES analysis depending on pH values. Metallic mineral analysis of the influent and the effluent were used to correlate the expected geochemical alterations in the rock with CO₂-brine pH change and fracture conductivity loss.

3.7 Experimental Parameters

The following geochemical, geomechanical, and flow parameters were experimentally determined using crushed shaly rocks samples and composite rock respectively. The reactive fluid of interest is the CO₂ saturated brine.

3.7.1 Geochemical Properties

1. Cationic assay of effluent (ICP-OES)
2. pH of effluent
3. Mineralogy of flooded crushed shale rocks (XRD, EDS, EMPA, XPS)
4. Morphology of crushed shale rocks (FIB-SEM)
5. Total organic carbon content of crushed shale rock

Table 3.7: Pre-injection and Post-injection analyses for each CO₂-brine flooding experimental run including rock and fluid sampling procedure.

Run No.	Type of Analysis
Step 1	Flood crushed shale rock with CO ₂ -brine and transport effluent to composite core under varying axial and radial stress.
Step 2	Take real time measurement of differential pressure drop for changes in conductivity. This will be automatically acquired during injection and transport of CO ₂ -brine.
Step 3	Analyze final effluent composition (pH, ICP-OES). Analyze crushed shale rock for morphology, mineral composition, total organic carbon composition and hardness characteristics (SEM, EDS, XRD, TOC, Micro-indentation).
Step 4	Calculate effective fracture aperture and fracture conductivity.
Step 5	Use geochemical results to bound overall chemo-flow modelling in aqueous CO ₂ -shale interaction under constant geomechanical conditions

3.8.3 Critical Experimental Conditions and Materials

- Artificial Cores Solids Fraction: made from cement ($\approx 97\%$), kaolinite ($\approx 3\%$) and PEEK polymer micro-tubing (resistant to chemical corrosion)
- Crushed Shale Rocks: sizes <2mm (lots of fines)
- CO₂-Brine Composition: 22.6g/l (22600 ppm) of NaCl solution
- Pressure Vessels and Flowlines: high temperature and pressure rated (max. of 350°F, 4000psi)

3.8.4 Experimental Process Parameters for Conditions A and B as Reported in Chapter 4

The following experimental conditions were used during the shale/CO₂-brine flooding

- a. Global flow rate: 0.5ml/min
- b. Flow cell(s) back pressure: 1000psi
- c. Flow cell(s) axial and radial pressure:1400psi
- d. Operating temperature: 50°C
- e. pH of CO₂ – brine: 3.7 – 3.8

The raw data of most of the experimental results presented in Chapter 4 are included in the Appendix section of this report.

CHAPTER 4

RESULTS FROM SHALE ROCK/FLUID INTERACTIONS EXPERIMENTS

4.1 pH Measurement

Measurements of the pH of the effluent for all the 24 experiments were taken and the averages reported in figure 4.1. The pH values for each sample type were used for the computation of the standard error (standard deviation). It can be observed from the pH profile that the alkaline buffer strength of the shale rocks through reactive interaction with the CO₂-brine fluid at the experimental pressure and temperature conditions is significantly pronounced for the Mancos, Marcellus and Pottsville shale rocks while that of the Wilcox shale is markedly lower.

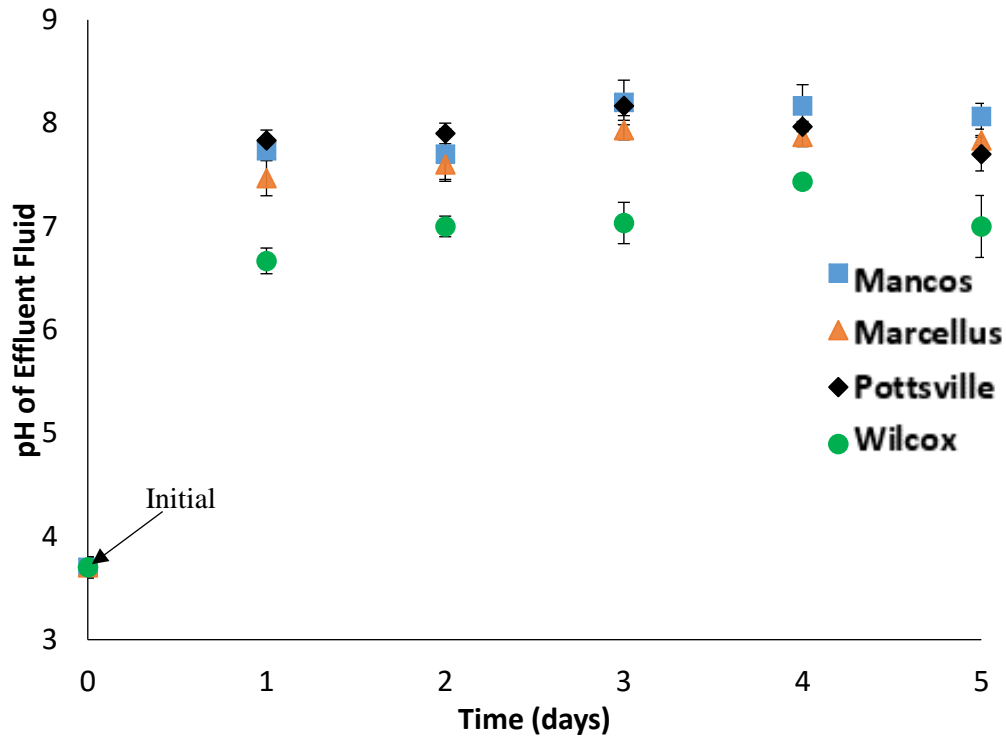


Figure 4.1: pH measurement of effluent for the four different shale rock samples used for the rock-fluid interaction experiment. It shows consistent increase in the pH values indicating significant alkalinity buffer strength of the shale rocks in the presence of acid CO₂ -brine fluid that was injected. This buffer strength is expected to reduce over time under dynamic condition.

The profile showed a trend pointing towards a waning of the buffer strength by the 5th day. The error bars are standard deviation values based on 3 measurements of pH values. These observations are in agreement with previous experiments conducted in the laboratory and reported by other researchers. This changes in pH is expected to control, to some degree, the ability of the various rock minerals to exchange ions with one another.

4.2 Inductively Coupled Plasma-Optical Emission Spectroscopy (ICP-OES) Analysis

The inductively coupled plasma optical emission spectroscopy analysis of the effluent from moderate temperature- moderate pressure runs using the four shale rock samples are shown in figures 4.2 to 4.15. The dimensionless concentration of both the major and trace elements in the effluent solution at the end of the experiments were analyzed using the initial composition of the influent CO₂ saturated brine as the normalizing quantity. The elemental concentration of the influent is 1 on each of the graph. Sections 4.2.1 and 4.2.2 discusses the major and trace elements present in the fluid in details and relating them to the mineralogical composition of the bulk rock samples. Geochemical reactions of interest are also further discussed in Chapter 5.

4.2.1 Major Elemental Concentration in Effluent

Elemental Calcium concentration in the effluent collected at the outlet of the artificially fractured cores are presented in figure 4.2. The ratios of Ca_n/Ca_o are presented as data points on the chart. Ca_n represent the concentration of Calcium in part per million (ppm) for each day (n = time in days). Ca_o is the original elemental concentration in the influent CO₂ saturated brine. This dimensionless entity represents the fractional increase or decrease in the elemental composition

of Calcium and other major alkaline earth metals discussed in this section (Magnesium (Mg), Potassium (K), Selenium (Se), Sulphur (S) and Silicon (S)). The error bars are standard deviation values based on 3 measurements of elemental composition.

The concentration profile for Calcium shows that the Marcellus samples had the highest fraction in solution which rapidly decreased over the five day period of continuously flooding the samples with CO₂ saturated brine. The initial pH of the influent fluid is approximately 3.7. The Mancos, Marcellus and Wilcox shale rocks exhibited similarly trend of a gradual exponential decline over the five day period. The Pottsville shales reflected a gradual increase that appears to continue over the experimental period.

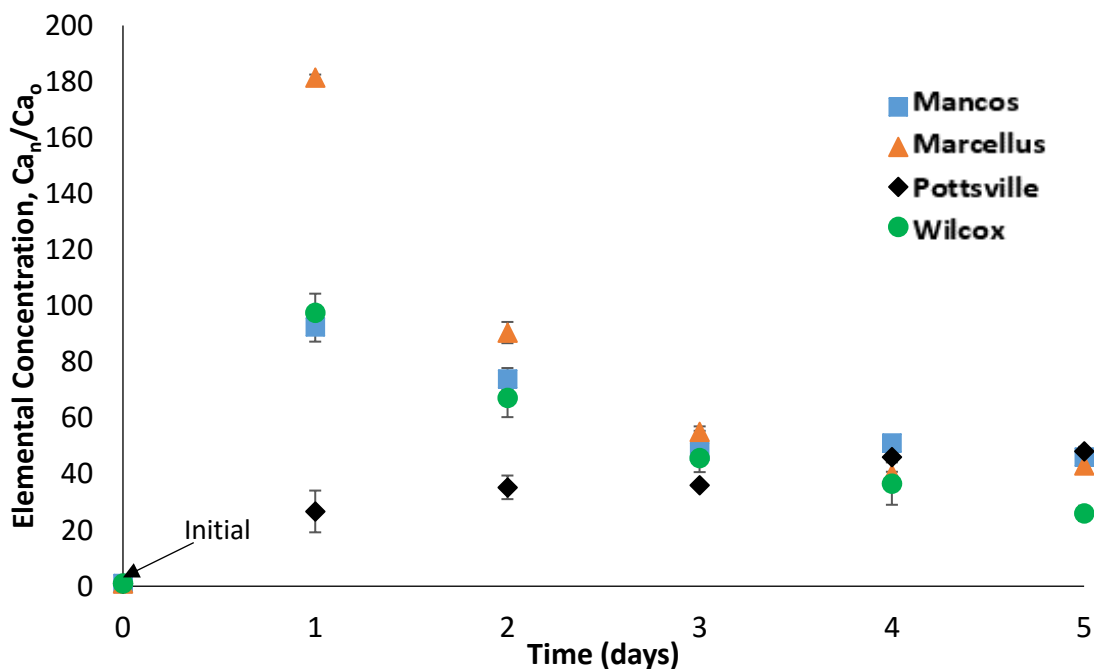


Figure 4.2: Dimensionless elemental concentration of the effluent fluids showing the fraction of Calcium (Ca) that were leached out from the shale rock samples. The Mancos, Marcellus and Wilcox shale rocks had significantly higher fraction of Ca within the first two days of the experiment compared to the Pottsville, indicating greater dissolution of calcium based minerals.

While the elemental concentration of Calcium in the Mancos, Marcellus and Wilcox shales peaks on the first day of the experiment, that of the Pottsville shale continued to increase over the five day period but it also expected to peak and gradually decline with similar trend to the Mancos, Marcellus and Wilcox shales. This resilient behavior of the Pottsville shale might suggest a slower dissolution reaction of its calcium based minerals constituent compared to the Mancos, Marcellus and Wilcox shales. The bulk rock XRD analysis indicated calcite and dolomite as the main calcium bearing minerals in the Mancos, Marcellus and Wilcox shales while anhydrites are the main calcium bearing minerals in the Pottsville.

Figure 4.3 presents the five day elemental concentration trend in the effluent for Magnesium. The profile for the four samples are similar to that of calcium. It can be observed that the fractional composition of magnesium in the effluent are about half of elemental calcium presented in figure 4.2. The Mancos, Pottsville and Wilcox shale rocks appear to be plateauing out after the five-day experimental period, while the Marcellus shale samples is rapidly approaching zero concentration during the same period. The similarity of concentration profile suggests that plausible geochemical dissolution reactions are occurring along with magnesium based minerals in the shale rocks. This type of reactions are mostly associated with calcite, dolomite and illitic (illite containing) clay minerals.

Elemental Potassium in solution (figure 4.4) exhibited a trend that showed a reduction in the free potassium available in the influent fluid for the Marcellus and Wilcox shale rocks before stabilizing after the five-day experimental period. This indicated a consumption of the potassium element in the injected fluid via reactive rock-fluid interaction for the two samples. The Mancos and Pottsville shale samples exhibited the general trend of initial increases in elemental

(potassium) concentration, in the effluent fluid, followed by a decreasing profile as the experiment progresses. This is most-likely due to limited rock volume.

Concentrations of Selenium (figure 4.5) are most significant for the Mancos and Pottsville shale rocks while the Marcellus and Wilcox shales had little to no selenium ions leached into the effluent fluid. The presence of selenium in the effluent solution showed the extent of shale rock samples' heterogeneity as no known selenium bearing mineral was identified in the rocks by XRD analysis. This suggests that these selenium bearing minerals only exist in trace amounts within these sedimentary rocks matrix. The presence of free selenium in solution could act as catalysts for faster reactive flow. Furthermore, Sulphur content (figure 4.6) was highest in the Wilcox shale followed by the Mancos and Marcellus shale. This confirms that CO₂ saturated-brine can effectively dissolve stable minerals like pyrites and other sulphur bearing minerals. The Marcellus and Wilcox shale samples had the highest content of pyrite mineral as identified by XRD analysis. It appears that there is a preferential dissolution of pyrite in the Wilcox shale compared to the Marcellus, even though it has a higher content of pyrite. It can be assumed that relative abundance of these soluble minerals in the rock matrix would have influence on geochemical speciation in the effluent. The convective transport of these geochemical species are important in balancing the equilibrium conditions of the subsurface. The introduction of fluids such as dissolved CO₂ in brine can significantly alter the equilibrium landscape that can affect the natural in-take or release of chemical species. The trend noticeable in these results suggest that massive dissolution of calcites and dolomites might pose significant challenges in cases where there are significant ingress of carbon dioxide in aqueous form into the shale caprock. This can lead to increased percentage of flow paths within the rock.

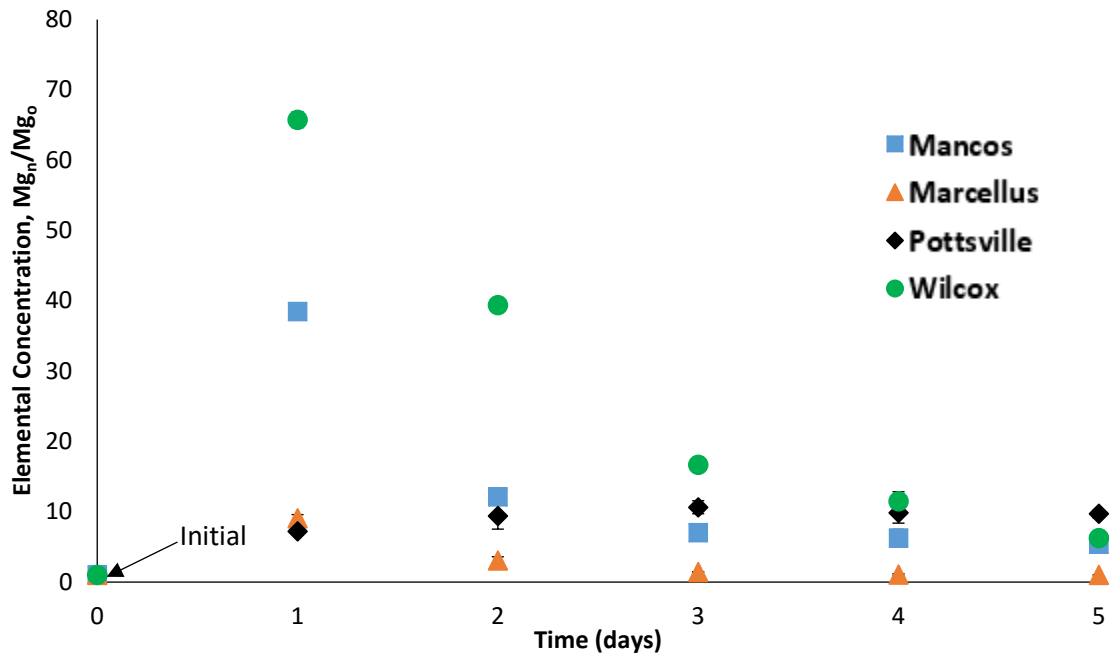


Figure 4.3: Dimensionless cationic concentration of the effluent fluids showing the fraction of Magnesium (Mg) that were leached out from the shale rock samples. The trend of the Mg concentration is similar to that of Ca indicating concurrent geochemical reactions.

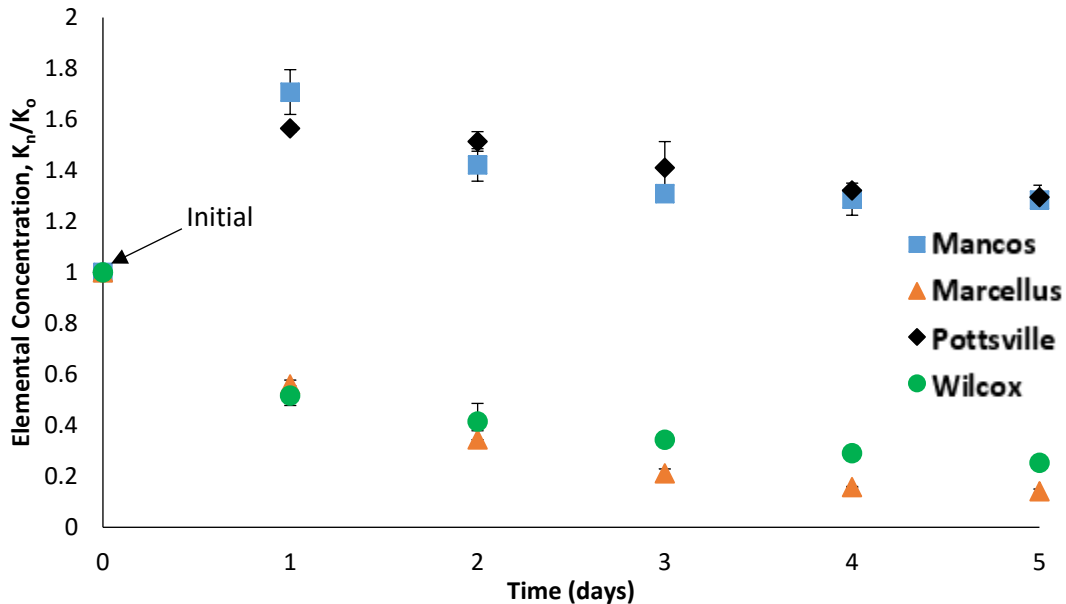


Figure 4.4: Dimensionless cationic concentration of the effluent fluids showing the fraction of Potassium (K) that were leached out from the shale rock samples. The profile for the Marcellus and Wilcox shale rocks indicated a marked reduction in potassium concentration beginning from the start of the experiment. This suggests that trace amount of K in the brine were absorbed.

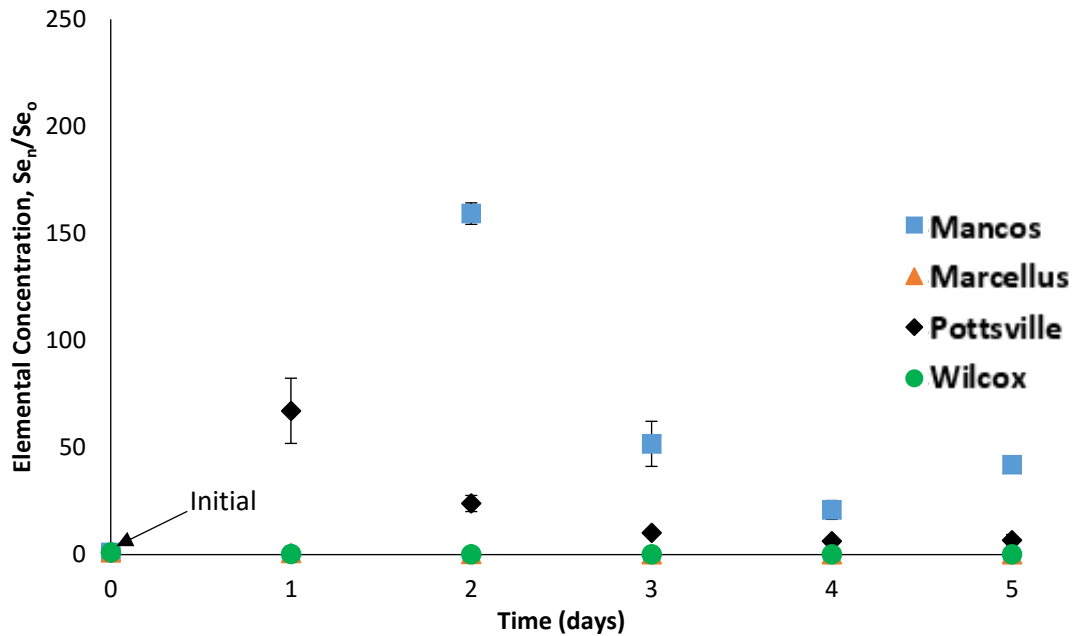


Figure 4.5: Dimensionless cationic concentration of the effluent fluids showing the fraction of Selenium (Se) that were leached out from the shale rock samples. The profile showed that selenium is present in significant quantity within the shale rock of Mancos and Pottsville with only trace amounts in the Marcellus and Wilcox shale rocks.

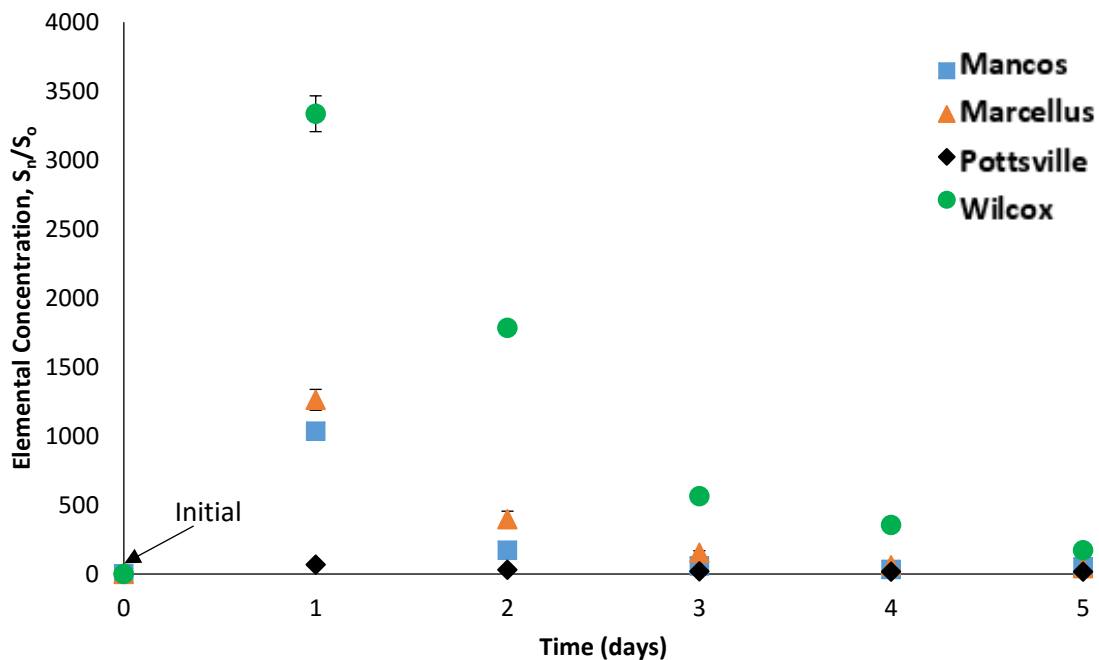


Figure 4.6: Dimensionless cationic concentration of the effluent fluids showing the fraction of Sulphur (S) that were leached out from the shale rock samples. The concentration of Sulphur was highest in the Wilcox shale with fractional values peaking with the first day of the experiment. Pottsville shale appears lean in Sulphur content all through experiment.

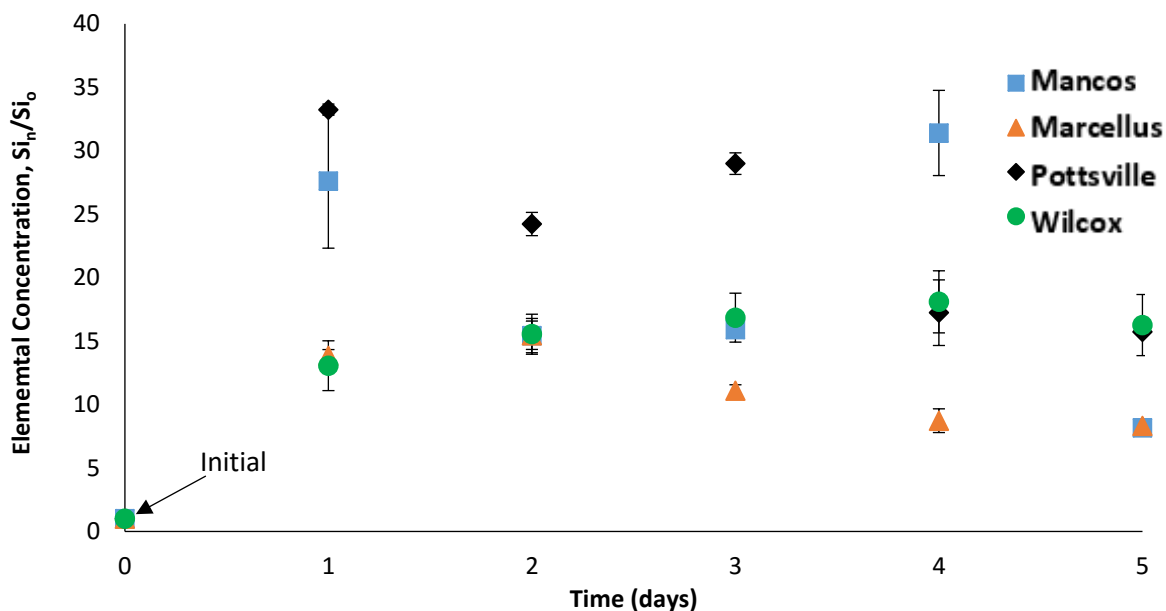


Figure 4.7: Dimensionless cationic concentration of the effluent fluids showing the fraction of Silicon (Si) that were leached out from the shale rock samples. The fractional profile of silicon indicated dissolution of silicon bearing minerals. It is possible that of early precipitation in form of diagenetic quartz occurred as the concentration of Si remained fairly constant.

Elemental silicon concentration in the effluent analyzed showed that they are present in solution in significant quantity compared to the initial CO₂-brine fluid that was injected. Figure 4.7 documents these Si concentrations for all the shale samples. The presence of diagenetic quartz in the precipitates recovered, indicated that most of the silicon in solution had crystalized out of the solution to form a variant of opal mineral that is amorphous in shape.

4.2.2 Minor Elemental Concentration in Effluent

Trace concentration of certain elements in the effluent solution is discussed. These include Aluminum (Al), Arsenic (As), Boron (B), Iron (Fe), Manganese (Mn), Nickel (Ni), Phosphorus (P) and Zinc (Zn). They are described as occurring in trace amounts because the actual part per million (ppm) concentrations are in the range 0.1 mg/l to 10mg/l which are significantly lower

compared to the concentration of the major elemental compositions described above. Previous researchers have attempted to model trace metals mechanism of release and evolution in carbonates reservoirs that are capped by shale rocks [43].

Figure 4.8 shows the concentration of Al in the effluent solution for all the four samples used in the five day experiment at moderate temperature and pressure conditions. The concentration for the Marcellus and Wilcox followed the trend observed in potassium concentration profile indicating a consumption of the element during possible reactive rock-fluid interaction. It is safe to assume that Aluminum did not participate significantly in these reactions given its low concentration in the effluent, though dissolved aluminum bearing minerals in solution could have precipitated out of the solution in form of clay, therefore the low concentration. The Mancos and Pottsville shale rocks showed little to no change in Al concentration indicating passive interaction of aluminum bearing minerals in these samples with CO₂-brine influent fluid. Arsenic and Boron elemental compositions (Figures 4.9 and 4.10) showed a similar trend to that of Aluminum for all the samples analyzed.

Elemental concentration of Iron is quite significant in the Wilcox as shown in figure 4.11. The chart presents a confirmation that the pyrite (FeS₂) content in the Wilcox reactively interacted more with the influent fluid leading to high concentrations of Iron (Fe) and Sulphur (S) in the effluent. Other samples (Mancos, Marcellus and Pottsville shales) have iron concentration in trace amounts. Manganese (Mn) concentration followed the trend observed in Iron with the Wilcox shale having a disproportionate concentration of Mn in the solution compared to the other three samples. This can be seen in figure 4.12 with the concentration declining exponentially during the five-day experiment. The concentration of Mn in the effluent recovered

for the Mancos, Marcellus and Pottsville shales were in trace amounts though the Wilcox's fifth day concentration rapidly approached the range for these other samples. The concentration of Mn in the Wilcox indicate a rapid reactive interaction of the manganese bearing minerals in the shale rock with CO₂ saturated brine leading to free manganese cations in solution. The elemental concentration of Nickel (Ni) and Phosphorus (P) showed a trend of trace element consumption similar to K, Al, B and As for the Marcellus and Wilcox shales while the Ni and P concentrations of A and C appeared unchanged in the effluent when compared to the influent CO₂-brine fluid. Figures 4.13 and 4.14 showed the trace concentrations of Ni and P. These trace metals may be able to act as catalysts for surface and internal reactions in the sample rock pore spaces.

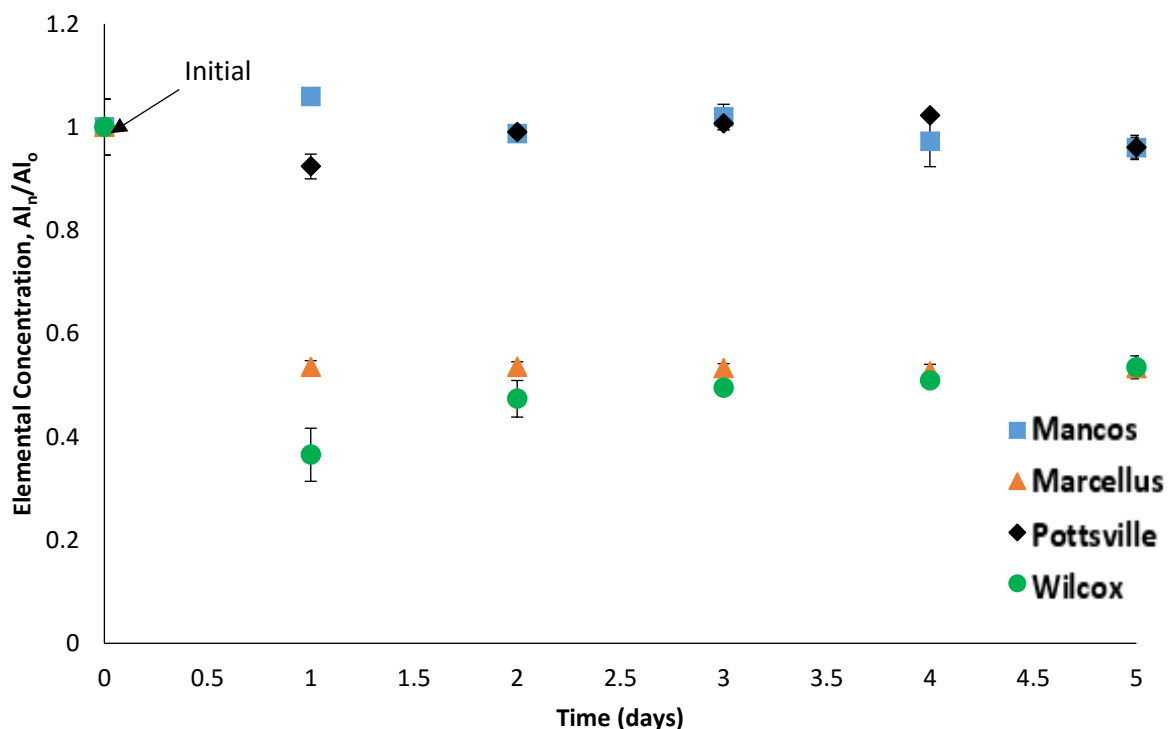


Figure 4.8: Dimensionless cationic concentration of the effluent fluids showing the fraction of Aluminum (Al) that were leached out from the shale rock samples. The trace concentrations of Al remained constant for the Mancos and Pottsville shale rocks. The Al profile for the Marcellus and Wilcox shale rocks were initially mildly reduced but later held constant during the last three days of the experiment.

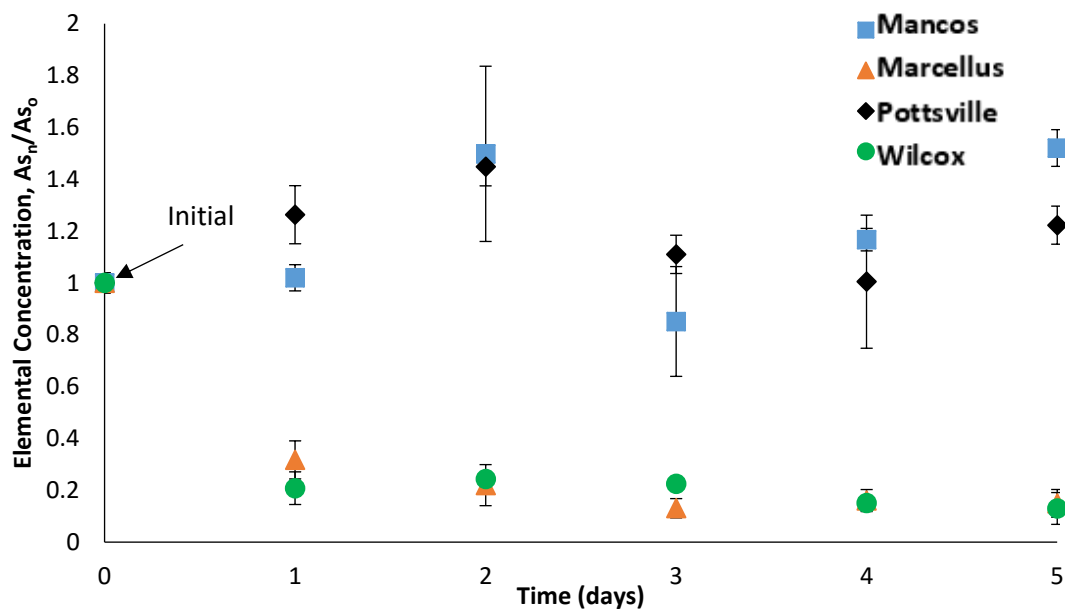


Figure 4.9: Dimensionless cationic concentration of the effluent fluids showing the fraction of Arsenic (As) that were leached out from the shale rock samples. The trace concentrations of As in the effluent fluid from the Mancos and Pottsville shale rocks significantly diverged from the Marcellus and Wilcox over the 5 day experiment plateauing out for all samples at end of the experiment.

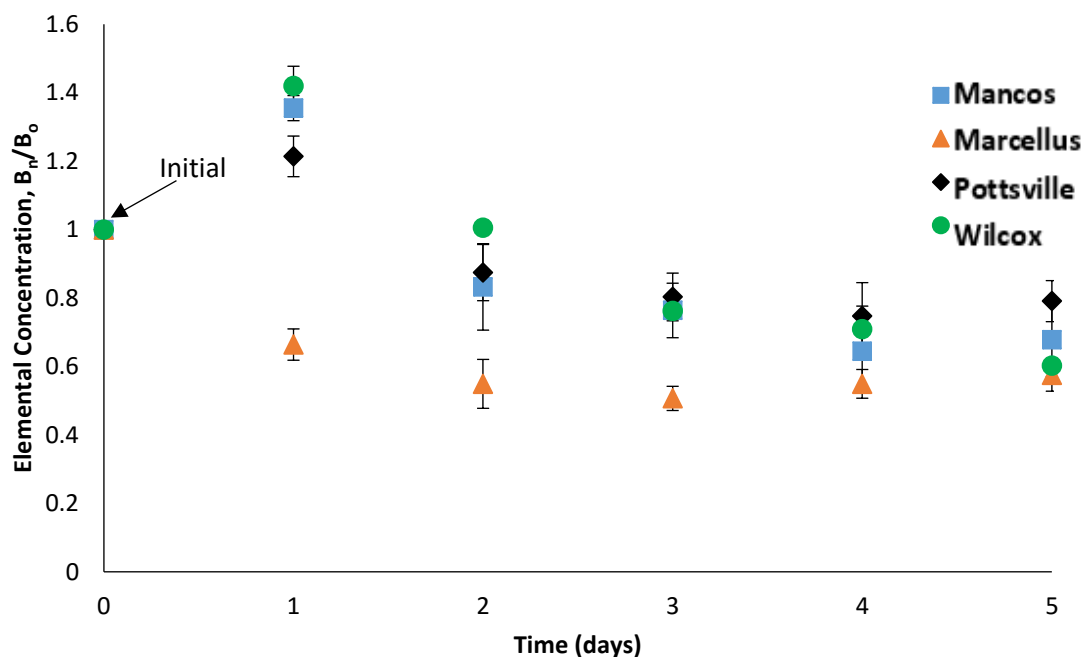


Figure 4.10: Dimensionless cationic concentration of the effluent fluids showing the fraction of Boron (B) that were leached out from the shale rock samples. The minor concentrations of Boron showed a common decreasing pattern for all the samples, stabilizing towards the end of the experiment at values that are lower than the initial.

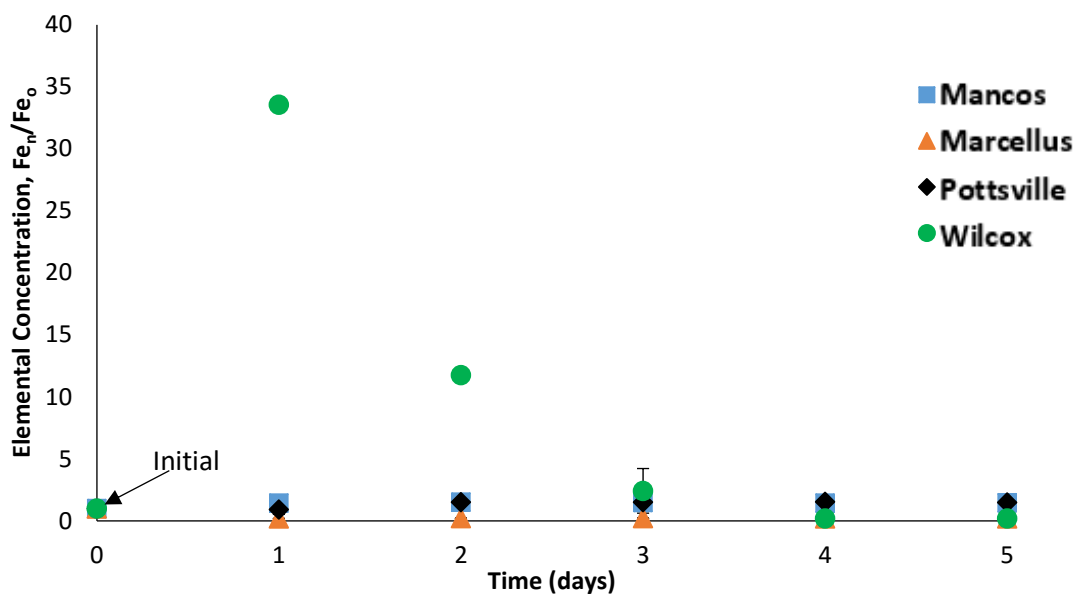


Figure 4.11: Dimensionless cationic concentration of the effluent fluids showing the fraction of Iron (Fe) that were leached out from the shale rock samples. The trace Fe content profile showed that the Wilcox shale had a much higher fraction of Fe in solution compared to the other three samples. This Fe concentration rapidly reduced over time during the experiment.

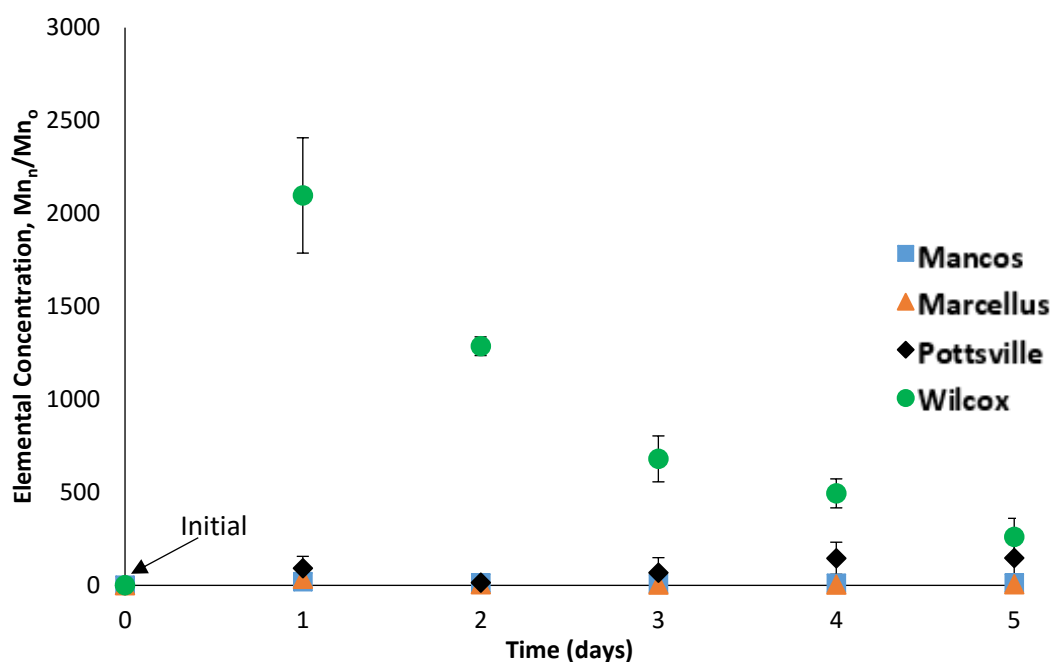


Figure 4.12: Dimensionless cationic concentration of the effluent fluids showing the fraction of Manganese (Mn) that were leached out from the shale rock samples. The Mn profile showed a much higher concentration of Mn in the effluent associated with the Wilcox shale rocks compared to the other three samples. This Mn concentration rapidly reduced over time during the experiment.

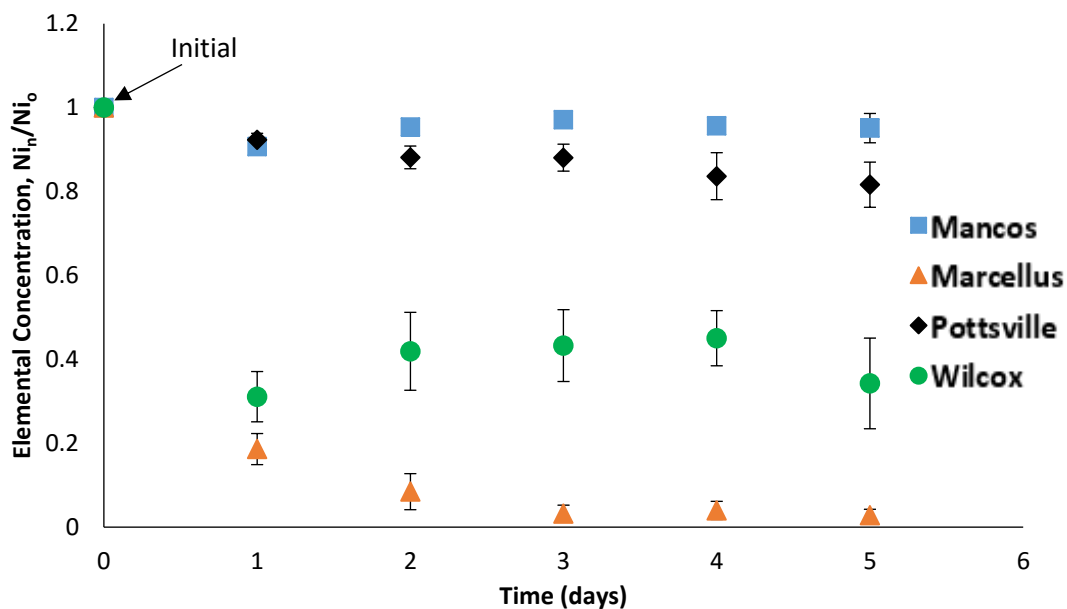


Figure 4.13: Dimensionless cationic concentration of the effluent fluids showing the fraction of Nickel (Ni) that were leached out from the shale rock samples. The trace profile for Ni indicated that the Marcellus and the Wilco shales had a mild decrease in the associated effluent compared to the initial CO₂-brine fluid. Nickel concentration remained constant for the Mancos and Pottsville shale rocks.

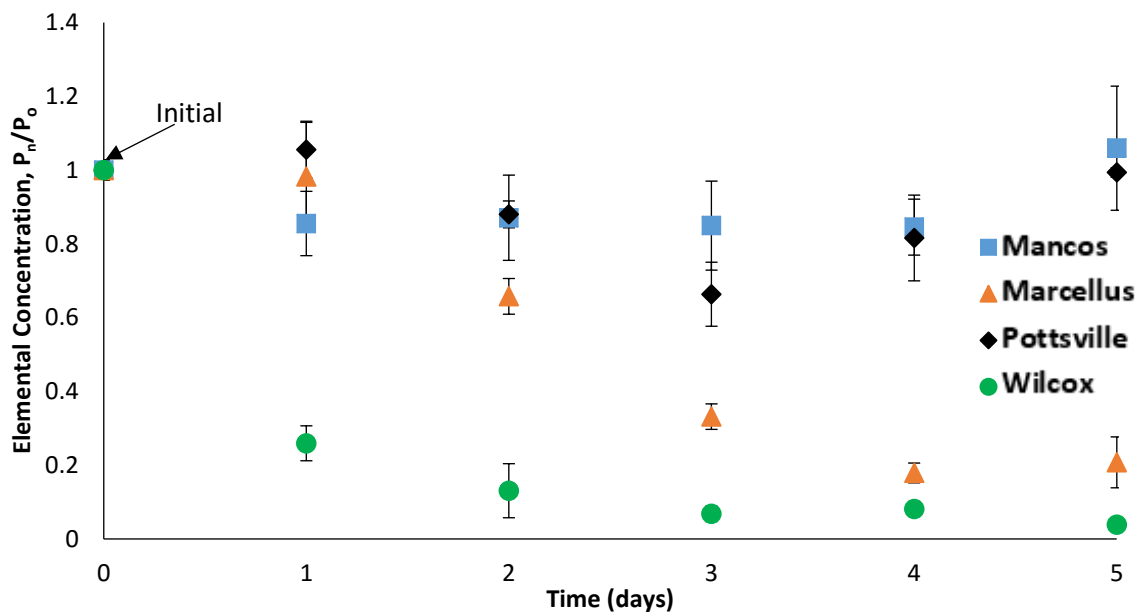


Figure 4.14: Dimensionless cationic concentration of the effluent fluids showing the fraction of Phosphorus (P) that were leached out from the shale rock samples. The trace profile for P indicated that the Marcellus and Wilcox shale rocks had a mild decrease in the associated effluent compared to the initial CO₂-brine fluid. Phosphorus concentration remained fairly constant for the Mancos and Pottsville shale rocks.

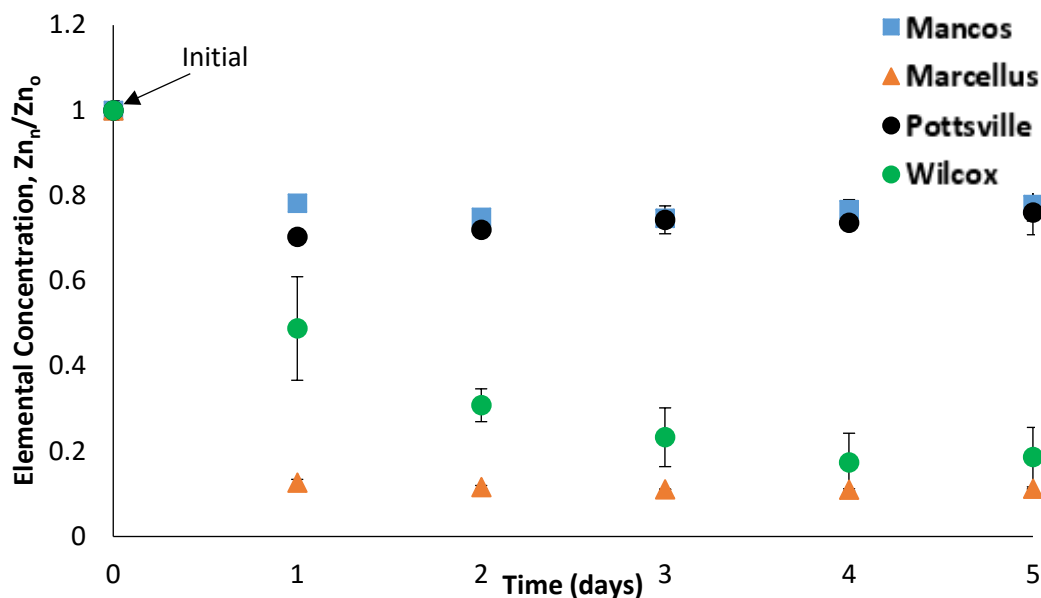


Figure 4.15: Dimensionless cationic concentration of the effluent fluids showing the fraction of Zinc (Zn) that were leached out from the shale rock samples. The concentration of Zn in the effluent fluid associated with all the shale samples decreased compared to the initial CO₂-brine fluid. This decrease is most pronounced in the Marcellus and Wilcox shale rocks.

Figure 4.15 shows the concentration profile for Zinc (Zn) that not only has a trend similar to that of Ni and P described above, it was also a trend of persistent concentration reduction for all the four samples analyzed. This indicates that Zn is most-likely participating in geochemical reactions as a facilitating components given its trace concentration.

4.3 Total Carbon Analysis

The total carbon contents of all the four samples were analyzed for the three runs per sample experiment at moderate temperature and pressure conditions. Figure 4.16 shows the Marcellus shale as having the highest percentage of carbon compared to other samples as expected for a highly fossiliferous shale rock. The percentage carbon content were in the order Marcellus >

Wilcox > Mancos > Pottsville. This order of magnitude still holds after the CO₂-brine flooding experiment. It can be observed for the figure that were significant increases in the percentage content of carbon in all the samples which can be indicative of both adhered carbon and mineralized carbon in the these shale samples. This might be good for carbon sequestration.

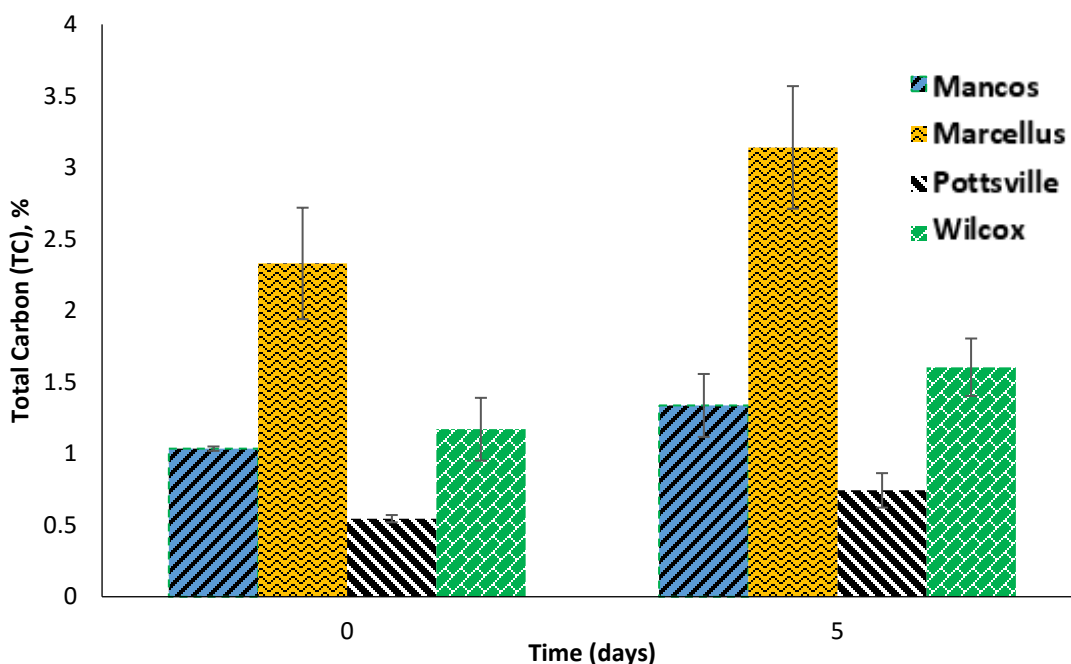


Figure 4.16: Total Carbon measurement of bulk rock for the four different samples analyzed. It shows major increase in carbon content for the Marcellus shale compared to the other three samples. This increases can be associated with surface CO₂ adsorption or carbon mineralization.

It suggests that shale caprock can act like repositories for CO₂ when sufficient surface area are available for rock fluid interaction. The surface area of the shale caprock exposed in these experiments are equivalent of several thousand meter square. Subsurface CO₂ plume movement will be contact seal rocks in this manner and scope. Distinguishing between adhered carbon and mineralized carbon content might shed more light on which process- adsorption or mineralization- will be most significant for CO₂ sequestration in shaly rocks over the long term.

The error bars are standard deviation (SD) values for the three runs per sample experiments. The total carbon analysis is more qualitative than quantitative for conclusive interpretations.

4.4 X-Ray Diffraction (XRD) Analysis

X-ray diffraction (XRD) analysis were carried on the bulk rock and the precipitates that were recovered from the effluent fluid. Both bulk and clay XRD analysis were performed in order to decipher the minerals that are most active in rock-fluid interaction and their implication on precipitates generation which can be transported in solution. These precipitates are of interest as hydraulic paths (micro-fractures, worm holes etc.) may be possibly plugged if the right quantity are generated from the bulk rock as dissolved substances. These dissolved minerals can then precipitate given the right pH, pressure, temperature, compositional and other conditions. The following sections (4.4.1 and 4.4.2) discuss the XRD analyses in details.

4.4.1 Bulk XRD Analysis

After the five days of flooding the shale rock samples continuously with CO₂ saturated brine at moderate temperature and pressure conditions, XRD analyses were carried out on the bulk experimental shale rock samples and the precipitates that were recovered from the effluent fluid with the aim of qualifying and quantifying geochemical changes that could have taken place as a result of reactive rock-fluid interaction. These geochemical changes are expected to affect the mineralogical composition and structure of the shale rocks. The results were compared to the initial shale rock samples that were not flooded with CO₂-brine. Figures 4.17 to 4.20 show the profiles of the main mineralogical components in the shale rocks (pre- and post-flooding with CO₂-brine) and the recovered precipitates as identified by bulk XRD analysis for the Mancos, Marcellus, Pottsville and Wilcox shale rocks respectively. The bulk shale rocks show little to no

change in mineralogical content pre- and post-flooding with CO₂-brine within the limit of XRD resolution. This was the observed trend in all the four samples. It can however be observed that the mineralogy identification peaks were better resolved in the post-flooding samples. It suggests that the amorphous content of the shale rocks have been largely removed by the acidic fluid. In the data reported by expert researchers in the field of carbon sequestration, defects or inherent errors in measuring equipment can affect the accuracy of XRD readings.

Amorphous content of rocks are usually responsible for suppressed peaks in XRD qualitative analysis. The bulk XRD analysis of precipitates showed the appearance of diagenetic minerals that were formed from the major mineralogical components of the shale rocks.

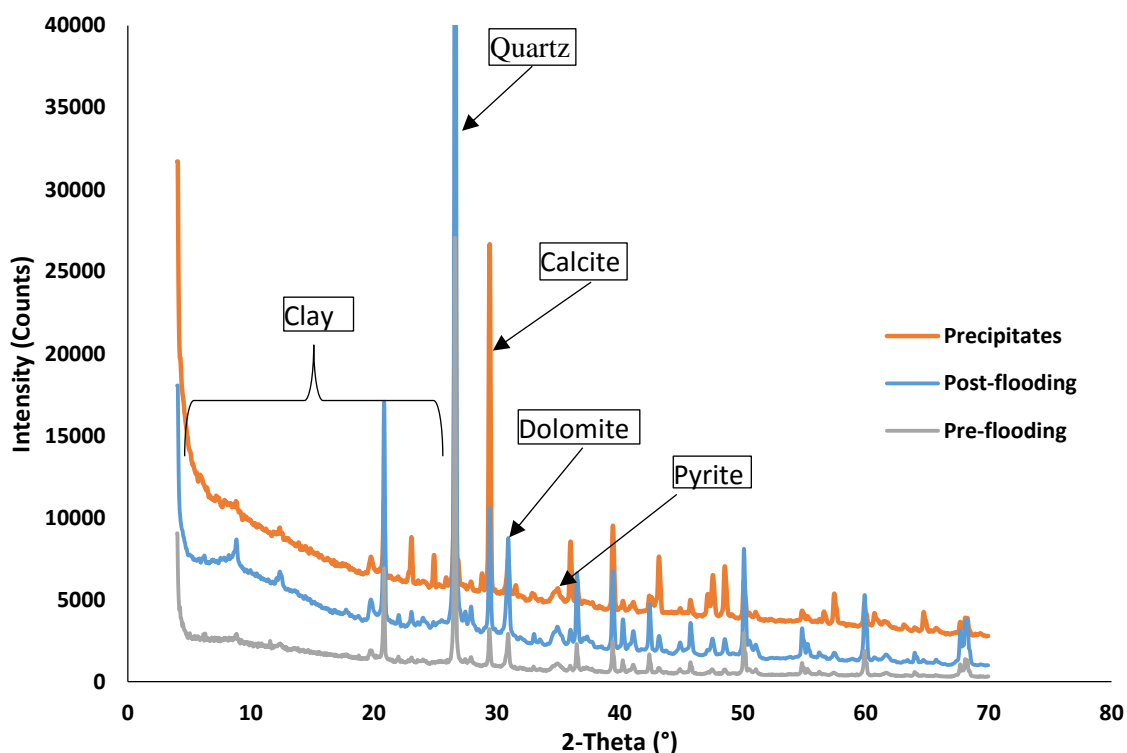


Figure 4.17: XRD Analysis of bulk rock (**Mancos**) before and after CO₂-brine flooding at moderate temperature and pressure conditions along with the mineralogical composition of the associated precipitates recovered from the effluent. It showed higher amount of diagenetic carbonates in the precipitates compared to the pre- and post-flooding samples.

Precipitate recovered from the effluent of flooding the Mancos shale with CO₂ saturated brine showed quartz, plagioclase, calcite, dolomite and pyrite as main constituent. This is excluding the clay fraction. Precipitates associated with the Marcellus shale included quartz aragonite and calcite only with no clay detected using XRD analysis. Precipitates associated with the Pottsville shale included quartz, albite and calcite while precipitates associated with the Wilcox shale included quartz, plagioclase and pyrite, excluding clay fractions from both samples. It can be seen from the bulk XRD output that mineral constituents of the original shale rocks are largely responsible for the diagenetic constituents of the associated precipitates which are dominated by quartz, calcites and clays.

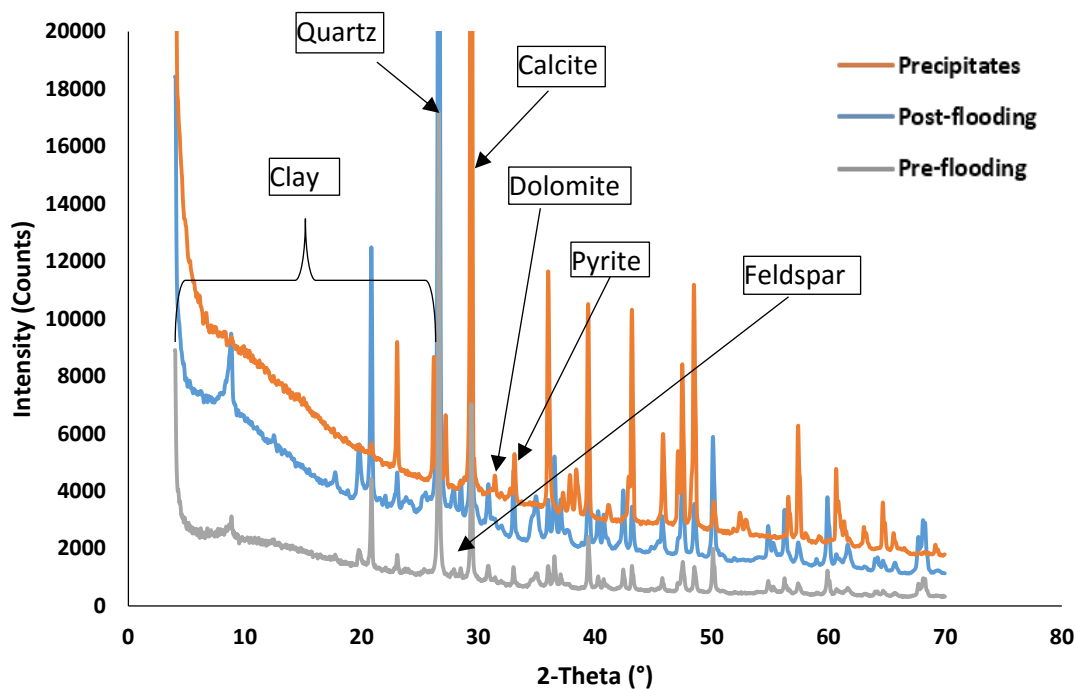


Figure 4.18: XRD Analysis of bulk rock (**Marcellus**) before and after CO₂-brine flooding at moderate temperature and pressure conditions along with the mineralogical composition of the associated precipitates recovered from the effluent. It showed higher amount of diagenetic carbonates in the precipitates compared to the pre- and post-flooding samples

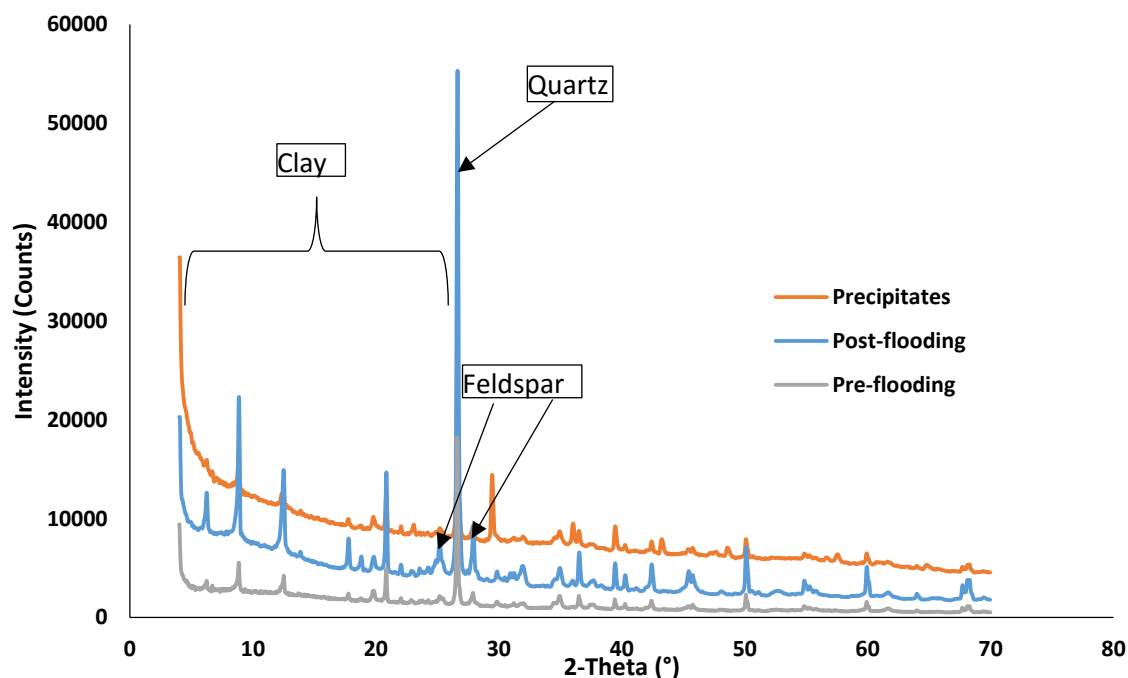


Figure 4.19: XRD Analysis of bulk rock (**Pottsville**) before and after CO₂-brine flooding at moderate temperature and pressure conditions along with the mineralogical composition of the associated precipitates recovered from the effluent. It showed higher amount of diagenetic quartz and clays in the precipitates versus the pre- and post-flooding samples.

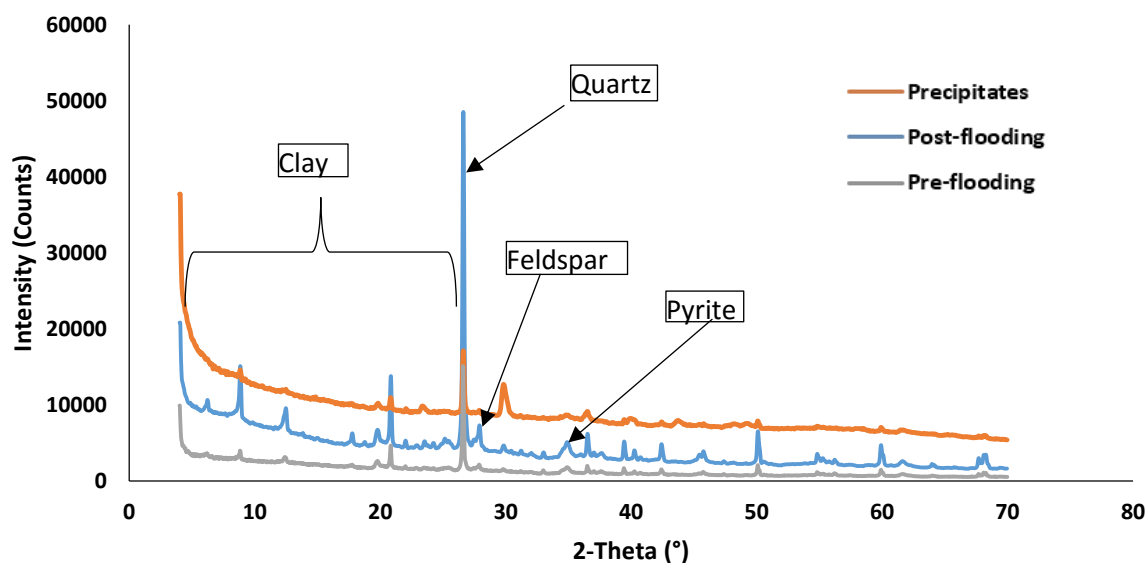


Figure 4.20: XRD Analysis of bulk rock (**Wilcox**) before and after CO₂-brine flooding at moderate temperature and pressure conditions along with the mineralogical composition of the associated precipitates recovered from the effluent. It showed higher amount of diagenetic quartz and clays in the precipitates versus the pre- and post-flooding samples.

The quantitative assessment of the mineralogical changes in the both the bulk shale rock and the precipitates are presented in section 4.4.3. The analysis of clay constituents in both the bulk rock and precipitates are presented in section 4.4.2.

4.4.2 Clay XRD Analysis

Clay XRD analysis is performed by first removing all other non-clay mineralogical contents in the shale rock. This is then followed by four stages of XRD analysis: a) Air dried analysis b) Glycolated analysis c) 300 Celsius analysis d) 550 Celsius analysis. These staged analysis are specifically important in quantitative clay content evaluation. The results of Ethylene glycolated samples are discussed in this section as it is representative of all the other stages in clay mineral identification. Figures 4.21 to 4.24 show the clay XRD analyses of the pre- and post-flooding samples as well as the recovered precipitates for all the four samples used during the experiment. The results showed sharper identification peaks for the clay minerals similar to the trend observed in bulk XRD analysis in the precipitates. An indication of non-interference of amorphous substances in mineral identification using XRD analysis.

The clay composition of the Mancos shale showed illite, chlorite and kaolinite as the main component (figure 4.21). The precipitates has mainly chlorite and kaolinite with traces of illite. Figure 4.22 indicated the presence of only Illitic clay and kaolinite in the bulk shale rock of the Marcellus shale with no identifiable clay peak in the precipitates associated with it. Clay fraction in Pottsville shale and the associated precipitates are presented in figure 4.23 showing the multiple identification peaks of illites, chlorite and kaolinite in the shale bulk rock and the associated precipitates recovered after the CO₂ brine flooding experiment. The Wilcox shale rock

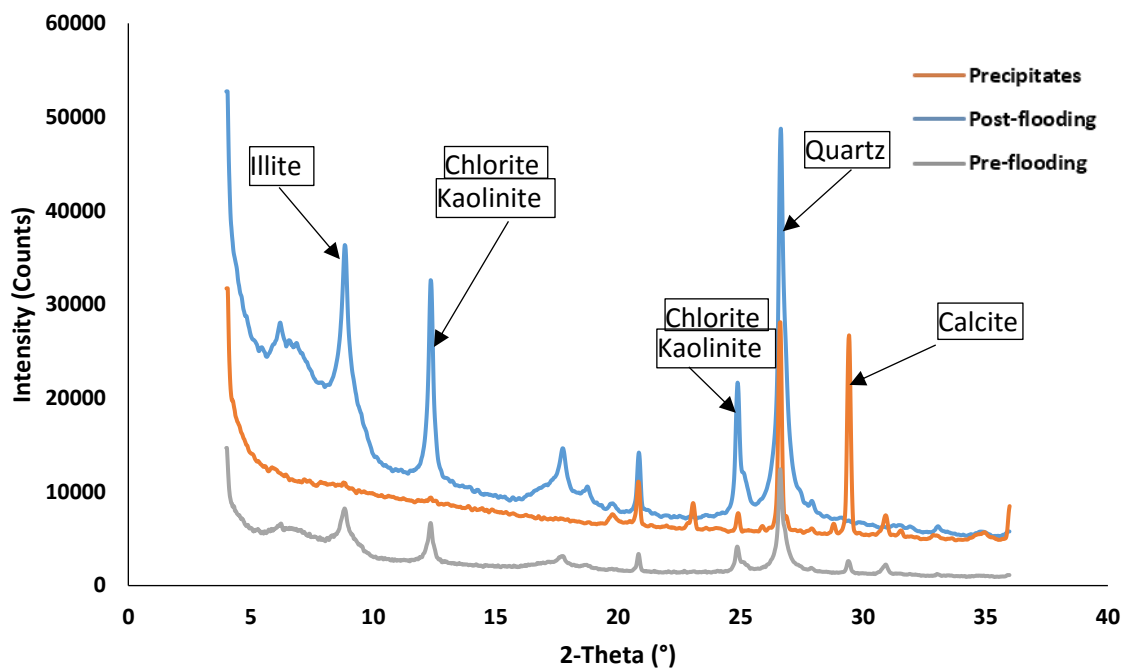


Figure 4.21: XRD Analysis of clay components (**Mancos**) before and after CO₂-brine flooding at moderate temperature and pressure conditions along with the mineralogical composition of the associated precipitates recovered from the effluent. It showed sharper clay peaks in post-flooding data and higher carbonate content in the precipitates.

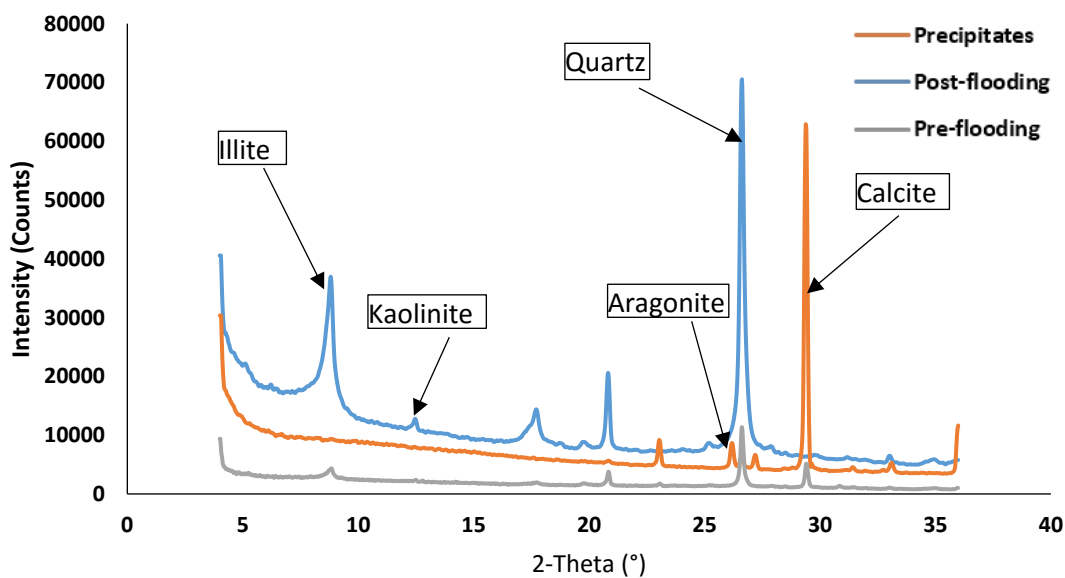


Figure 4.22: XRD Analysis of clay components (**Marcellus**) before and after CO₂-brine flooding at moderate temperature and pressure conditions along with the mineralogical composition of the associated precipitates recovered from the effluent. It showed sharper clay peaks in post-flooding data and higher diagenetic carbonate content in the precipitates.

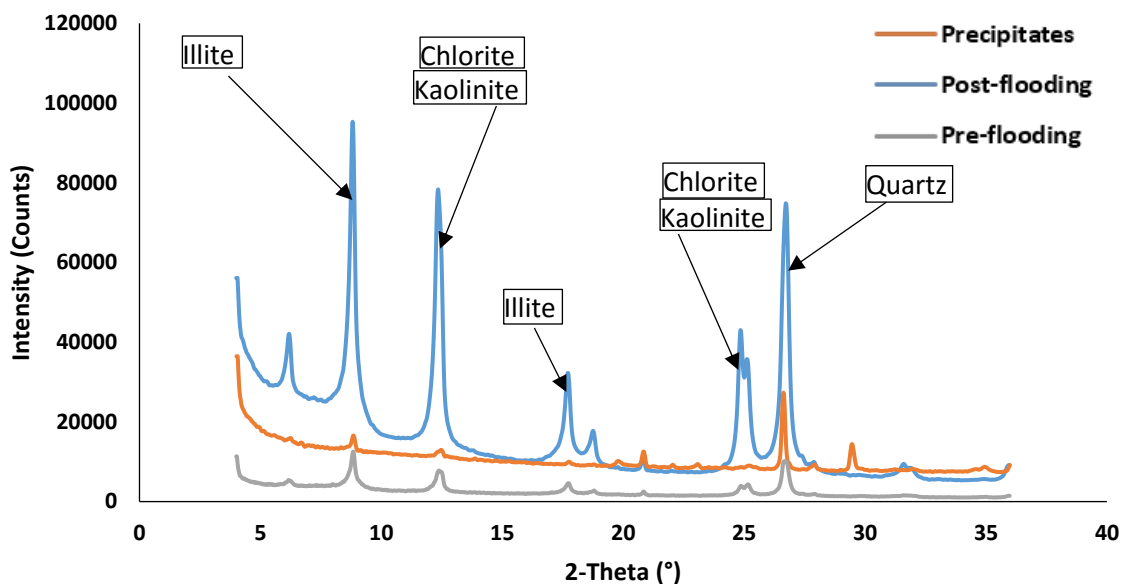


Figure 4.23: XRD Analysis of clay components (**Pottsville**) before and after CO₂-brine flooding at moderate temperature and pressure conditions along with the mineralogical composition of the associated precipitates recovered from the effluent. Significantly higher clay content is present in precipitates compared to previous samples.

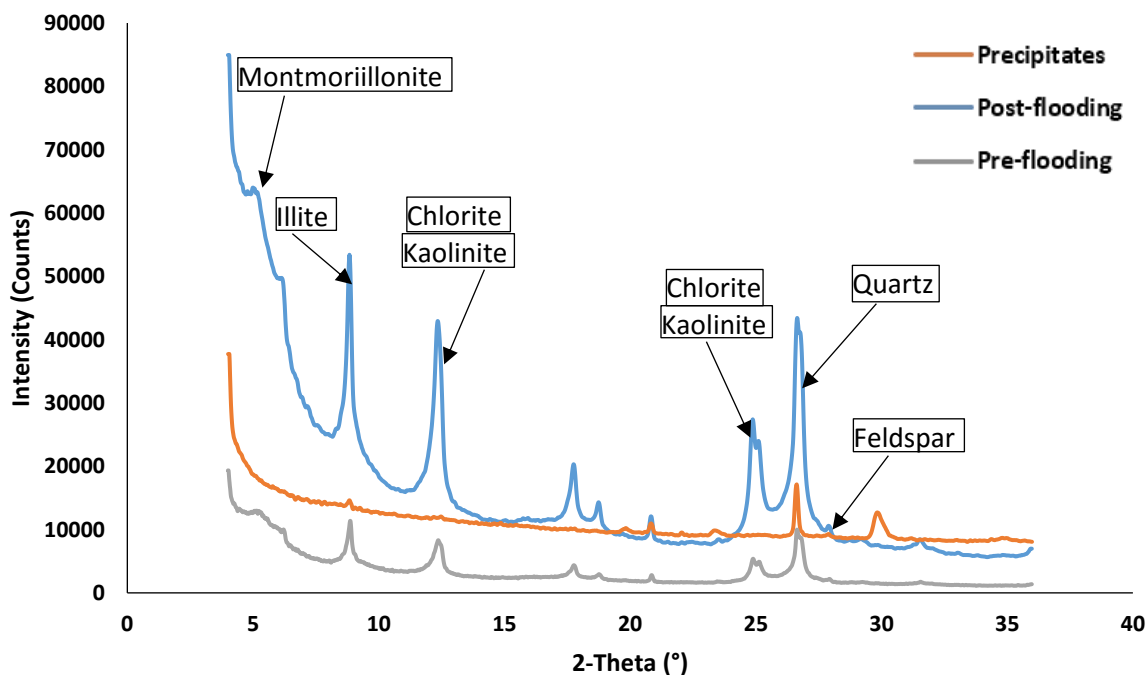


Figure 4.24: XRD Analysis of clay components (**Wilcox**) before and after CO₂-brine flooding at moderate temperature and pressure conditions along with the mineralogical composition of the associated precipitates recovered from the effluent. Significantly higher clay content is present in precipitates compared to previous samples combined with pyrite.

as shown in figure 4.24 indicated the presence of four distinct clay fractions which are montmorillonite (a characteristic swelling clay), illite, chlorite and kaolinite. The dissolution and re-precipitation of siliciclastic minerals such as illitic clays and quartz show that acidified aqueous media such as CO₂-brine can effect disequilibrium conditions. The qualitative results from the clay analysis of the shale bulk rock and the associated precipitates recovered from effluent fluid after CO₂-brine flooding indicated that the clay composition of the shale rocks are not significantly diagenetically modified at the operating laboratory conditions of the moderately high temperature and injection pressure (50 Celsius and 1000 psi).

4.4.3 Quantitative XRD Mineralogical Analysis

Quantitative evaluation of the changes in mineralogical content of the shale rocks are presented in table 4.1. It can be seen that non-clay minerals that are compounds of alkaline earth metals (Ca, Mg, Fe) such as calcite, dolomite, pyrite and feldspar are significantly altered, mostly a reduction in percentage within the accuracy of quantitative XRD analysis.

Mancos shale had reductions in feldspar, dolomite, pyrite and total clay (particularly illite and kaolinite). There was a slight increase in quartz, plagioclase, calcite, and chlorite in the Mancos shale. The Marcellus shale had reductions in feldspar, plagioclase, calcite, dolomite, anhydrite and kaolinite, while its quartz, chlorite and illite content increased. Furthermore, bulk shale rock of Pottsville shale had reductions in anhydrite, chlorite and illite with associated increases in quartz, feldspar, plagioclase and kaolinite. The Wilcox shale had mineralogical reductions in feldspar, anhydrite, pyrite, chlorite and kaolinite with associated increases in quartz, plagioclase, illites and swelling clay montmorillonite. It can be observed that significant reduction in total clay component in most of the samples analyzed was accompanied with significant increases in quartz

fraction of the mineralogy. This was a strong indication of diagenetic alteration of shale rock minerals due to aqueous CO₂-shale rock interaction under laboratory temperature and pressure conditions. The flow rate was set to a value that would replicate convective fluid transport in the subsurface. This type of flow characteristics represent long term scenarios.

Table 4.1: Bulk rock compositional change (in percentages) for the shale rock samples. These values were computed from the pre- and post-XRD quantitative analysis using the bulk and clay XRD methods. There were slight changes in quartz, carbonates and clay contents.

Component		Mancos(%)	Marcellus(%)	Pottsville(%)	Wilcox(%)
Quartz		1.25	0.61	11.19	5.57
K-Feldspar		-0.07	-0.8	0.86	-0.12
Plagioclase		0.18	-0.15	3.3	1.13
Calcite		1.04	-8.29	0	0
Dolomite		-0.65	-0.57	0	0
Anhydrite		0	-0.41	-1.2	-1.02
Pyrite		-0.74	0.56	0	-1.79
Clay(total)		-1.01	9.04	-14.15	-3.77
	Chlorite	0.4	0.18	-4.64	-0.88
	Illite	-1.17	10.12	-9.83	1.82
	Kaolinite	-0.24	-1.26	0.32	-5.44
	Montmorillonite	0	0	0	0.73

The mineralogical constituents of the precipitates that were recovered from the effluent during the shale/CO₂-brine flooding experiment are presented in table 4.2. The minerals were definitely derived from the bulk shale rocks showed diagenetic components that have elemental

compositions that indicated reactive dissolution-precipitation process occurred during the experiment. Precipitates from CO₂-brine flooding of the Mancos shale showed quartz, calcite and fine clays in nearly equal proportion. Precipitates from the Marcellus shale showed aragonite and calcite (both carbonates of calcium) as the sole component, indicating pronounced preferential dissolution of carbonates in this organics rich shale rock. Precipitates associated with the Pottsville and Wilcox shale rocks showed mainly clays and quartz with traces of calcite in that were probably formed from the dissolution of minor amount anhydrite present in the rocks by the CO₂-brine. Further clay analyses confirmed this compositions.

Table 4.2: Percentage composition of the mineralogical components of precipitates that were recovered from the effluent during the shale/CO₂-brine flooding experiment. The analysis indicated diagenetic quartz and carbonates as new minerals that were formed.

Minerals	Mancos(%)	Marcellus(%)	Pottsville(%)	Wilcox(%)
Quartz	30.15	1.8	43.56	39.39
K-Feldspar	-	-	-	-
Plagioclase	0.99	-	-	2.36
Albite	-	-	3.73	-
Aragonite	-	19.28	-	-
Calcite	38.06	78.92	3.07	1.22
Dolomite	4.1	-	-	-
Anhydrite	-	-	-	-
Pyrite	1.42	-	-	2.37
Clays (total)	25.28	-	49.64	54.66

4.5 Electron Micro-Probe Analysis (EMPA) of Bulk Rock

The geochemical surface imaging of the shale rocks using Electron Microprobe Analyzer (EMPA) technique revealed the nature of the changes to surface chemistry at micron scale and the possible transport and re-crystallization of secondary mineralogical textures. Polished thin sections of pre- and post- CO₂ flooding samples of the shale rocks were studied in order to map all the identifiable elemental component of the constituent minerals as applicable in sedimentary petrology. Figures 4.25 to 4.36 present the unique elemental maps for each of the shale caprock sample types.

Major element and select trace element compositions were determined by Electron Microprobe Analysis (EMPA). EMPA is one of several particle-beam techniques. A beam of accelerated electrons is focused on the surface of a specimen using a series of electromagnetic lenses, and these energetic electrons produce characteristic X-rays within a small volume (typically 1 to 9 cubic microns) of the specimen. Two dimensional maps were obtained for multiple elements that constitute the shale rocks, under operating conditions of accelerating voltage of 15 kV and beam current of 200 nA. The electron microprobe was run in mapping mode allowing automated analysis overnight. A total of four thin sections were mapped over a period of 4-5 hours each. Maps depict relative abundances of elements of interest, allowing the determination of compositional zones. The results showed the presence of Iron (Fe), Sodium (Na), Potassium (K), Silicon (Si), Carbon (C), Oxygen (O), Chlorine (Cl), Manganese (Mn), Calcium (Ca), Magnesium (Mg) and Aluminum (Al). They are present in rock minerals capable of exchanging ions with carbonic acid or aqueous CO₂. The elemental distribution of Ca and Mg in the reacted Mancos and Marcellus shales were lower within grain facies as shown in figures 4.25 to 4.27 and figures

4.28 to 4.30 (top row) respectively when compared to the corresponding control samples (bottom row). These were the surface maps for elemental spread involving CO₂-brine flooded samples. It has been noted that in addition to common alkali earth metals such as Na and K that

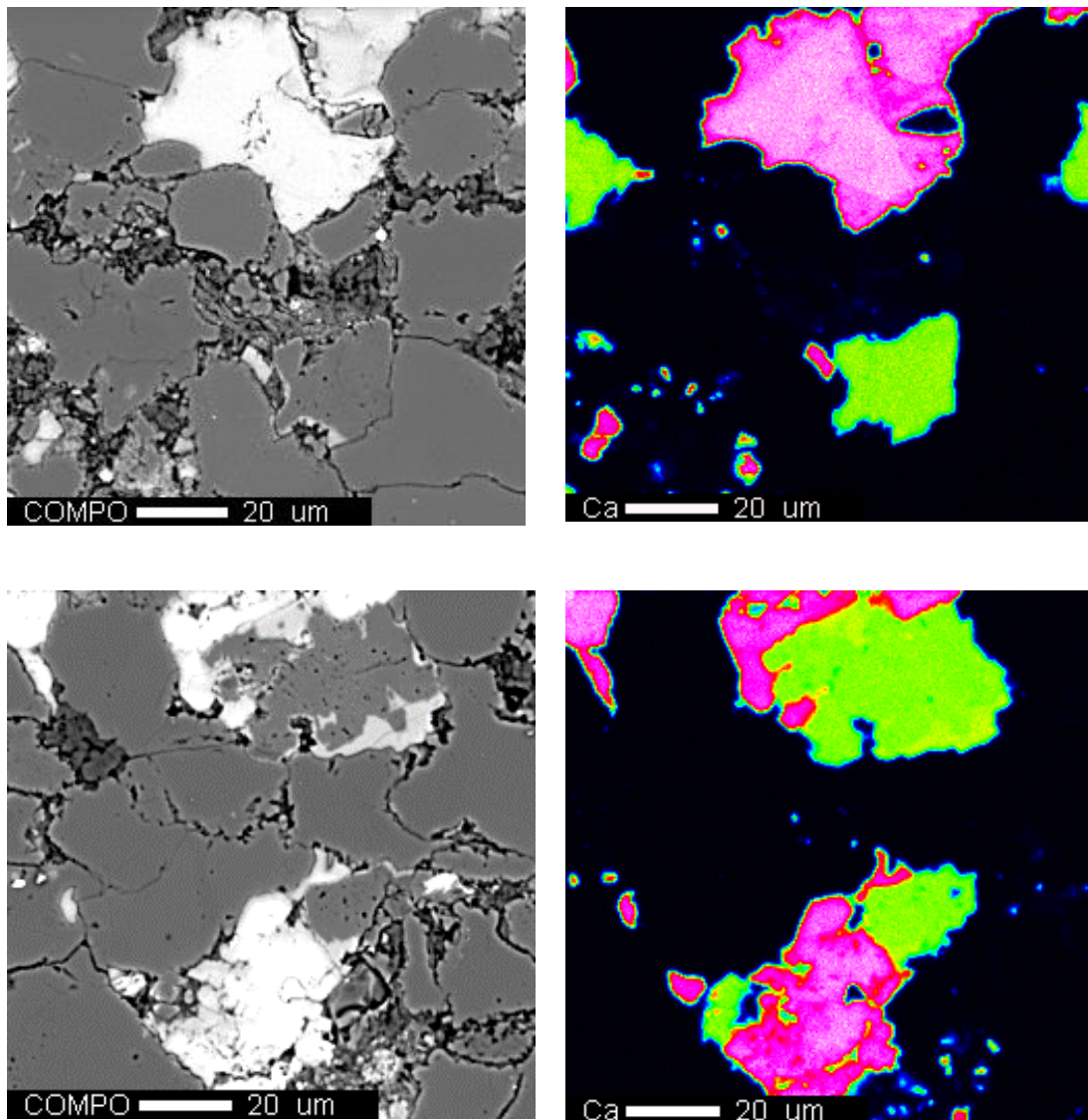


Figure 4.25: 20μm Electron Micro-Probe maps for **the Mancos shale** showing the Calcium (Ca) surface geochemical profile of the CO₂-reacted sample (top row) compared to control specimen (bottom row). Note the general depletion of elemental components that are associated with minerals that are susceptible to dissolution. These trends are only detected at the lower micron resolution presented above.

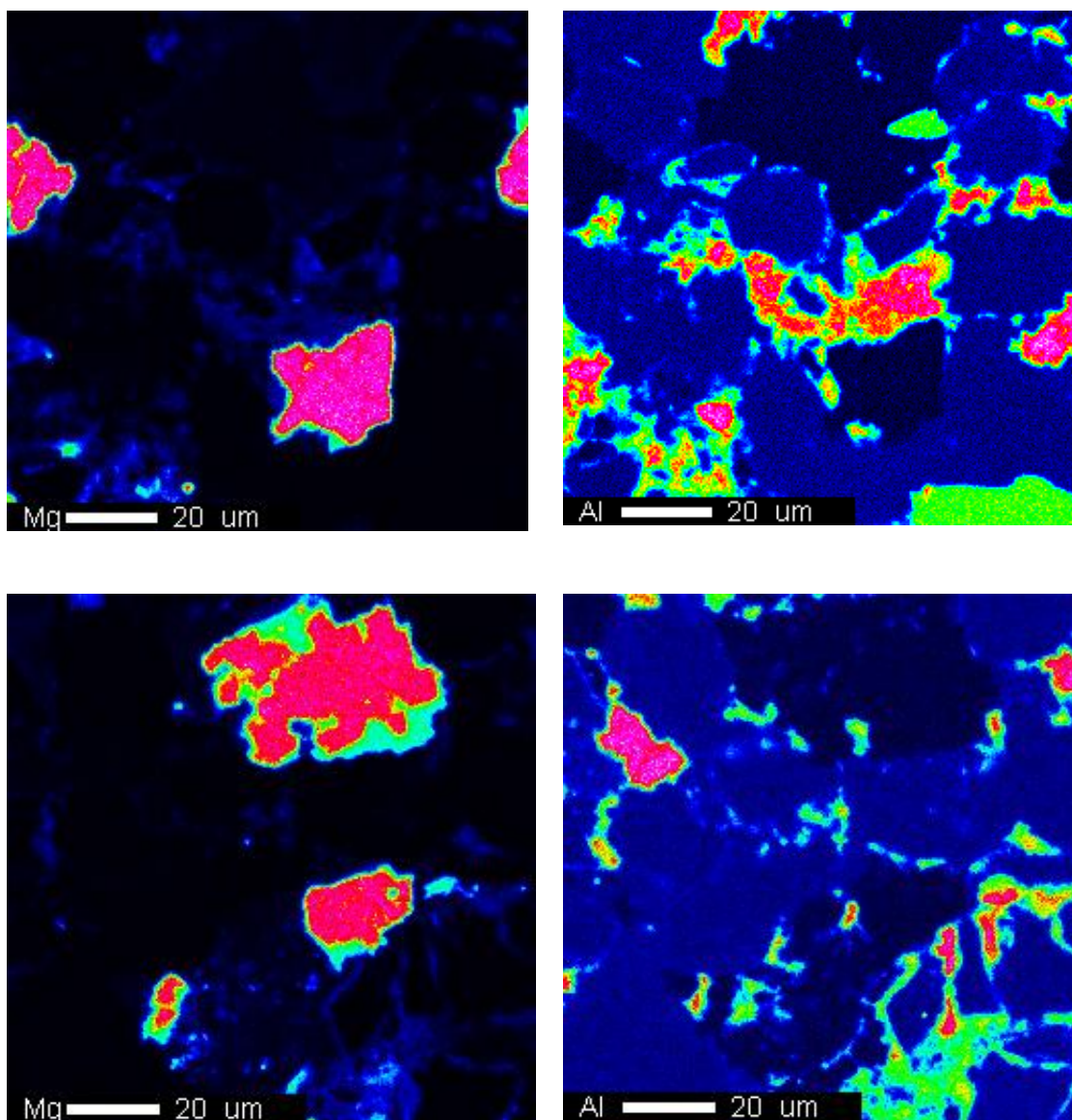


Figure 4.26: 20 μ m Electron Micro-Probe Analysis for **the Mancos shale** showing Magnesium (Mg) and Aluminum (Al) surface geochemical profile of the CO₂-reacted sample (top row) compared to control specimen (bottom row). Note the general depletion of elemental components that are associated with minerals that are susceptible to dissolution. These trends are only detected at the lower micron resolution presented above.

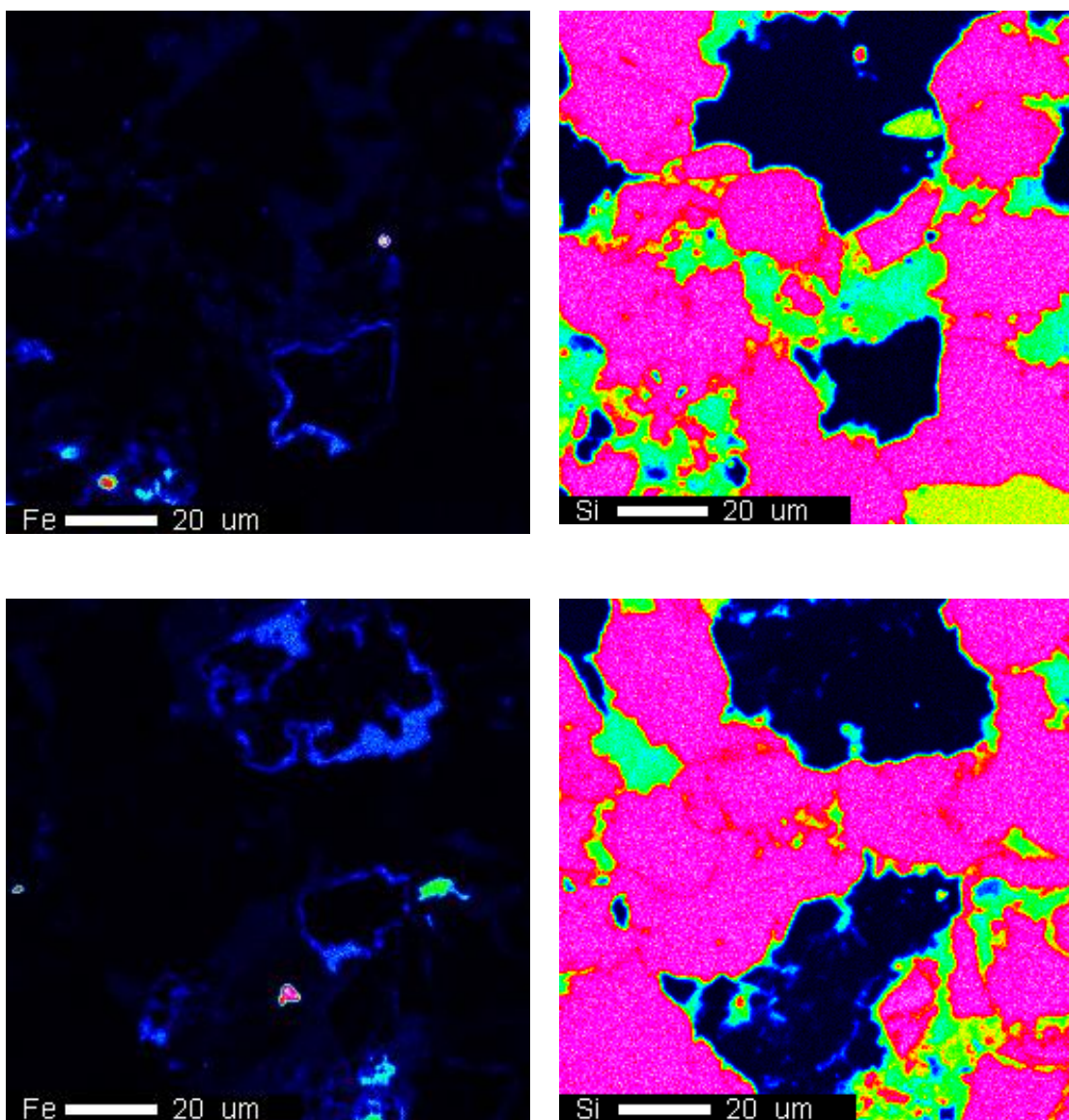


Figure 4.27: 20μm Electron Micro-Probe Analysis for **the Mancos shale** showing Iron (Fe) and silicon (Si) surface geochemical profile of the CO₂-reacted sample (top row) compared to control specimen (bottom row). Note the general depletion of elemental components that are associated with minerals that are susceptible to dissolution. These trends are only detected at the lower micron resolution presented above.

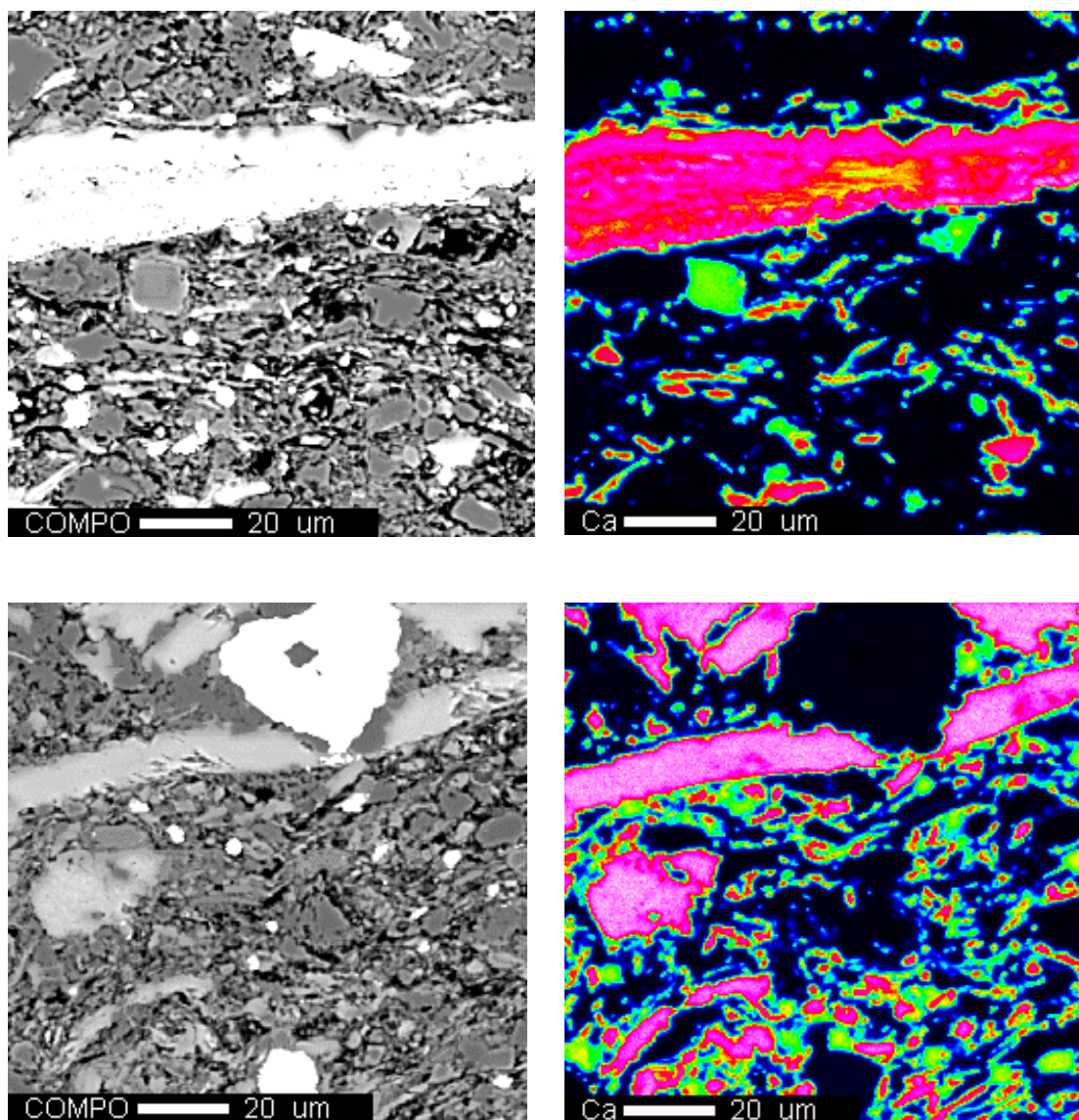


Figure 4.28: 20μm Electron Micro-Probe Analysis for **the Marcellus shale** showing the Calcium (Ca) surface geochemical profile of the CO₂-reacted sample (top row) compared to control specimen (bottom row). Note the general depletion of elemental components that are associated with minerals that are susceptible to dissolution. These trends are only detected at the lower micron resolution presented above.

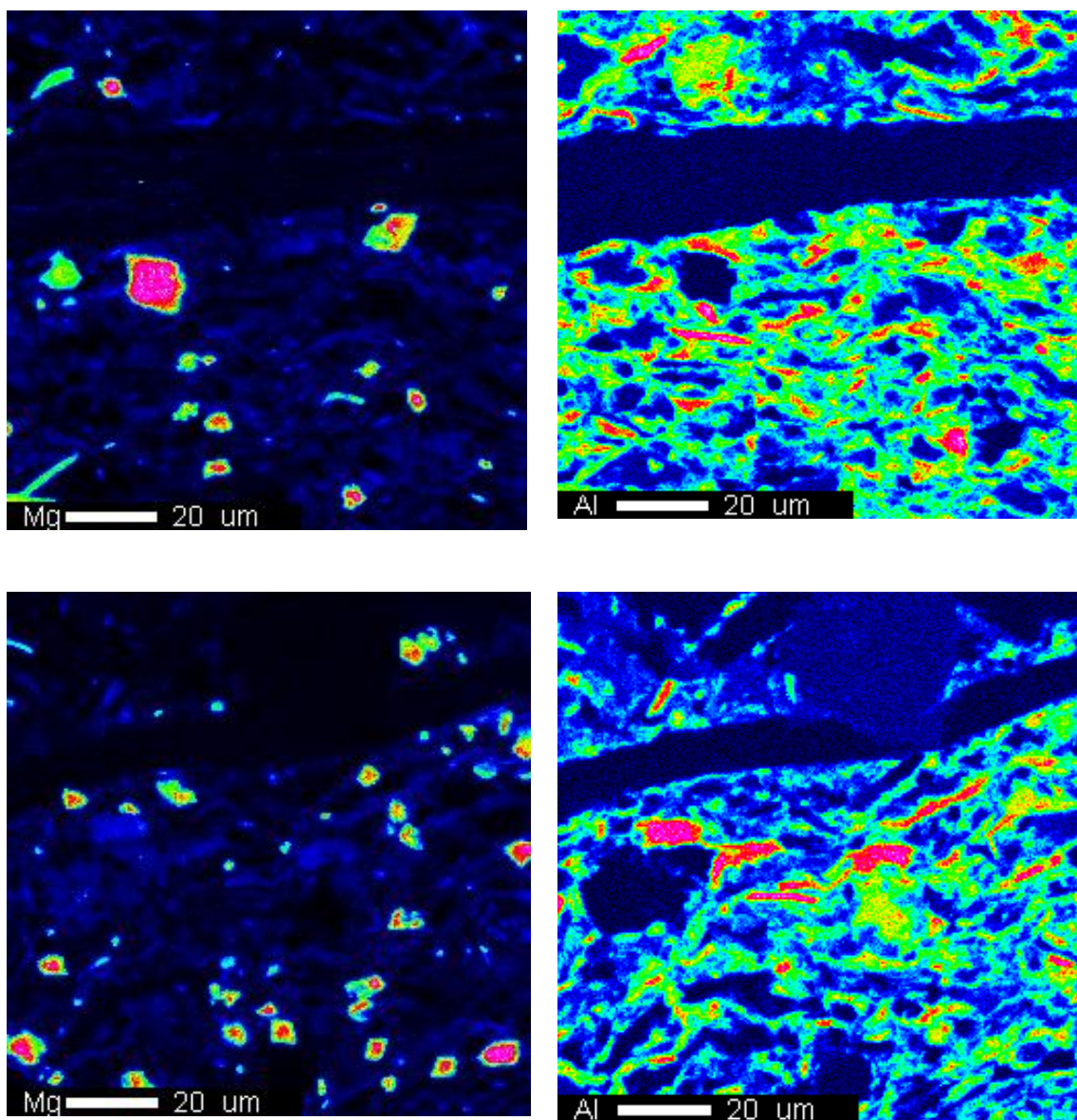


Figure 4.29: 20µm Electron Micro-Probe Analysis for **the Marcellus shale** showing Magnesium (Mg) and Aluminum (Al) surface geochemical profile of the CO₂-reacted sample (top row) compared to control specimen (bottom row). Note the general depletion of elemental components that are associated with minerals that are susceptible to dissolution. These trends are only detected at the lower micron resolution presented above.

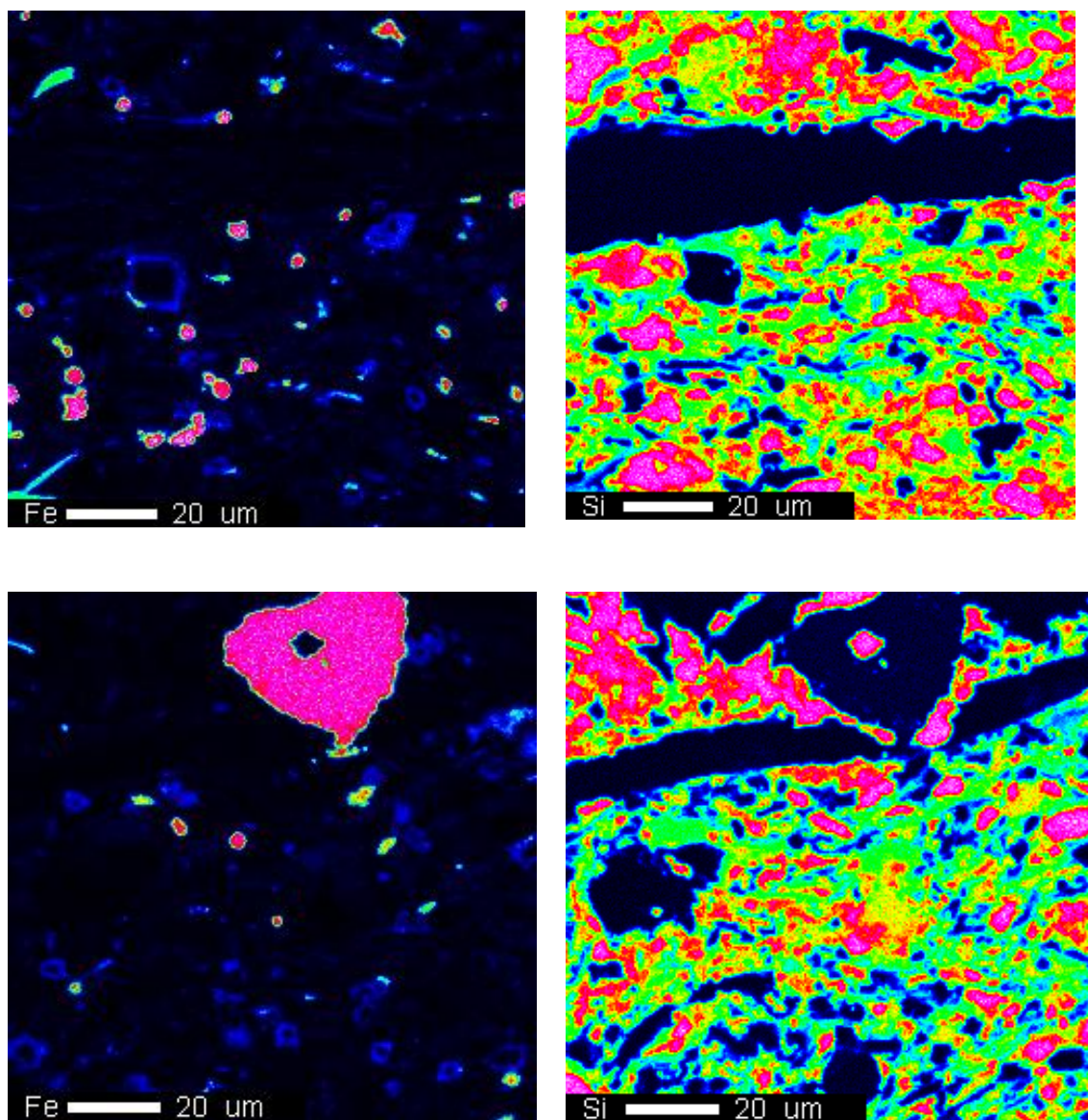


Figure 4.30: 20 μ m Electron Micro-Probe Analysis for **the Marcellus shale** showing Iron (Fe) and silicon (Si) surface geochemical profile of the CO₂-reacted sample (top row) compared to control specimen (bottom row). Note the general depletion of elemental components that are associated with minerals that are susceptible to dissolution. These trends are only detected at the lower micron resolution presented above.

form compounds which are generally soluble in acidic or alkaline fluids, Ca and Mg solutes have significant ion-exchange capacity as well. The surface depletion within grains show the extent of the reach of aqueous CO₂ in supporting dissolutive rock-fluid interaction in the subsurface. Pottsville and Wilcox shales are lean in Ca and Mg based minerals which informed the limited traces of these elements on the surface of the thin section samples. The distribution of Al and Fe as shown in figures 4.26/27 and figures 4.29/30 for Mancos and Marcellus shales respectively indicated low activity in the reacted samples while figures 4.31 to 4.33 and figures 4.34 to 4.36 for Pottsville and Wilcox shales respectively reflected significant concentration of Al and Fe which have smaller percentages in the minerals bearing them. These imply that compounds of Ca, Mg, Al, and Fe which were identified in the shale caprock samples, either as major or trace minerals, would be reactively soluble with faster kinetics in aqueous CO₂ with the possibility of re-precipitation to form new minerals at subsurface pressure and temperature. The formation of Aragonite in experiments involving Marcellus shale exemplify the dissolution-precipitation processes that impact long term caprock integrity. The ratio of the elements identified at the surface of the samples over the 5 days of CO₂-brine flooding showed mixed variations which could be partially attributed to mineral dissolution/precipitation and sample heterogeneity. Though the EMPA images were not shot on exactly the same rock piece thin section, the compared images in most of the specimen analyzed pointed to surface alterations as a result of reactive rock-fluid interaction in the shale rock samples. Additional data on these EMPA results are available in the appendix. Furthermore, the electron microprobe can function like a scanning electron microscope (SEM) and obtain highly magnified secondary- and backscattered-electron images of a sample under vacuum conditions.

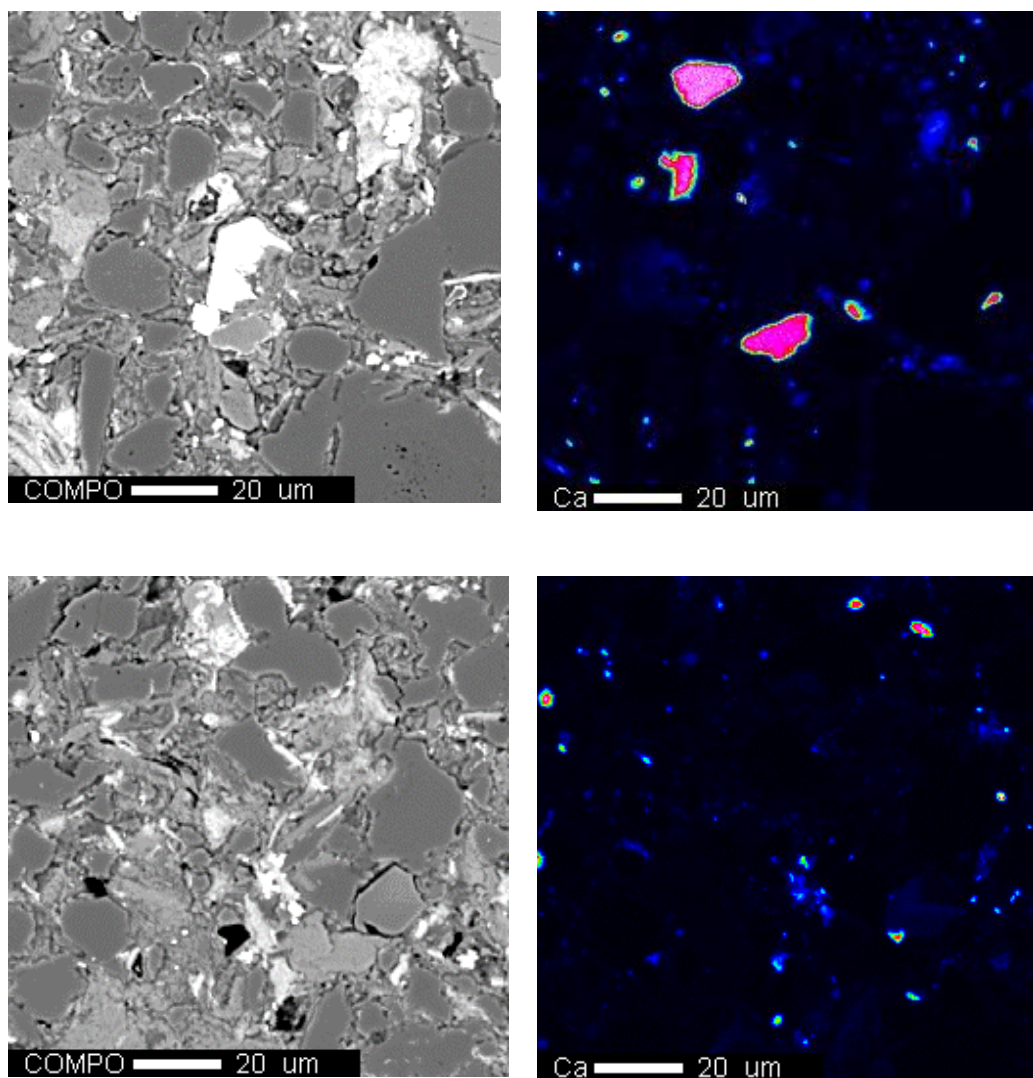


Figure 4.31: 20μm Electron Micro-Probe Analysis for **the Pottsville shale** showing the Calcium (Ca) surface geochemical profile of the CO₂-reacted sample (top row) compared to control specimen (bottom row). Note the general depletion of elemental components that are associated with minerals that are susceptible to dissolution. These trends are only detected at the lower micron resolution presented above.

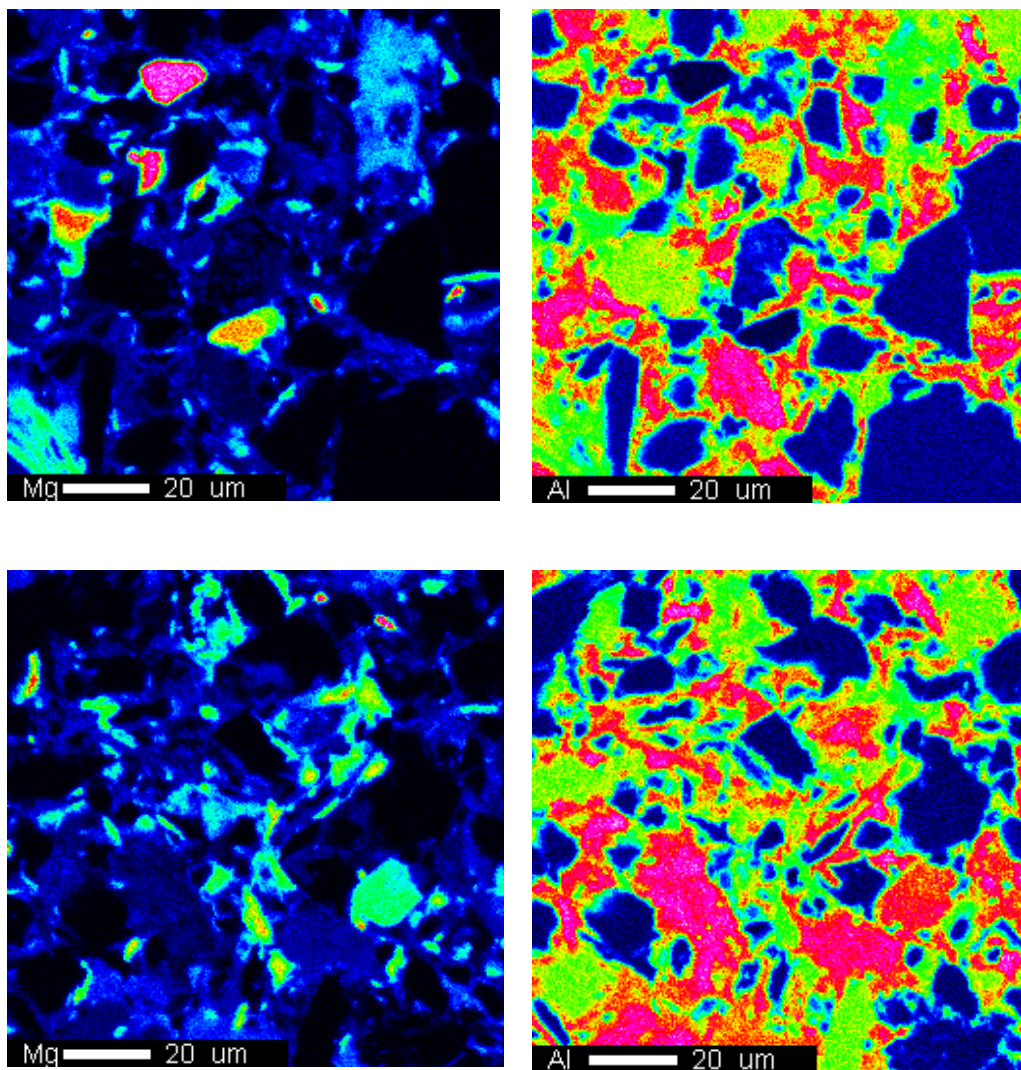


Figure 4.32: 20µm Electron Micro-Probe Analysis for **the Pottsville shale** showing Magnesium (Mg) and Aluminum (Al) surface geochemical profile of the CO₂-reacted sample (top row) compared to control specimen (bottom row). Note the general depletion of elemental components that are associated with minerals that are susceptible to dissolution. These trends are only detected at the lower micron resolution presented above.

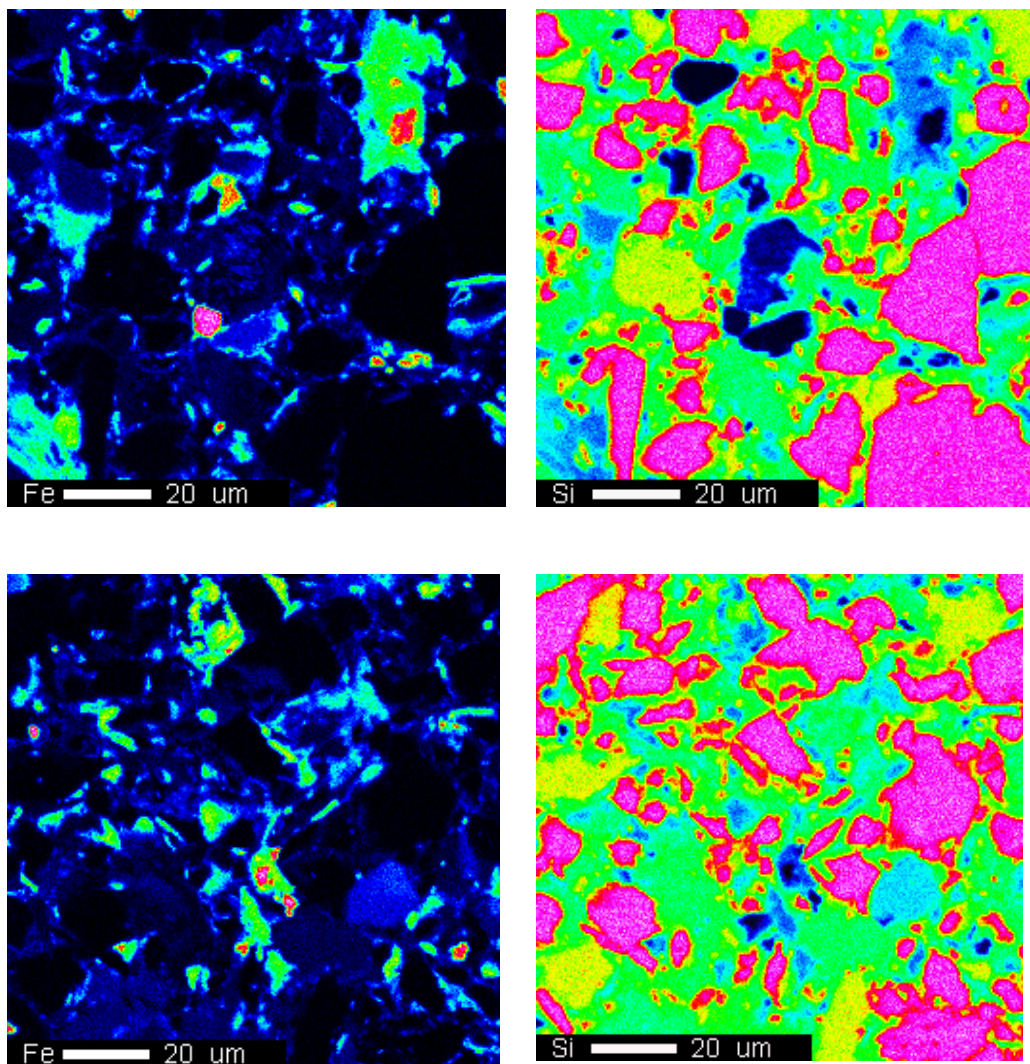


Figure 4.33: 20μm Electron Micro-Probe Analysis for **the Pottsville shale** showing Iron (Fe) and silicon (Si) surface geochemical profile of the CO₂-reacted sample (top row) compared to control specimen (bottom row). Note the general depletion of elemental components that are associated with minerals that are susceptible to dissolution. These trends are only detected at the lower micron resolution presented above.

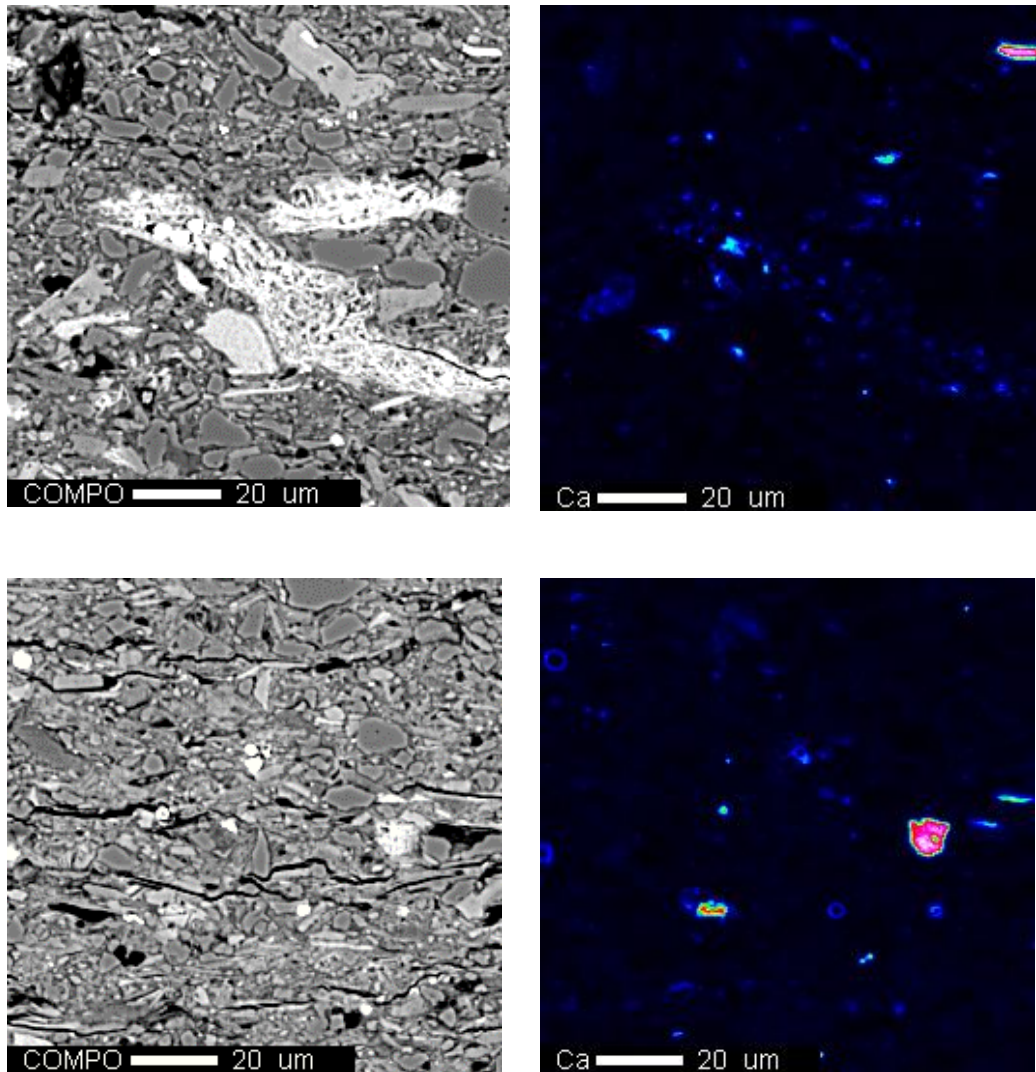


Figure 4.34: 20 μ m Electron Micro-Probe Analysis for **the Wilcox shale** showing the Calcium (Ca) surface geochemical profile of the CO₂-reacted sample (top row) compared to control specimen (bottom row). Note the general depletion of elemental components that are associated with minerals that are susceptible to dissolution. These trends are only detected at the lower micron resolution presented above.

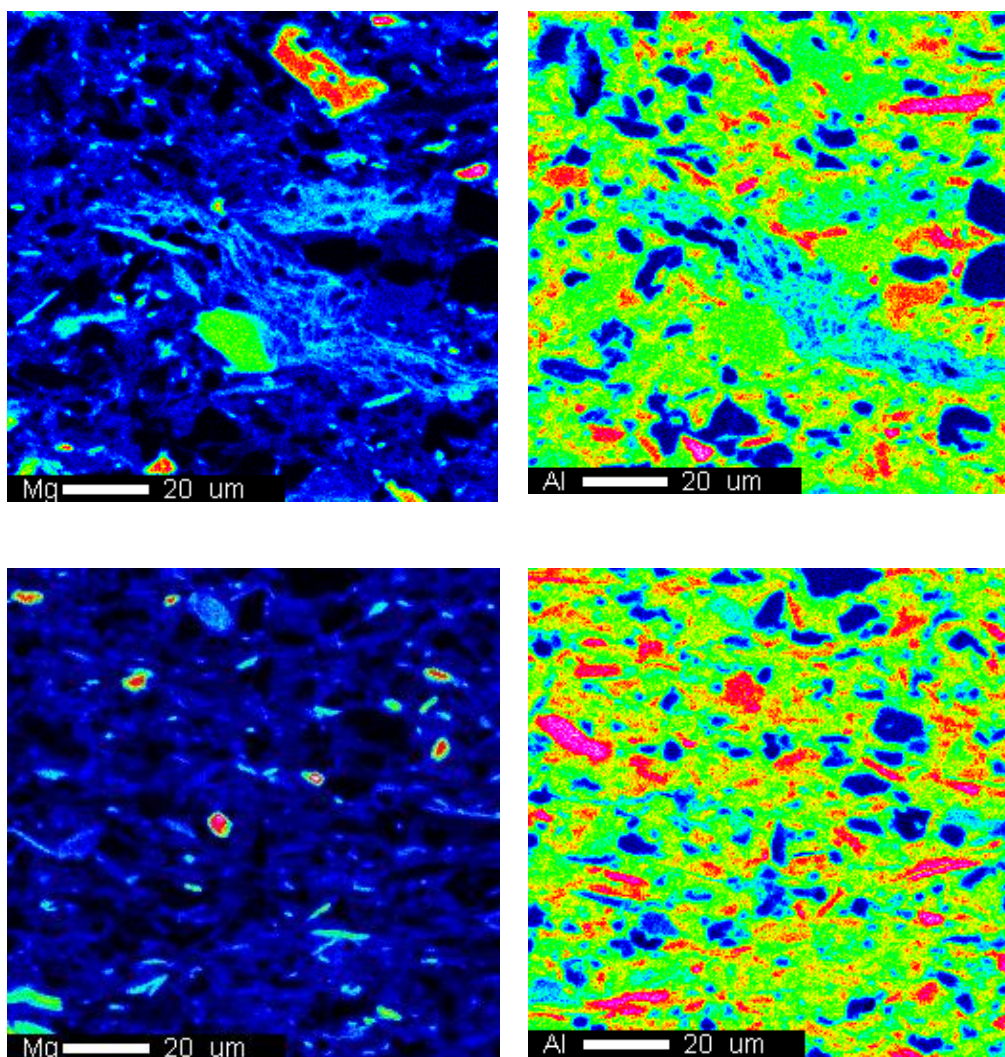


Figure 4.35: 20 μ m Electron Micro-Probe Analysis for **the Wilcox shale** showing Magnesium (Mg) and Aluminum (Al) surface geochemical profile of the CO₂-reacted sample (top row) compared to control specimen (bottom row). Note the general depletion of elemental components that are associated with minerals that are susceptible to dissolution. These trends are only detected at the lower micron resolution presented above.

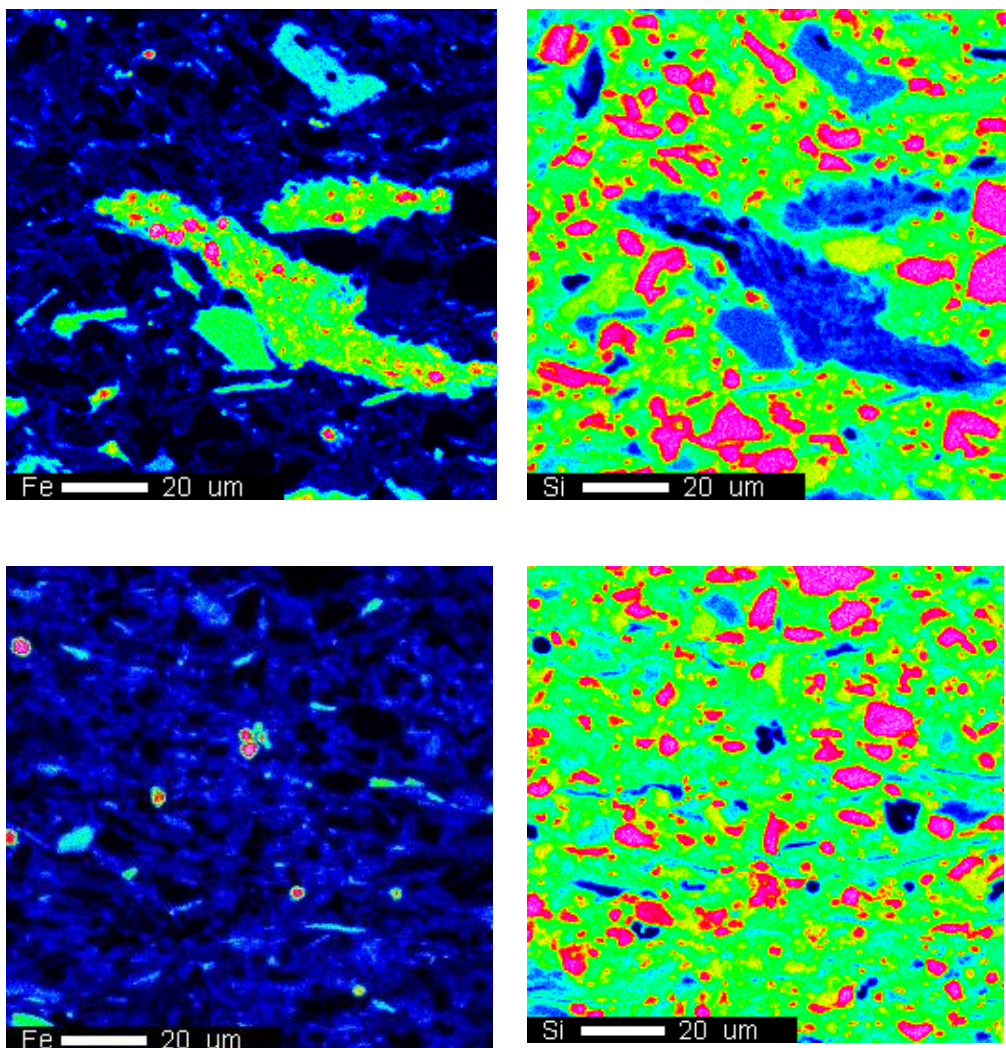


Figure 4.36: 20μm Electron Micro-Probe Analysis for **the Wilcox shale** showing Iron (Fe) and silicon (Si) surface geochemical profile of the CO₂-reacted sample (top row) compared to control specimen (bottom row). Note the general depletion of elemental components that are associated with minerals that are susceptible to dissolution. These trends are only detected at the lower micron resolution presented above.

4.6 Micro-Indentation of Rock Samples

Micro-indentation analyses were performed on polished samples of the shale rocks with the aim of determining the extent of possible changes in hardness level of the rocks after the CO₂-brine flooding experiment. The following set of conditions were used in all the indentation experiments: the maximum force used was 10 N; the loading and unloading rates were kept the same at 10 N/min; the pause at maximum load was 30 seconds; the contact load was 30 mN. The hardness was obtained with computational method from Oliver and Pharr [219]. The indenter type was Vickers' diamond with the Poisson coefficient of 0.07. There are scientific documentation of using this method for nano-indentation of pure clay minerals [220].

Figure 4.37 shows the Vickers' micro-hardness measurements acquired on the samples with the error bar equivalent of standard deviation (SD) from three experimental runs per sample. There was noticeable decrease in the hardness of the Mancos, Marcellus and Wilcox shale rocks in that order with the Pottsville shale showing little to no change at the moderate temperature and pressure conditions in which the experiments were performed.

This might indicate a weakening of the shale rocks under carbon sequestration conditions in the case of pervasive CO₂ intrusion into the overlaying caprock or most importantly at the seal rock-reservoir rock interphase where the impact of the injected CO₂ plume will be most significant. The impact of higher temperature and pressure conditions is recommended to be investigated in subsequent experimental research involving shale-aqueous CO₂ interactions. Experimental set up for the indentation is annotatively explained in the appendix A. Figures 4.38 shows the Young's Modulus equivalent of the Vickers' hardness and figure 4.39 attempted to combine the two parameters. YM and HV refers to Young's Modulus and Vickers' Hardness respectively. The

results show loss of geomechanical hardness particularly for the samples that are most susceptible to dissolution i.e. The Mancos and Marcellus shale rocks. The significant difference between the profiles of the Young Modulus and Vickers' Hardness is explained in the computation properties of the rock used. Vickers' Hardness captured more variations in the properties of the reacted samples when compared with the controls after the five days of the experiment. These two properties have been shown in other data acquired on engineered materials not to have any correlation. They were independently analyzed in this section for the impact of geochemical changes at the surface. Heterogeneity in material composition is believed to have significant effect on the trends that can be obtained for geomechanical properties.

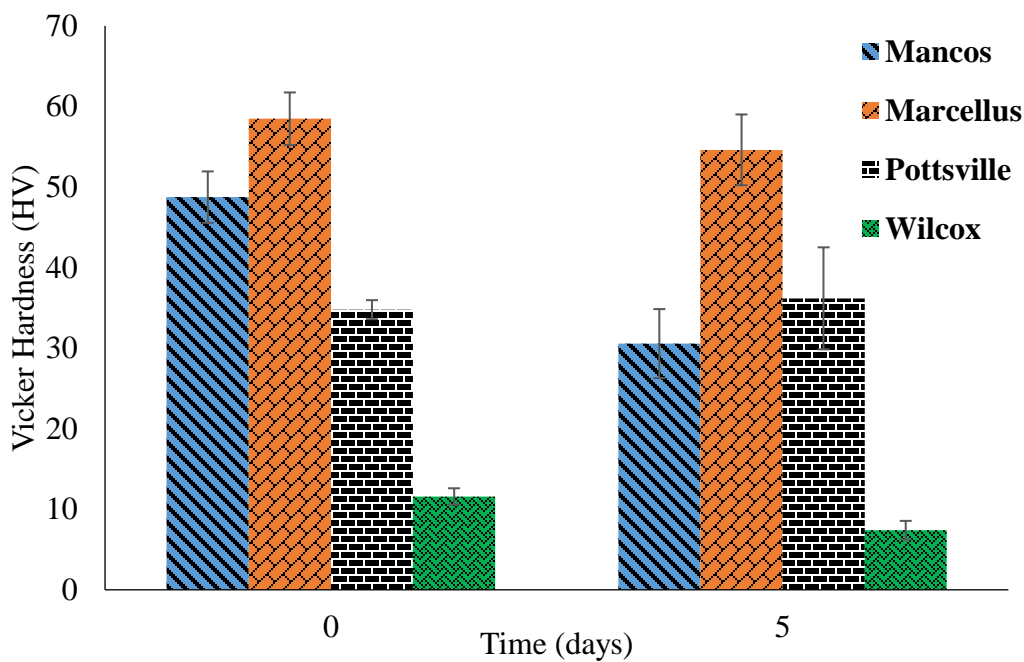


Figure 4.37: **the Vickers' micro-hardness** measurement taken on multiple samples of the experimental shale rocks. The results indicated a mild reduction in geomechanical hardness of the rock samples which are most significant in the Mancos, Marcellus and Wilcox shale rocks with lower quartz contents. This implies that initial quartz composition of shaly caprocks might be important in maintaining geomechanical integrity in long term CO₂ sequestration.

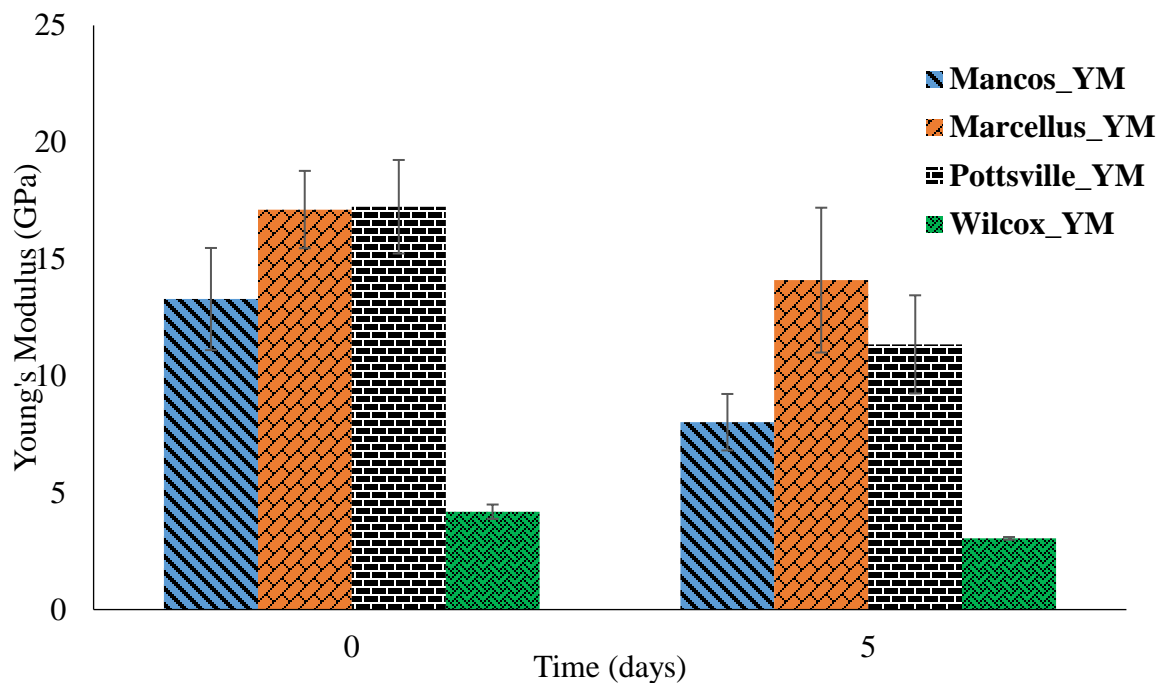


Figure 4.38: **Young's Modulus (GPa)** plots showing across the board decreases in measured values for the shale caprocks after flooding with CO₂-brine at 50°C and 1000psi.

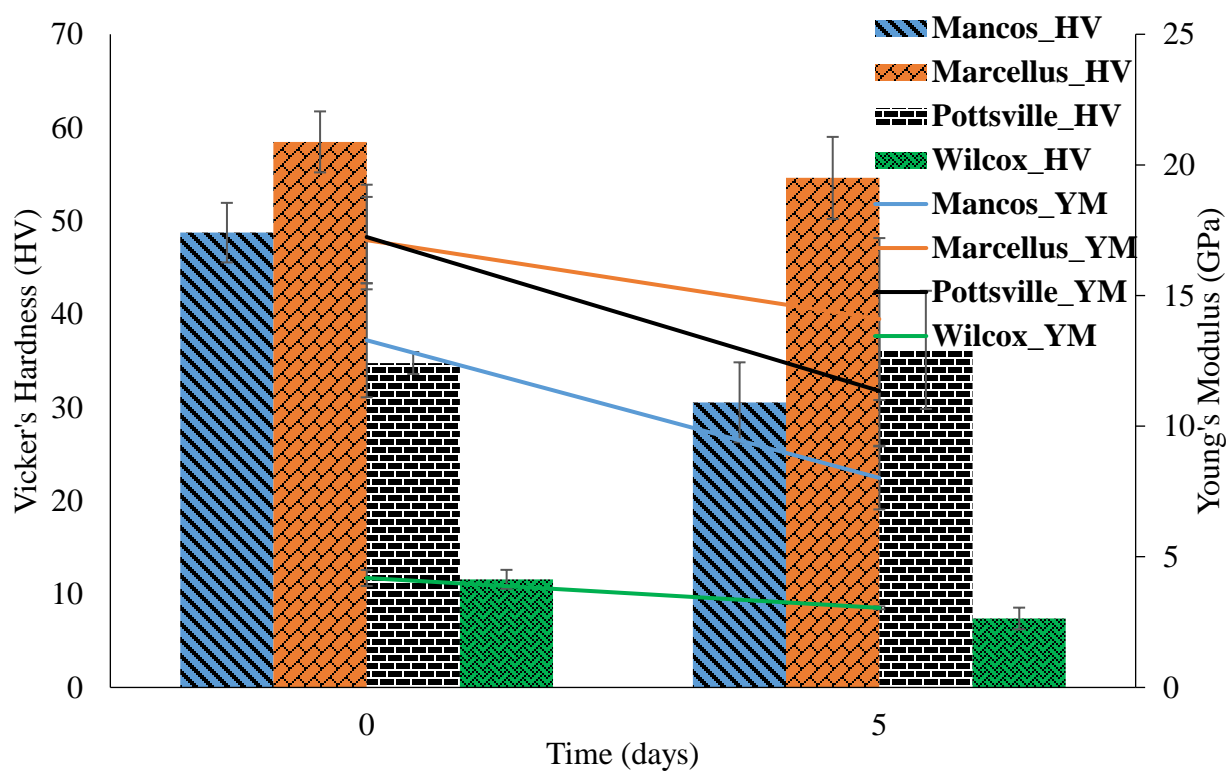


Figure 4.39: **Combined Hardness and Young's Modulus** plots showing across the board decreases in measured values for the shale caprocks after flooding with CO₂-brine at 50°C and 1000psi.

Figure 4.40 shows a plot of magnitude change in Vickers' hardness versus changes in the mineralogical composition of the shale rocks with respect to quartz, clay and carbonates. It can be suggested that formation of diagenetic quartz could improve the hardness of the shale rock as observed in the Pottsville shale where the percentage change in quartz content exceeded 10% which likely resulted from the clay fractions that were reduced by almost 15%. Significant reduction in clay and carbonates fraction of the shale rock which did not necessarily transformed to diagenetic quartz, as observed in the Mancos, Marcellus and Wilcox shale rocks, could shrink the geomechanical hardness of the rock. Higher temperature and pressure experiment could be used to confirm this observation.

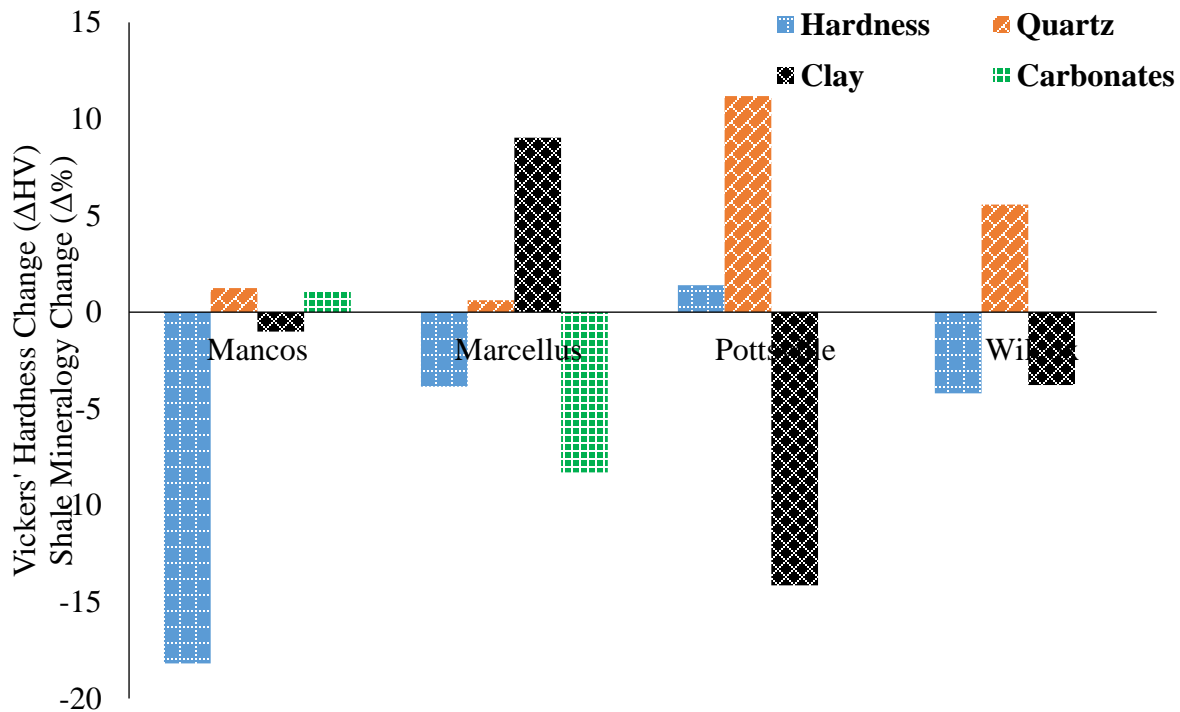


Figure 4.40: A correlation between the hardness of the shale rock and quantifiable mineralogical change in percentages. The graph shows that formation of diagenetic quartz can improve the hardness of the shale rock as observed in **Pottsville shale**. Significant reduction in clay and carbonates fraction of the shale rock, as observed in the **Mancos, Marcellus and Wilcox shale rocks**, can shrink the geomechanical hardness of the rock.

4.7 Differential Pressure Analysis

Differential pressure drop data acquired during the experimental runs were analyzed for flow inferences and diagnostics. Each shale caprock type had associated experimental runs that acquired multiple differential pressure data over a 5-day period. For example, three experimental runs were performed on the Mancos shale using composite fractured cores (**25 μ m and 150 μ m micro-tubing embedded**) with reaction effluent flowing through. This yielded thousands of differential pressure data points at 20 secs interval that were averaged for diagnostic and flow characteristic trends. These experimental runs were the same for other shale caprock types. These flow experiments were repeated for composite fractured cores with 150 μ m micro-tubing embedded for all the shale caprock types. The results of the averaged differential pressure data (dP), the 1st derivative of the differential pressure (dP/dt) and the estimated fracture conductivity are presented in figures 4.41 to 4.46. A comparison of the two fracture conductivity profiles are presented in figure 4.47. The effective fracture width was first estimated which formed a major input for the calculation of dimensionless fracture conductivity. The differential pressure drop, dP, data acquired during the experiment are presented in figures 4.41 (**for 25 μ m micro-tubing embedded cores**) and 4.42 (**for 150 μ m micro-tubing embedded cores**).these are averaged data points of pressure measurement acquired per every 20 seconds.

Figures 4.43 and 4.44 show the 1st order derivative of the differential pressure data for all the samples used in the experiment involving 25 μ m and 150 μ m micro-tubing embedded cores respectively. The results showed a gradual increase in the differential pressure (dP) drop across the composite core as dissolved precipitates laden fluid in flowed through it under equivalent temperature and pressure conditions prevailing in the whole closed system. These dP

measurements were acquired to tract the possibility of micro-fracture occlusion as a result of intra-fracture path precipitation. The differential pressure drop profiles (figures 4.41 and 4.42) showed significant increases within the initial two days of the experiment which gradually stabilized in the last three days. It will be noted that the stabilized value (or peak) of the pressure drops for the 150 μ m fractured cores profile (figure 4.42) is about half of the stabilized peak for 25 μ m composite fractured cores (figure 4.41). These profiles are indicative of possible particulate build up along conductive flow paths in the fractured composite cores.

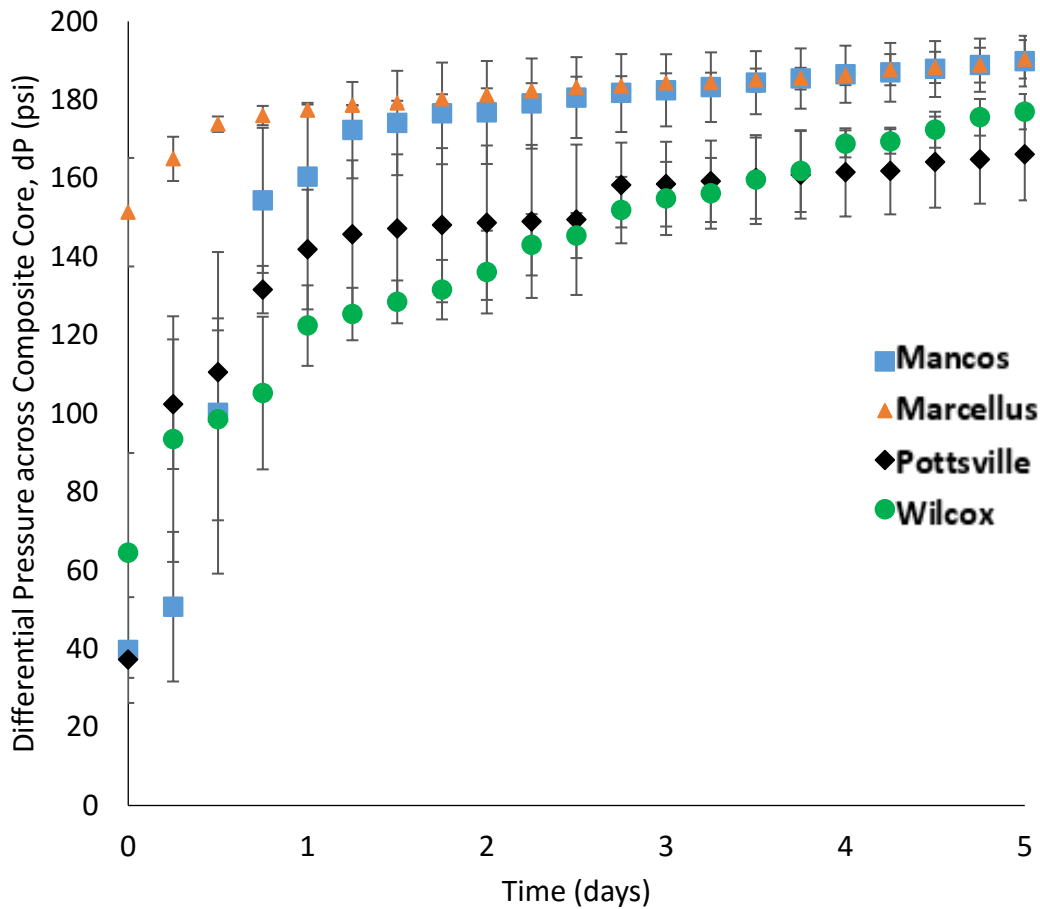


Figure 4.41: Average differential pressure profile across the **25 μ m composite core**, with embedded micro-tubings to mimic fractures. The injected fluid was directly from the outlet of the packed bed of crushed shale rock samples. Each data point represented a moving average from the three experimental runs per shale rock samples.

The first derivative of dP data as shown in figure 4.43 reveals that the most significant change to pressurized flow occurred in the first two days of starting the experiment for all the shale rock samples considered. The large fracture cores have similar behavior as expected (figure 4.44). It can be inferred that the impact of reactive flow on micro-fracture conductivity under carbon sequestration conditions will be most significant in the short term with the effect tapering off over the long term. The impact of high temperature and pressure conditions need to be investigated in subsequent experiments. The pressure profiles and their 1st derivatives are important in capturing the onset of changes in fracture flow and behavior. The estimation of fracture conductivity provides a quantitative view of these changes.

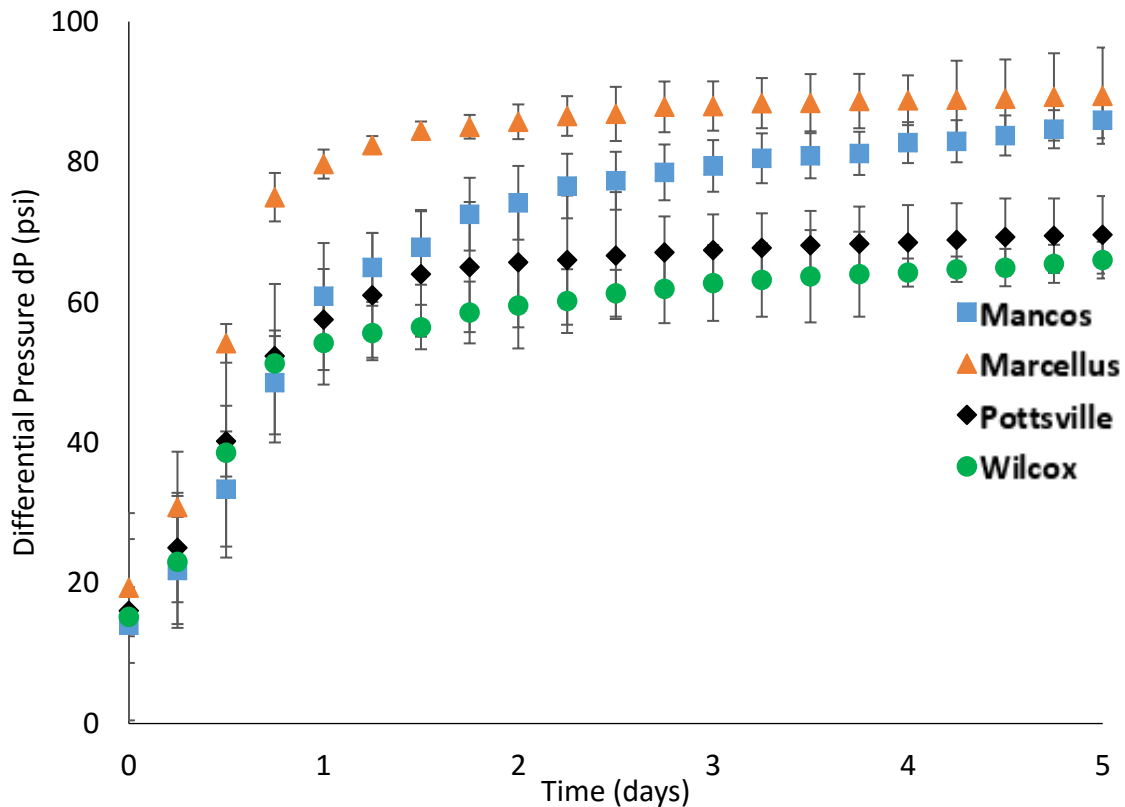


Figure 4.42: Average differential pressure profile across **150µm composite core**, with embedded micro-tubings to mimic fractures. The injected fluid was directly from the outlet of the packed bed of crushed shale rock samples. Each data point represented a moving average from the three experimental runs per shale rock samples.

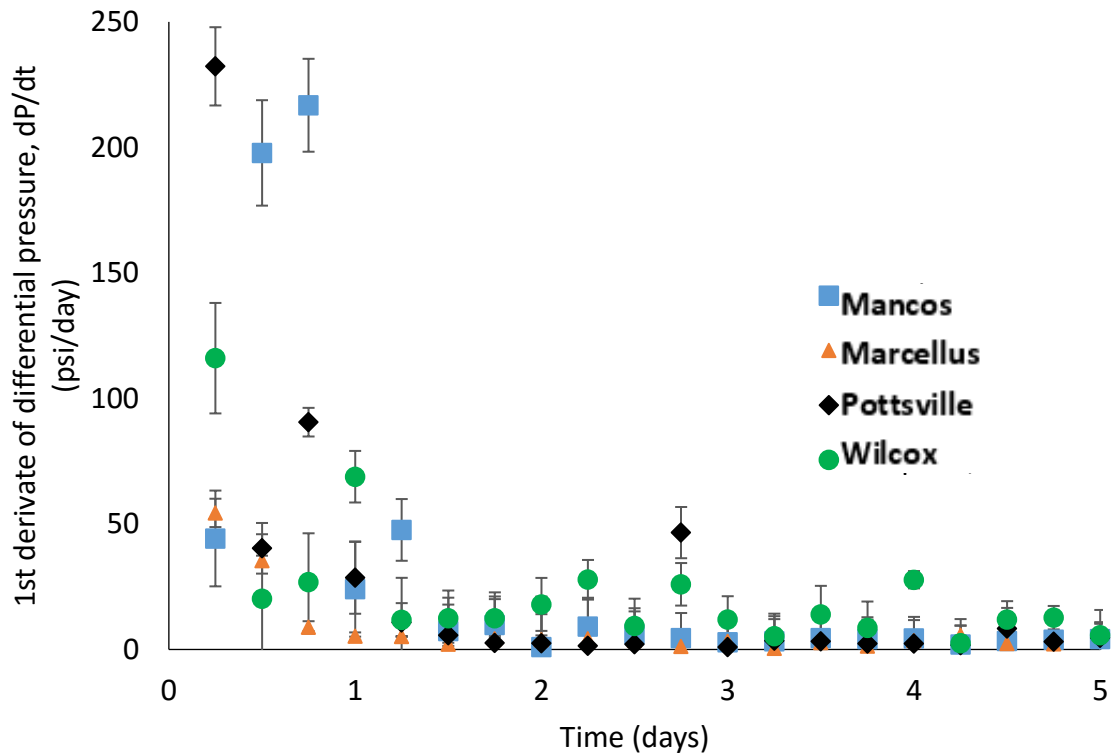


Figure 4.43: Average first derivative of differential pressure drop across the **25 μ m composite core**, with embedded micro-tubings to mimic fractures. The injected fluid was from directly from the outlet of the packed bed of crushed shale rock samples. The profile showed that most significant changes to pressurized flow behavior occurred within the first two days of the experiment. This probably due to flow path occlusion.

The use of pressure derivative is to help identify possible inflection points that could be diagnostic of the pressure responses. The acquisition of thousands of differential pressure data is useful in this regard. Laboratory transient pressure analysis provides a description of the fracture flow behavior though the length and geometry of the effect fracture in these experiments are several order of magnitude shorter than that obtained in the field. The observations from the pressure derivative presented in this report showed conclusively that day 2 of the experiments was the most significant for flow properties change.

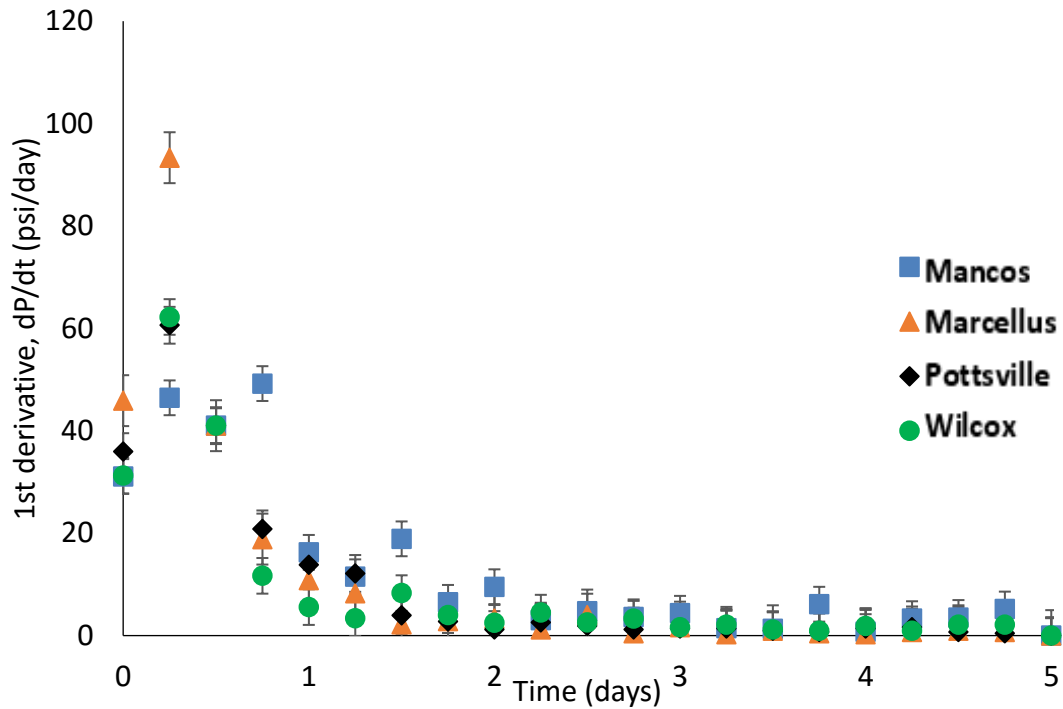


Figure 4.44: Average first derivative of differential pressure drop across the **150 μ m composite core**, with embedded micro-tubings to mimic fractures. The injected fluid was from directly from the outlet of the packed bed of crushed shale rock samples. The profile showed that most significant changes to pressurized flow behavior occurred within the first two days of the experiment. This probably due to flow path occlusion.

4.8 Fracture Conductivity Estimation

The fracture conductivity of the multiple composite fractured cores were estimated using the equations proposed by Dicman et al., [193, 221], and Warren and Root [222] for flow in fractures. Each shale caprock type had associated experimental runs that acquired multiple differential pressure data over a 5-day period. For example, three experimental runs were performed on the Mancos shale using composite fractured cores (25 μ m micro-tubing embedded) with reaction effluent flowing through. This yielded differential pressure data points at 20 secs interval that were averaged for diagnostic and flow characteristic trends. These experimental runs were the

same for other shale caprock types. These flow experiments were repeated for composite fractured cores with 150 μ m micro-tubing embedded for all the shale caprock types. The results of the estimated fracture conductivity are presented in figures 4.45 to 4.47. The effective fracture width was first estimated which formed a major input for the calculation of dimensionless fracture conductivity. The critical assumptions were i.) flow was primarily through fractures ii.) bulk fracture flow properties are captured in the experimental differential pressure measurements ii.) CO₂-brine viscosity was constant throughout the experiment iii.) the length of the core approximates the fracture length. Using equations 4.1 to 4.8;

$$k_f = 8.45 \times 10^9 w_f^2 \quad \text{Eq. 4.1}$$

$$k_f = \frac{k_{av}A - k_m(A - w_f l)}{w_f l} \quad \text{Eq. 4.2}$$

$$8.45 \times 10^9 w_f^3 l - k_{av}A + k_m(A - w_f l) = 0 \quad \text{Eq. 4.3}$$

$$q_m = \frac{k_m A \Delta P}{\mu L} \quad \text{Eq. 4.4}$$

$$q_f = 9.86 \times 10^9 \frac{w_f^3 l \Delta P}{12 \mu L_f} \quad \text{Eq. 4.5}$$

$$w_f k_f = \pi C_r k L_f \quad \text{Eq. 4.6}$$

$$w_f = \sqrt[3]{\frac{q_f \times 12 \mu}{9.86 \times 10^9 \Delta P}} \quad \text{Eq. 4.7}$$

$$C_r = \frac{w_f k_f}{\pi K_{av} L_f} \approx \frac{w_f}{\pi L_f} \quad \text{Eq. 4.8}$$

Where ΔP , w_f , l , L_f , k_m , k_f , k_{av} , A , q_m , q_f , μ , and C_r represent differential pressure (atm), fracture width (cm), core diameter (cm), fracture length (cm), matrix permeability (darcy), fracture permeability (darcy), average permeability (darcy), cross sectional area (cm²), flow rate through matrix (cm³/sec), flow rate through fracture (cm³/sec), viscosity (cp) and dimensionless fracture conductivity respectively.

Figure 4.45 shows the dimensionless fracture conductivity for flow through the artificially fractured composite cores (with 25 μ m micro-tubings embedded), calculated using equation 4.8. The profile suggests that the conductivity of the fractures degenerated rapidly within the first day of the experiment, tapering off at a constant rate towards the end of the experiment. The data presented in figure 4.45 were based on three experimental runs per shale rock sample with the error bar representing the standard deviation values. The fracture conductivity profile for the experiments that were conducted using fractured composite cores with 150 μ m micro-tubing embedded showed similar trend in rapid conductivity loss within the initial two days of the experiments (figure 4.46). With the recovery of significant amount of precipitates from effluent fluid, it can be inferred that in-situ geochemical precipitation was responsible for the loss of fractured conductivity as differential pressure drop across the cores built up and later stabilized during the experiments. It is estimated that only few micron size particulates are required to completely occlude fracture flow paths. It also appears there is no direct linear correlations between the fracture conductivity trends and the micro-tubings sizes that were used during the experiment. Chapters 5 and 6 explored the attempts at fitting the experimental data of the calculated fractured conductivity and reaction kinetics for some form of generalization.

Figure 4.47 compared the trends of the fracture conductivity of the 25 μ m cores with the 150 μ m cores. The extent of conductivity reduction is about 30% lower for the bigger micro-fractures (150 μ m). This indicates that there is significant limit to fracture aperture closure due to geochemical effects. The data presented in figure 4.47 can be used for modelling the impact of diagenetic alterations within subsets of naturally fractured shale caprocks. The availability of more geochemical data and their impacts on flow properties in micro-fractures will help build more robust numerical approximations that can be applied field-wide. The number of shale rock samples used in these experimental reports fall within and outside those that have been reported in the literature. The fact that the larger the potential micro-fracture defects in an intact rock the less likely short-term diagenesis can seal them, implies that we can only depend to a limited extent on the ability of rock-aqueous CO₂ interactions to heal inherent anomalies in caprocks. The field-wide effects of this can be investigated with discrete fracture network studies. In many instances, modeling flow characteristics in fractured media can be through the use of the dual-continuum algorithm whereby fractures and matrix are modeled as two separate kinds of continua. These facsimile type of models usually do not replicate many commonly observed types of fractured tight rock characteristics as they do not explicitly model the shape of discrete fractures, geological inclusion features, and characteristic beddings that govern flow direction in the subsurface. One of the perceived issues with using DFN models to address this short coming is that the fractures in the model tend to be too uniform in length, area and spatial distribution but these features describe the interpretative assumptions made in this experimental report.

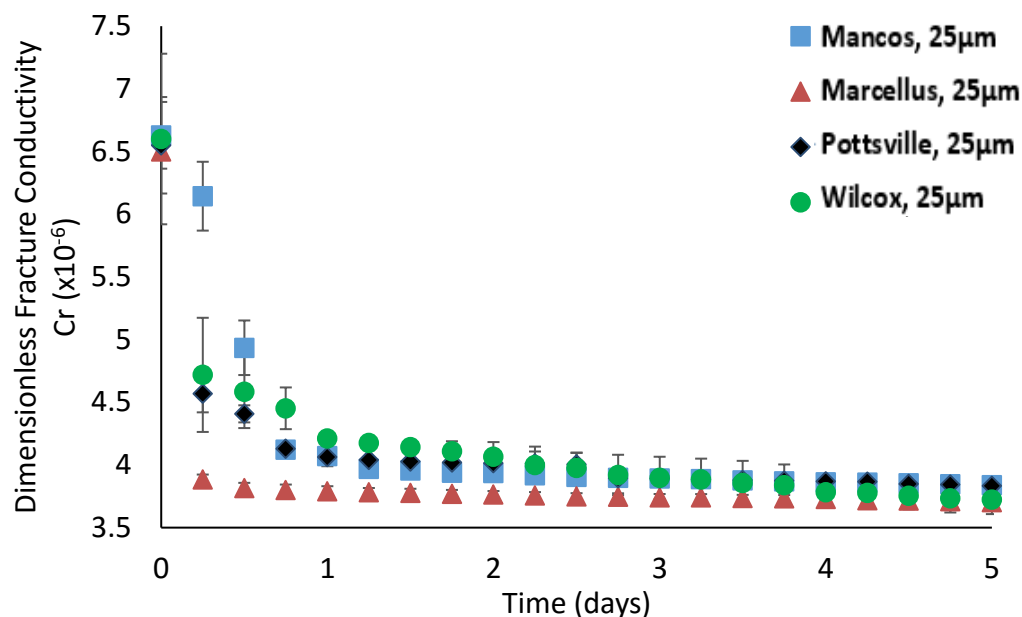


Figure 4.45: Calculated dimensionless fracture conductivity profile from experimental differential pressure (dP) data using fractured core parameters with **25µm micro-tubings embedded**. The profile indicated a rapid reduction in the conductivity of the artificial fractured core within the first two days of the experiment. This reduction can only be attributed to in-situ geochemical precipitation.

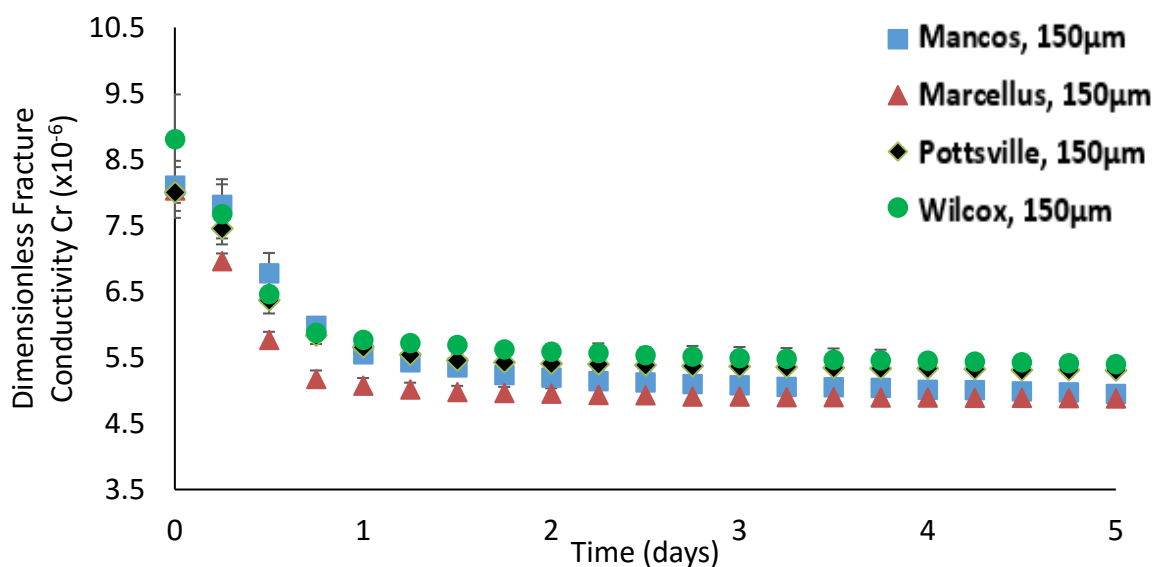


Figure 4.46: Calculated dimensionless fracture conductivity profile from experimental differential pressure (dP) data using fractured core parameters with **150µm micro-tubings embedded**. The profile indicated a rapid reduction in the conductivity of the artificial fractured core within the first two days of the experiment. This reduction can only be attributed to in-situ geochemical precipitation.

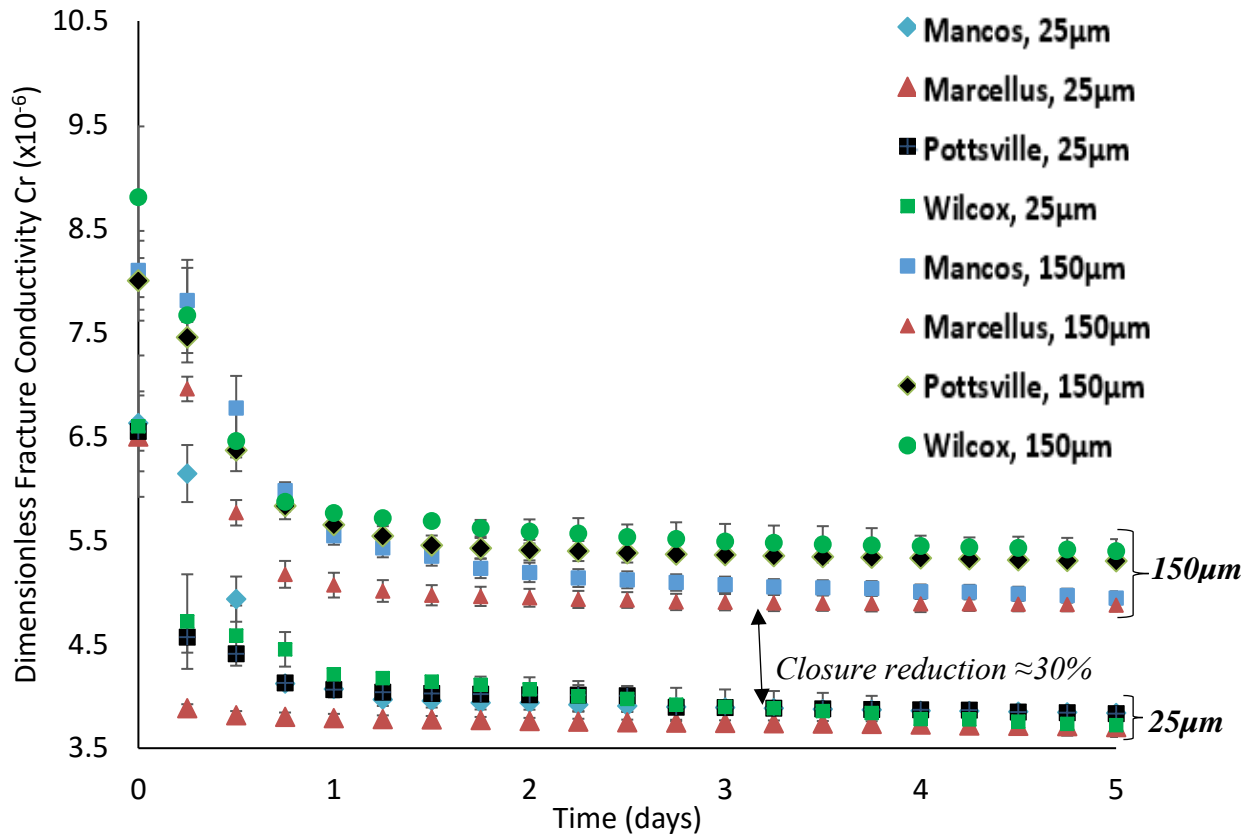


Figure 4.47: **Comparison** of calculated dimensionless fracture conductivity profile from experimental differential pressure (dP) data using fractured core parameters with **25µm and 150µm embedded micro-tubings**. The profile indicated a rapid reduction in the conductivity of the artificial fractured core within the first two days of the experiment. The extent of conductivity reduction is about 30% lower for the bigger micro-fractures (150µm). This indicates that there is significant limit to fracture aperture closure due to geochemical effects.

CHAPTER 5

DISCUSSION OF RESULTS OF SHALE ROCK/FLUID INTERACTIONS EXPERIMENTS

5.1 General Discussion of Experimental Results

The detailed discussion of experimental results is presented in this chapter. The discussion is done under three sub-headings; (1) geochemical speciation in effluent fluid, (2) bulk rock/precipitates analysis, (3) fracture flow characterization. The discussion covers in detail the aqueous geochemistry of the resulting dissolved-mineral-saturated fluid (after rock-fluid interactions experiments) and the impact of rock-fluid interactions on surface and bulk rock geochemistry, including the precipitates that were recovered from the effluent. The effect of the convective transport of the geochemically active effluent through fractured media is also discussed; primarily differential pressure drop and micro-fracture conductivity. The impact of these phenomena are captured by the various analytical methods and techniques that were used for fluid, rock and fractured media characterization.

5.1.1 Geochemical Speciation in Experimental Effluent Fluid

The geochemical characterization of the effluent fluid showed the most pronounced documentation of reactive rock-fluid interactions. The pH of the effluent fluid showed initial resilience to acidic fluid medium. The shaly rocks acted as alkaline buffering media where by the final effluent indicated geochemical reactions that brought acidity conditions up to and above neutral scale. It can be observed from the pH profile (figure 4.1) that the alkaline buffer strength of the shale rocks through reactive interaction with the CO₂-brine fluid at the experimental pressure and temperature conditions is significantly pronounced for the Mancos, Marcellus and Pottsville shale rocks while that of the Wilcox shale is markedly lower. Many geochemical

reactions are dependent on the pH of the medium. It is expected that forward dissolution reactions will be encouraged under acidic pH conditions of CO₂ geo-sequestration. These observations are in agreement with previous experiments conducted in the laboratory and reported by other researchers. The changes in pH is expected to control, to some degree, the ability of the various rock minerals to exchange ions with one another. The diffusion and subsequent dissolution of free CO₂ molecules in the connate water of the caprock is expected to lead to localized ultra-low pH ranges that will catalyze pore and micro-fracture surface dissolution. The idea that supercritical CO₂ would sink to the deep bottom part of the reservoir brings the idea of convective transport of super-saturated acidic fluid into the overlaying seal rocks. This will have the same effect as gaseous CO₂ diffusion in the tight hydraulically connected spaces within the rock. The pH data reported suggest varying degrees of alkaline buffering strength of the rocks; the higher the fraction of calcium based minerals, the higher the alkaline buffering strength. This is consistent with literature reports.

The ICP-OES concentrations of both major and trace metals such as Ca²⁺, Mg²⁺, Se²⁺, Al³⁺ Si²⁺, and Zn²⁺ indicated rapid dissolution of rock minerals that have alkaline earth metals in their crystalline or amorphous matrices (figures 4.2 to 4.15). The concentration profile for Calcium shows that the Marcellus samples had the highest fraction in solution which rapidly decreased over the five day period of continuously flooding the samples with CO₂ saturated brine. The initial pH of the influent fluid is approximately 3.7. The Mancos, Marcellus and Wilcox shale rocks exhibited similarly trend of a gradual exponential decline over the five day period. The Pottsville shales reflected a gradual increase that appears to continue over the experimental period. While the elemental concentration of Calcium in the Mancos, Marcellus and Wilcox shales peaks on the

first day of the experiment, that of the Pottsville shale continued to increase over the five day period but it also expected to peak and gradually decline with similar trend to the Mancos, Marcellus and Wilcox shales. This resilient behavior of the Pottsville shale might suggest a slower dissolution reaction of its calcium based minerals constituent compared to the Mancos, Marcellus and Wilcox shales. The bulk rock XRD analysis indicated calcite and dolomite as the main calcium bearing minerals in the Mancos, Marcellus and Wilcox shales while anhydrites are the main calcium bearing minerals in the Pottsville. These observations in the effluent are significant as the cationic content of any fluid determines the extent to which sizeable amount of dissolved solutes precipitates out of solution. This is evident in the Marcellus and Mancos samples where large amount of carbonate precipitates were recovered. The precipitation of dissolved minerals at normal temperature and pressure conditions shows that in the subsurface, changes in geochemical and thermodynamic conditions can affect the speed at which aqueous precipitation processes take place.

5.1.2 Bulk Rock/Precipitates Analysis

The XRD analysis of the bulk rocks yielded useful information about the possible changes in the mineralogy of the shales. Figures 4.17 to 4.20 show the profiles of the main mineralogical components in the shale rocks (pre- and post-flooding with CO₂-brine) and the recovered precipitates as identified by bulk XRD analysis for the Mancos, Marcellus, Pottsville and Wilcox shale rocks respectively. Bulk XRD analysis reflected changes that are not significant enough in their percentages in order to make affirmative conclusions. The clay XRD analysis also showed that there are only subtle changes in the clay component of all the rock samples. But the

Marcellus shale showed far greater heterogeneity in both mineralogy and morphology. These heterogeneities does not make the Marcellus shale a good candidate for seal rocks of CO₂ sequestration sites. The Pottsville shale shows platy grain structures that are tightly packed and efficient for preventing fluid movement. In terms of pre- and post-flooding mineralogy, it appears the Pottsville shale is most stable followed by the Wilcox which is not tight in pore structure. Furthermore, the recovery of amorphous precipitates in all of the associated effluent samples showed the role that temperature plays in the ability of dissolved minerals to remain in solution for an extended period. More than ninety percent of the precipitates were recovered within a month after the experiments. These precipitates are of varying coloration; dark brown to light pink (see Appendix A). While the bulk shale rock samples showed little changes at the surface, the mineralogical analysis carried out on them revealed the removal of amorphous contents from the rocks in significant amounts. These amorphous contents form the bulk of the precipitates were recovered from the effluent. Amorphous content of rocks are usually responsible for suppressed peaks in XRD qualitative analysis. The bulk XRD analysis of precipitates showed the appearance of diagenetic minerals that were formed from the major mineralogical components of the shale rocks. The quantitative XRD analysis performed on samples are largely qualitative with minor evidence of changes in the mineralogy of the rock samples after the experiment. But for the margin of changes reported in tables 4.1 and 4.2, it best to assume that the contents of the precipitates are largely amorphous and crystalline forms of carbonates as seen in XRD.

The total carbon content of the shale rocks (figure 4.16) indicated that the higher the organic content of the seal rock, the higher the potential for carbon absorption to the surface of the rock. The Marcellus shale exemplified this behavior well when compared to other shale samples. The

percentage carbon content were in the order Marcellus > Wilcox > Mancos > Pottsville. This order of magnitude still holds after the CO₂-brine flooding experiment. It can be observed for the figure that were significant increases in the percentage content of carbon in all the samples which can be indicative of both adhered carbon and mineralized carbon in the these shale samples.

The electron microprobe analysis (EMPA) showed the presence of Iron (Fe), Sodium (Na), Potassium (K), Silicon (Si), Carbon (C), Oxygen (O), Chlorine (Cl), Manganese (Mn), Calcium (Ca), Magnesium (Mg) and Aluminum (Al). They are present in rock minerals capable of exchanging ions with carbonic acid or aqueous CO₂. The elemental distribution of Ca and Mg in the reacted Mancos and Marcellus shales were lower within grain facies as shown in figures 4.25 to 4.27 and figures 4.28 to 4.30 (top row) respectively when compared to the corresponding control samples (bottom row). These were the surface maps for elemental spread involving CO₂-brine flooded samples. It has been noted that in addition to common alkali earth metals such as Na and K that form compounds which are generally soluble in acidic or alkaline fluids, Ca and Mg solutes have significant ion-exchange capacity as well. The surface depletion within grains show the extent of the reach of aqueous CO₂ in supporting dissolutive rock-fluid interaction in the subsurface. Pottsville and Wilcox shales are lean in Ca and Mg based minerals which informed the limited traces of these elements on the surface of the thin section samples. The distribution of Al and Fe as shown in figures 4.26/27 and figures 4.29/30 for Mancos and Marcellus shales respectively indicated low activity in the reacted samples while figures 4.31 to 4.33 and figures 4.34 to 4.36 for Pottsville and Wilcox shales respectively reflected significant concentration of Al and Fe which have smaller percentages in the minerals baring them. These imply that compounds of Ca, Mg, Al, and Fe which were identified in the shale caprock samples, either as major or trace minerals,

would be reactively soluble with faster kinetics in aqueous CO₂ with the possibility of re-precipitation to form new minerals at subsurface pressure and temperature. The formation of Aragonite in experiments involving Marcellus shale exemplify the dissolution-precipitation processes that impact long term caprock integrity.

The magnitude of the mechanical strength of the bulk shale rocks was reduced for most of the samples analyzed (figures 4.37 and 4.38). This was measured in terms of Vickers' Hardness. The most impacted was the Wilcox shale which has the highest percentage of swelling clay (Montmorillonite). The tablet of shale rocks used were polished using laboratory grinder which could have altered some mechanical properties. These polishers are graded from fine to coarse applications. The finest grade of polisher is used at the final stage of rock preparation for micro-indentation. This is expected to have some effects on near-wellbore stability of shale caprock sections for CO₂ sequestration sites. Also, the correlation of changes in mineralogy to hardness and Young's Modulus (figures 4.39 and 4.40) suggested that the higher the diagenetic quartz formed, the higher the mechanical properties. It implies that rock-fluid geochemical interactions that can continuously convert clays and other minerals into opal will provide higher geomechanical stability and tighter hydraulic barrier on the longer term.

5.1.3 Fracture Flow Characterization

The characterization of fracture flow properties showed that the formation of precipitates in the super-saturated fluid can occlude hydraulic conductivity. This phenomenon is supported by the experimental data presented in figures 4.41 to 4.47. These are in specific cases when soluble alkaline earth metal minerals are present in large amount with the host rock as seen with

carbonates rich shale rocks. The next chapter attempts to integrate the geochemical and fracture flow experimental data obtained and provide models to represent them. The applications of such integrated models will be in numerical reservoir simulations where discrete fracture network models can be used to describe and visualize long term behavior of sedimentary tight rocks under carbon sequestration conditions. It is expected that deep fractured shale will exhibit greater diagenesis when in contact with aqueous carbon dioxide. The experimental data reported showed that 25 μ m sized fractures can be closed more rapidly with 150 μ m sized ones taking longer time to close and are 30% less in fracture sizes. The first derivatives of the differential pressures showed that most of the changes occurred during the first two days of the experiment with the Marcellus sample reflecting the most changes in the rapid exponential decline. The use of pressure derivative is to help identify possible inflection points that could be diagnostic of the pressure responses. The acquisition of thousands of differential pressure data is useful in this regard. Laboratory transient pressure analysis provides a description of the fracture flow behavior though the length and geometry of the effect fracture in these experiments are several order of magnitude shorter than that obtained in the field the Mancos and the Wilcox also indicated a rapid loss of fracture conductivity. These losses are attributable to the generation of significant amount of precipitates from the effluent fluid of shale rock-aqueous CO₂ interactions. These precipitates were crystalized at varying rates and this was thought to have been responsible for the different initial gradients. The rapid precipitation of aragonites from the effluent samples of the CO₂-brine flooding Marcellus shales showed that the convective transport of precipitate laden fluid at 50°C and 1000psi pressure, can lead to fast fracture conductivity closure.

5.2 Integrated Experimental Observations

The integration of the sections described above leads to the flow diagram shown in figure 5.1. The geochemical footprint in the effluent and the mineralogical/morphological characteristics of the shale rocks is shown to have impacted the conductivity of micro-fractures. This is through the formation of precipitates. The physics of geochemical-fracture flow in shale caprock can be described analytically. The upper decline curve represents lower impact of the effects of geochemical interactions under constant geomechanical conditions. The upper decline curve represent higher impact of the effects of geochemical interactions. These effects can be mathematically/analytically modelled as an exponential-natural logarithmic function. This function can be used in used in complex discrete fracture networks representing natural flow path deformities in shale caprock. This function is exclusively for corrections to flow characteristics over time in re-activated or open micro-fracture networks inherent in shale caprocks. The monitoring of leakages via caprock should account for geochemical changes and not just geomechanical alterations which tend to first worsen seal integrity during the initial phase of injection. The independent modelling of coupled geochemical effects and micro-fracture conductivity can be described by the exponential-natural logarithm relationship, leaving out complex reactions which are difficult to account for simultaneously. In the literature, the effect of capillarity is highly emphasized as a determining factor for seal integrity but the presence of scattered, randomly distributed micro-fractures lead to low or non-accounting of carbon molecules that could be involved in rock-fluid interactions under CO₂ sequestration and containment conditions.

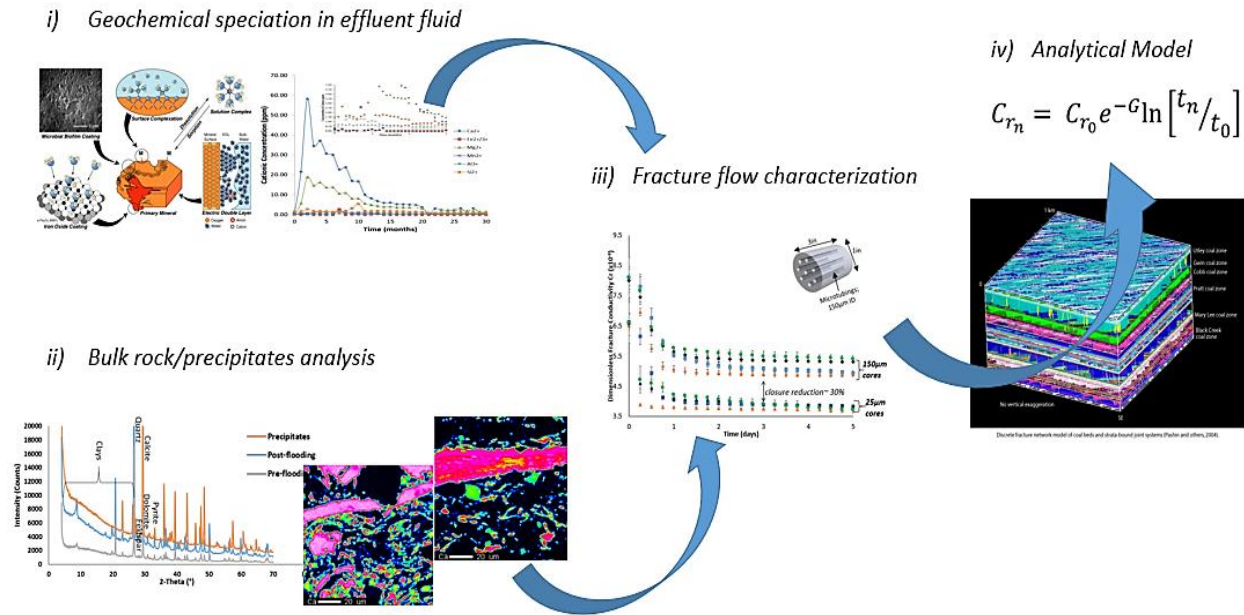


Figure 5.1. The integration of the geochemical, geomechanical and micro-fracture conductivity in shale rock-aqueous CO₂ interactions. The schematics showed how convective fluid transport will provide the necessary flow-path bridging materials after repetitive dissolution-precipitation reactions. These reactions provide significant quantities of precipitates for flow occlusion.

The use of analytical solutions in discrete fracture network models will improve the process of carbon account in CO₂ sequestration projects by ensuring that mineralized carbon molecules are accounted for in flow-path closure. Multiple layers of unevenly distributed tight rocks can reveal heterogeneous behavior via pressure and saturation field monitoring. Comparison with field data/simulation will be tremendously useful for carbon sequestration site characterization.

CHAPTER 6

CONCLUSIONS AND RECOMMENDATIONS

6.1 Conclusions

The interaction of aqueous CO₂ and shale caprocks that are representative of the geological seals suitable for CO₂ sequestration and containment projects have been experimentally studied under laboratory conditions of stress (1400psi axial and radial stress), temperature (50°C) and injection pressures (1000 psi). Four shale caprock samples from different geologic formations within the United States were used. The effluent emanating from these closed system diagenetic rock-fluid interactions were flowed through an artificially fractured media made of cylindrical cement cores with PEEK polymer micro-tubings embedded. This was intended to mimic micro-fractures, which are sometimes present in intact caprocks. Several experimental runs using the unique setup described in Chapter 3 were carried out with two different sets of micro-tubing diameters (25µm and 150 µm ID). Effluent fluid analysis were carried out using pH meters and ICP-OES techniques for acidity/alkalinity measurements and ionic content analysis. Bulk shale rocks were analyzed with XRD, SEM, EMPA, TOC and Micro-indentation techniques for changes in rock mineralogy, morphology, elemental composition, inorganic carbon and geomechanical properties. The measurement of differential pressure drop across the artificially fractured cores yielded information on the impact of geochemical changes in the experimental fluid on effective micro-fracture apertures and corresponding fracture conductivity.

The following major conclusions can be inferred from the laboratory experiment involving shale rock interactions with CO₂ saturated brine under dynamic flow conditions:

1. Moderately high temperature (50°C) and injection pressure (1000psi) in the core scale experiment indicate rapid dissolution of shale rock minerals as shown by the analyses of effluent fluid, bulk rock and precipitate analyses.
2. The effluent fluid indicated that alkaline earth metal based minerals particularly Calcium and Magnesium in shale caprocks are the most susceptible to reactive dissolution at these experimental conditions.
3. Reactive dissolution leads to the formation of new diagenetic minerals, notably in carbonates-rich shale caprocks, which precipitated out of the effluent fluid in significant quantity. These precipitates are capable of aggregating in saturated solutions.
4. The distribution of major elements on the surface of the bulk shale caprocks showed minute morphological changes at the edges of distinct grains and the association of minor elements with major minerals. This shows that significant heterogeneity within the tight rocks are responsible for the release of environmentally unfriendly trace elements that can compromise groundwater quality.
5. Reaction kinetic models indicated that there is significant increase in rates of diagenetic rock fluid interactions as temperature is additively doubled. This implied that deep hot shale rocks will experience higher rates of diagenetic rock-fluid interactions that could possibly impact hydraulic fractures. This is applicable to large scale CO₂ sequestration into stimulated shale reservoirs with hydraulic fracture networks.
6. Micro-hardness property of the bulk rock showed significant reduction in geomechanical strength for three samples; Mancos, Marcellus and Wilcox. Micro-hardness property of

the bulk rock is not significantly affected as observed in this 5-day experiment for Pottsville shale samples with non-swelling clay and no carbonates.

7. The gradual rise of differential pressure drop across the fractured composite core is an indication of loss of flow characteristics. Dimensionless fracture conductivity indicated that the loss of flow characteristics was most pronounced within the first two days of the experiment leading to aperture closure over time.
8. There is significant limit to the size of effective fracture apertures that can be closed by diagenetic rock-fluid interactions. Experimental data showed approximately 30% reduction in end-of-experiment conductivity loss when micro-tubings sizes were changed from 25 μm to 150 μm .
9. The loss of fracture conductivity can be analytically modelled as an exponential-natural logarithm function for two profiles of fracture conductivity that represent the extremes.
10. The modelling of discrete fracture networks in shale caprocks can be the key to the accuracy of carbon accounting. It can be opined that given the potential of rock-fluid interactions in generating significant amount of precipitates, the exact amount of carbon from molecules of carbon dioxide injected and minerally sequestered can be estimated.
11. The data presented in this report can be used in incorporating the effect of short term diagenesis on fracture flow characteristics by assigning physics based models (exponential-natural logarithm function is developed) to discrete fracture network cases. The integration of various models of geochemistry, geomechanics and micro-fracture conductivity can provide a single model representation of caprock behavior/integrity under carbon sequestration conditions.

6.2 Recommendations

The understanding of diagenetic rock-fluid interactions in tight shale caprocks require detailed experimental data for successful theoretical and numerical modelling. Base on the additions to the body of knowledge through this research works, the following recommendations are proposed:

1. Experimental runs at higher temperature and pressure conditions could be carried out to investigate rock-fluid interactions effect in the case of injection of CO₂ into deep fractured shale formations. For example the experimental conditions could be: Overburden stress = 4000psi, Backpressure = 3600psi; Injection pressure = 3600 psi, Operating temperature = 150°C. Temperature and pressure control will present the biggest challenge and more sophisticated instrumentation can be deplored to achieve the desired conditions.
2. Acquire geochemical, geomechanical and flow parameters as were in the moderate temperature and pressure experiments described in this report. Imaging analyses of relevant samples will also be carried out to identify morphological changes.
3. Model the reaction rate and flow characteristics at multiple experimental conditions of pressure and temperature at the core scale for possible scale up to numerical simulation.
4. Predict subsurface implication of the impact of diagenesis and stress on fracture conductivity from core scale experiment and the associated models.
5. Additional shale rock samples could be explored to create a more robust statistically useful data base for geostatistical and discrete fracture network predictions of long term rock-fluid interaction effects on other geological basins of interests to CO₂ sequestration project managers.

REFERENCES

1. Shukla, R., et al., A Review of Studies on CO₂ Sequestration and Caprock Integrity. *Fuel*, 2010. 89(10): p. 2651-2664.
2. Stevens, S.H., Natural CO₂ Fields as Analogs for Geologic CO₂ Storage. 2005. Volume 2(Carbon Dioxide Capture for Storage in Deep Geologic Formations – Results from the CO₂ Capture Project Geologic Storage of Carbon Dioxide with Monitoring and Verification, Sally M. Benson, Lawrence Berkeley Laboratory, Berkeley, CA, USA): p. Pages 687-697.
3. Wollenweber, J., et al., Experimental Investigation of the CO₂ Sealing Efficiency of Caprocks. *International Journal of Greenhouse Gas Control*, 2010. 4(2): p. 231-241.
4. Bicocchi, G., et al., Chemical Alteration and Mineral Growth under High Pco₂ Conditions: Insights from the Mineral Chemistry of Carbonate Phases in the Caprese Reservoir (Northern Apennines, central Italy). *Chemical Geology*, 2017. 450: p. 81-95.
5. Arts, R.C., O. Eiken, and N. Scott- Sylvain, Ten Years' Experience of Monitoring CO₂ Injection in the Utsira Sand at Sleipner, Offshore Norway. *First Break*, 2008. 26: p. 65-72.
6. Akervoll, I., E. Lindeberg, and A. Lackner, Feasibility of Reproduction of Stored CO₂ from the Utsira Formation at the Sleipner Gas Field. *Energy Procedia*, 2009. 1(1): p. 2557-2564.
7. Buttinelli, M., et al., the Geo-database of Caprock Quality and Deep Saline Aquifers Distribution for Geological Storage of CO₂ in Italy. *Energy*, 2011. 36(5): p. 2968-2983.
8. Chadwick, R.A., et al., Geological Characterization of CO₂ Storage Sites: Lessons from Sleipner, Northern North Sea, in *Greenhouse Gas Control Technologies - 6th International Conference*, J. Gale and Y. Kaya, Editors. 2003, Pergamon: Oxford. p. 321-326.
9. Davis, E.J. and S.D. Marsic, Interpretation of CO₂-Sequestration-Induced Surface Deformation at Krechba, Algeria, in *SPE International Conference on CO₂ Capture, Storage, and Utilization*. 2010: New Orleans, Louisiana, USA. doi:10.2118/147444-MS.
10. Farokhpour, R., et al., Experimental and Numerical Simulation of CO₂ Injection Into Upper-Triassic Sandstones in Svalbard, Norway, in *SPE International Conference on CO₂ Capture, Storage, and Utilization*. 2010: New Orleans, Louisiana, USA.

11. Giday-WoldeGabriel, M.F., et al., Textural and Geochemical Features along a Reservoir-Cap Rock Contact in the Sacroc Unit of West Texas, L.A.N.L. Earth and Environmental Sciences Division, Editor. 2007: Los Alamos, NM, 87545 USA.
12. Xu, T., et al., Reactive Transport Modeling to Study Changes in Water Chemistry Induced By CO₂ Injection at the Frio-I Brine Pilot. *Chemical Geology*, 2010. 271(3-4): p. 153-164.
13. Zhang, W., et al., Long-Term Variations of CO₂ Trapped in different Mechanisms in Deep Saline Formations: A Case Study of the Songliao Basin, China. *International Journal of Greenhouse Gas Control*, 2009. 3(2): p. 161-180.
14. Carbon Sequestration Atlas of the United States and Canada. National Energy Technology Laboratory, Department of Energy 2010. Vol. 3: p. 162.
15. Ellis, B., et al. Alteration of Caprock Fracture Geometries During Flow of CO₂-acidified Brine: Informing Basin-scale Leakage Models From Pore-scale modeling and Core-scale Experiments. in AGU Fall Meeting Abstracts. 2011.
16. Javadpour, F., CO₂ Injection in Geological Formations: Determining Macroscale Coefficients From Pore Scale Processes. *Transport in Porous Media*, 2009. 79(1): p. 87-105.
17. Renard, S., et al., Geochemical Study of the Reactivity of a Carbonate r=Rock in a Geological Storage of CO₂: Implications of co-injected Gases. *Energy Procedia*, 2011. 4: p. 5364-5369.
18. Salem, A.M. and S.A. Sheded, Variation of Petrophysical Properties due to Carbon Dioxide (CO₂) Storage in Carbonate Reservoirs. *Journal of Petroleum and Gas*, 2013. 4(4): p. 91-102.
19. Wei, N., et al., Geochemical Impact of Aquifer Storage for Impure CO₂ containing O₂ and N₂: Tongliao field experiment. *Applied Energy*, 2015. 145: p. 198-210.
20. Bourg, I.C., L.E. Beckingham, and D.J. DePaolo, the Nanoscale Basis of CO₂ Trapping for Geologic Storage. *Environmental science & technology*, 2015.
21. Hong, K.C. and J.W. Ault, Effects of Noncondensable Gas Injection on Oil Recovery by Steamflooding. *SPE Journal of Petroleum Technology*, 1984. 36(12): p. 2160-2170.
22. Bagci, A.S. and F. Gumrah, Effects of CO₂ and CH₄ Addition to Steam on Recovery of West Kozluca Heavy Oil, in SPE International thermal Operations and Heavy Oil Symposium and Western Regional Meeting. 2004, Society of Petroleum Engineers: Bakersfield, California.

23. Smith, S.A., et al., Geomechanical Testing and Modeling of Reservoir and Cap Rock Integrity in an Acid Gas EOR/Sequestration Project, Zama, Alberta, Canada. *Energy Procedia*, 2009. 1(1): p. 2169-2176.
24. Mohammad, S., R.L. Robinson, and K. Gasem, Multiphase Analysis for CO₂: Water/Mixed-Gas Adsorption on Coals, in *SPE International Conference on CO₂ Capture, Storage, and Utilization*. 2010: New Orleans, Louisiana, USA.
25. Pitman, J.K., et al., Origin of Minerals in Joint and Cleat Systems of the Pottsville Formation, Black Warrior Basin, Alabama: Implications for Coalbed Methane Generation and Production. *AAPG Bulletin*, 2003. 87(5): p. 713-731.
26. Pashin, J.C., et al., Carbon Sequestration and Enhanced Recovery Potential of Mature Coalbed Methane Reservoirs in the Black Warrior Basin. *AAPG Special Volume*, 2009.
27. Goodman, A., et al., Methodology for Assessing CO₂ Storage Potential of Organic-Rich Shale Formations. *Energy Procedia*, 2014. 63: p. 5178-5184.
28. Murphy, R., et al., Ferrihydrite Phase Transformation in the Presence of Aqueous Sulfide and Supercritical CO₂. *Chemical Geology*, 2010. 271(1-2): p. 26-30.
29. Alemu, B.L., et al., Caprock Interaction with CO₂: A Laboratory Study of reactivity of shale with supercritical CO₂ and brine. *Applied Geochemistry*, 2011. 26(12): p. 1975-1989.
30. Pentland, C.H., et al., Measurement of Supercritical Carbon Dioxide Capillary Trapping in Core Analysis, in *SPE International Conference on CO₂ Capture, Storage, and Utilization*. 2010: New Orleans, Louisiana, USA. doi:10.2118/138476-MS.
31. Hemme, C. and W. van Berk, Change in Cap Rock Porosity triggered by Pressure and Temperature Dependent CO₂–Water–Rock Interactions in CO₂ Storage Systems. *Petroleum*, 2017. 3(1): p. 96-108.
32. Michels, L., et al., Intercalation and Retention of Carbon Dioxide in a Smectite Clay promoted by Interlayer Cations. *Scientific reports*, 2015. 5: p. 8775.
33. Busch, A., et al., Effects of Physical Sorption and Chemical Reactions of CO₂ in Shaly Caprocks. *Energy Procedia*, 2009. 1(1): p. 3229-3235.
34. Wollenweber, J., et al., Caprock and Overburden Processes in Geological CO₂ Storage: an Experimental Study on Sealing Efficiency and Mineral Alterations. *Energy Procedia*, 2009. 1(1): p. 3469-3476.

35. Busch, A., et al., Carbon Dioxide Storage Potential of Shales. *International Journal of Greenhouse Gas Control*, 2008. 2(3): p. 297-308.
36. Audigane, P., et al., Reactive Transport Modeling Using TOUGHREACT for the Long Term CO₂ Storage at Sleipner, North Sea. *Carbon Capture and Sequestration*, 2005. 2.
37. Eiken, O., et al., Lessons Learned From 14 Years of CCS Operations: Sleipner, In Salah and Snøhvit. *Energy Procedia*, 2011. 4: p. 5541-5548.
38. Gaus, I., M. Azaroual, and I. Czernichowski-Lauriol, Reactive Transport Modelling of the Impact of CO₂ Injection on the Clayey Cap Rock at Sleipner (North Sea). *Chemical Geology*, 2005. 217(3): p. 319-337.
39. Allen, P.A. and J.R. Allen, *Basin Analysis - Principles and Applications* (2nd Edition). John Wiley & Sons.
40. Li, Z., et al., CO₂ Sequestration in Depleted Oil and Gas Reservoirs--Caprock Characterization and Storage Capacity. *Energy Conversion and Management*, 2006. 47(11-12): p. 1372-1382.
41. Bryant, S. and L.W. Lake, Effect of Impurities on Subsurface CO₂ Storage Processes, in *Carbon Dioxide Capture for Storage in Deep Geologic Formations*. 2005, Elsevier Science: Amsterdam. p. 983-996.
42. Wang, J., et al., Effects of Impurities on CO₂ Transport, Injection and Storage. *Energy Procedia*, 2011. 4: p. 3071-3078.
43. Marcon, V. and J.P. Kaszuba, Carbon Dioxide–Brine–Rock Interactions in a Carbonate Reservoir Capped By Shale: Experimental Insights Regarding the Evolution of Trace Metals. *Geochimica Et Cosmochimica Acta*, 2015. 168: p. 22-42.
44. Busch, A., et al., Investigation of High-Pressure Selective Adsorption/Desorption Behaviour of CO₂ and CH₄ on Coals: An Experimental Study. *International Journal of Coal Geology*, 2006. 66(1-2): p. 53-68.
45. Busch, A. and A. Amann-Hildenbrand, Predicting Capillarity of Mudrocks. *Marine and Petroleum Geology*, 2013. 45: p. 208-223.
46. Bennett, R.H., W.R. Bryant, and M.H. Hulbert, *the Microstructure of Fine-Grained Sediments, From Mud to Shale*. 1991, New York: Springer-Verlag.
47. Hildenbrand, A., S. Schlömer, and B.M. Krooss, Gas Breakthrough Experiments on Fine-Grained Sedimentary Rocks. *Geofluids*, 2002. 2(1): p. 3-23.

48. Emmanuel, S., L.M. Anovitz, and R.J. Day-Stirrat, Effects of Coupled Chemo-Mechanical Processes on the Evolution of Pore-Size Distributions in Geological Media. *Rev Mineral Geochem*, 2015. 80: p. 45-60.
49. Mouzakis, K.M., et al., Experimental Study of Porosity Changes in Shale Caprocks Exposed to CO₂-Saturated Brines I: Evolution of Mineralogy, Pore Connectivity, Pore Size Distribution, and Surface Area. *Environmental Engineering Science*.
50. Miller, Q.R., et al., Experimental Study of Porosity Changes in Shale Caprocks Exposed to Carbon Dioxide-Saturated Brine II: Insights From Aqueous Geochemistry. *Environmental Engineering Science*. 33.10 (2016): p. 736-744.
51. Khan, S., et al., An Integrated Geomechanics Workflow for Caprock-Integrity Analysis of a Potential Carbon Storage, in *SPE International Conference on CO₂ Capture, Storage, and Utilization*. 2010: New Orleans, Louisiana, USA. doi:10.2118/139477-MS.
52. Vilarrasa, V., S. Olivella, and J. Carrera, Geomechanical Stability of the Caprock During CO₂ Sequestration in Deep Saline Aquifers. *Energy Procedia*, 2011. 4: p. 5306-5313.
53. Busch, A., et al., The Significance of Caprock Sealing Integrity for CO₂ Storage, in *SPE International Conference on CO₂ Capture, Storage, and Utilization*. 2010: New Orleans, Louisiana, USA. doi:10.2118/139588-MS.
54. Ellis, B.R., et al., Changes in Caprock Integrity Due to Vertical Migration of CO₂-Enriched Brine. *Energy Procedia*, 2011. 4: p. 5327-5334.
55. Mcpherson, B., Modeling Caprock Integrity: Assessment Objectives. *IEA-GHG CO₂ Geological Storage Modelling Workshop Orleans, France*, 2009.
56. Armitage, P.J., et al., Diagenetic and Sedimentary Controls on Porosity in Lower Carboniferous Fine-Grained Lithologies, Krechba Field, Algeria: a Petrological Study of a Caprock to a Carbon Capture Site. *Marine and Petroleum Geology*, 2010. 27(7): p. 1395-1410.
57. Ali, S.A., et al., Diagenesis and Reservoir Quality. *Oilfield Review*, 2010. 22(2): p. 14-27.
58. Duenckel, R., et al., Proppant Diagenesis--Integrated Analyses Provide New Insights Into Origin Occurrence and Implications for Proppant Performance. *SPE Production & Operations*, 2012. 27(02): p. 131-144.
59. Weaver, J.D., et al., Fracture-Related Diagenesis may Impact Conductivity. *SPE Journal*, 2007. 12(03): p. 272-281.

60. Katsube, T.J. and M.A. Williamson, Effects of Diagenesis on Shale Nano-Pore Structure and Implications for Sealing Capacity. *Clay Minerals*, 1994. 29(4): p. 451-472.
61. Kohler, E., T. Parra, and O. Vidal, Clayey Cap-Rock Behavior in H₂O-CO₂ Media at Low Pressure and Temperature Conditions: An Experimental Approach. *Clays and Clay Minerals*, 2009. 57(5): p. 616-637.
62. Nogues, J.P., et al., Permeability Evolution Due to Dissolution and Precipitation of Carbonates Using Reactive Transport Modeling in Pore Networks. *Water Resources Research*, 2013. 49(9): p. 6006-6021.
63. Armitage, P., et al., Permeability of the Mercia Mudstone: Suitability As Caprock to Carbon Capture and Storage Sites. *Geofluids* 16.1 (2016): p. 26-42.
64. Edlmann, K., S. Haszeldine, and C. Mcdermott, Experimental Investigation Into the Sealing Capability of Naturally Fractured Shale Caprocks to Supercritical Carbon Dioxide Flow. *Environmental Earth Sciences*, 2013. 70(7): p. 3393-3409.
65. Liu, F., et al., CO₂–Brine–Caprock Interaction: Reactivity Experiments on Eau Claire Shale and a Review of Relevant Literature. *International Journal of Greenhouse Gas Control*, 2012. 7: p. 153-167.
66. Elsworth, D. and H. Yasuhara, Mechanical and Transport Constitutive Models for Fractures Subject to Dissolution and Precipitation. *International Journal for Numerical and Analytical Methods in Geomechanics*, 2010. 34(5): p. 533-549.
67. Reynolds, M. and J. Buendia. Permanently Sequester Anthropogenic Carbon Dioxide-Through Hydraulic Fracturing. in *SPE Unconventional Resources Conference*. 2017. Society of Petroleum Engineers. doi:10.2118/185033-MS.
68. Nicot, J.p. and I.J. Duncan, Common attributes of Hydraulically Fractured Oil and Gas Production and CO₂ Geological Sequestration. *Greenhouse Gases: Science and Technology*, 2012. 2(5): p. 352-368.
69. Stack, A.G., Precipitation in Pores: A Geochemical Frontier. *Rev Mineral Geochem*, 2015. 80: p. 165-190.
70. Molins, S., Reactive Interfaces in Direct Numerical Simulation of Pore Scale Processes. *Rev Mineral Geochem*, 2015. 80: p. 461-481.
71. Vidic, R.D., et al., Impact of Shale Gas Development on Regional Water Quality. *Science*, 2013. 340(6134).

72. Amthor, J.E. and J. Okkerman, Influence of Early Diagenesis on Reservoir Quality of Rotliegende Sandstones, Northern Netherlands. AAPG Bulletin, 1998. 82(12): p. 2246-2265.
73. Wendler, J., et al., Carbonate Diagenesis and Feldspar Alteration in Fracture-Related Bleaching Zones (Buntsandstein, Central Germany): Possible Link to CO₂-Influenced Fluid–Mineral Reactions. International Journal of Earth Sciences, 2012. 101(1): p. 159-176.
74. Altundas, B., et al., Retardation of CO₂ Migration Due to Capillary Pressure Hysteresis: a New CO₂ Trapping Mechanism, in SPE International Conference on CO₂ Capture, Storage, and Utilization. 2010: New Orleans, Louisiana, USA. doi:10.2118/139641-MS.
75. Soldal, M., Caprock Interaction with CO₂: Geomechanical and Geochemical Effects, in Department of Geosciences. 2008, University of Oslo: Oslo. p. 106.
76. Pashin, J.C. and M.R. McIntyre, Temperature–Pressure Conditions in Coalbed Methane Reservoirs of the Black Warrior Basin: Implications for Carbon Sequestration and Enhanced Coalbed Methane Recovery. International Journal of Coal Geology, 2003. 54(3): p. 167-183.
77. Espinoza, D.N. and J.C. Santamarina, Water-CO₂-Mineral Systems: Interfacial Tension, Contact Angle, and Diffusion; Implications to CO₂ Geological Storage. Water Resour. Res., 2010. 46(7): p. W07537.
78. Moulton, O.A., et al., Self-Diffusion Coefficients of the Binary H₂O–CO₂ Mixture at High Temperatures and Pressures. the Journal of Chemical thermodynamics 93 (2016): p. 424-429.
79. Busch, A. and N. Müller, Determining CO₂/Brine Relative Permeability and Capillary Threshold Pressures for Reservoir Rocks and Caprocks: Recommendations for Development of Standard Laboratory Protocols. Energy Procedia, 2011. 4: p. 6053-6060.
80. Blaich, M.E. Developing Effective and Environmentally Suitable Fracturing Fluids Using Hydraulic Fracturing Flowback Waters. in SPE Unconventional Gas Conference. 2010. Society of Petroleum Engineers. doi:10.2118/131784-MS
81. EPA, Characteristics of Coalbed Methane Production and Associated Hydraulic Fracturing Practices. Evaluation of Impacts to Underground Sources of Drinking Water by Hydraulic Fracturing of Coalbed Methane Reservoirs, 2004: p. 32.
82. USGS, Summary of Studies Related to Hydraulic Fracturing Conducted by USGS Water Science Centers. USGS, 2012. 5: p. 1 - 8.

83. Chalbaud, C., et al., Interfacial Tension Measurements and Wettability Evaluation for Geological CO₂ Storage. *Advances in Water Resources*, 2009. 32(1): p. 98-109.
84. Hildenbrand, A., et al., Gas Breakthrough Experiments on Pelitic Rocks: Comparative Study with N₂, CO₂ and CH₄. *Geofluids*, 2004. 4(1): p. 61-80.
85. Bacon, D.H., et al., CO₂ Storage by Sorption on Organic Matter and Clay in Gas Shale. *Journal of Unconventional Oil and Gas Resources*, 2015. 12: p. 123-133.
86. Xu, T., J.A. Apps, and K. Pruess, Mineral Sequestration of Carbon Dioxide in a Sandstone–Shale System. *Chemical Geology*, 2005. 217(3): p. 295-318.
87. Schieber, J., Reverse Engineering Mother Nature—Shale Sedimentology From An Experimental Perspective. *Sedimentary Geology*, 2011. 238(1): p. 1-22.
88. Anovitz, L.M. and D.R. Cole, Characterization and Analysis of Porosity and Pore Structures. *Rev Mineral Geochem*, 2015. 80: p. 61-164.
89. Bennion, D.B. and S. Bachu, Permeability and Relative Permeability Measurements at Reservoir Conditions for CO₂-Water Systems in Ultra Low Permeability Confining Caprocks, in EUROPEC/EAGE Conference and Exhibition. 2007: London, U.K.
90. Al-Bazali, T.M., et al., Measurement of the Sealing Capacity of Shale Caprocks, in SPE Annual Technical Conference and Exhibition. 2005: Dallas, Texas. doi:10.2118/96100-MS.
91. Johnson, J. W., J.J. Nitao and J.P. Morris, Environmental Sciences Division, Lawrence Livermore National Laboratory, Livermore, CA, USA, Reactive Transport Modeling of Cap-Rock Integrity During Natural and Engineered CO₂ Storage. *Carbon Dioxide Capture for Storage in Deep Geologic Formations*, 2005. Vol. 2.
92. Morris, J., S. Johnson, and S.J. Friedmann, Geomechanical Simulations of Caprock Integrity Using the Livermore Distinct Element Method. 2008. Medium: ED; Size: PDF-File: 10 Pages; Size: 1 Mbytes.
93. Amann-Hildenbrand, A., et al., Experimental Investigation of the Sealing Capacity of Generic Clay-Rich Caprocks. *International Journal of Greenhouse Gas Control*, 2013. 19: p. 620-641.
94. Hensen, E.J.M. and B. Smit, Why Clays Swell. *the Journal of Physical Chemistry B*, 2002. 106(49): p. 12664-12667.
95. Eke, P.E., A. Curtis, and S. Haszeldine, CO₂-Brine Surface Dissolution and Injection: CO₂ Storage Enhancement, in *Offshore Europe*. 2009: Aberdeen, UK.

96. Kampman, N., et al., Drilling and Sampling a Natural CO₂ Reservoir: Implications for Fluid Flow and CO₂-Fluid–Rock Reactions During CO₂ Migration Through the Overburden. *Chemical Geology*, 2013.
97. Ruiz-Agudo, E., C. Putnis, and A. Putnis, Coupled Dissolution and Precipitation at Mineral–Fluid Interfaces. *Chemical Geology*, 2014. 383: p. 132-146.
98. Rimmelé, G., V. Barlet-Gouédard, and F. Renard, Evolution of the Petrophysical and Mineralogical Properties of Two Reservoir Rocks Under thermodynamic Conditions Relevant for CO₂ Geological Storage at 3 Km Depth. *Oil & Gas Science and Technology–Revue De l’Institut Français Du Pétrole*, 2010. 65(4): p. 565-580.
99. Olson, J.E., S.E. Laubach, and R.H. Lander, Natural Fracture Characterization in Tight Gas Sandstones: Integrating Mechanics and Diagenesis. *AAPG Bulletin*, 2009. 93(11): p. 1535-1549.
100. Johnson, J.W., J.J. Nitao, and C. I. Steefel, Fundamental Elements of Geologic CO₂ Sequestration in Saline Aquifers, G.A.E.T. Division and L.L.N. Laboratory, Editors. 2006: Livermore, CA 94550.
101. Carroll, S.A., W.W. McNab, and S.C. Torres, Experimental Study of Cement-Sandstone/Shale-Brine-CO₂ Interactions. *Geochemical Transactions*, 2011. 12(1): p. 9.
102. Carroll, S., et al., Wellbore Integrity in Carbon Sequestration Environments: 1. Experimental Study of Cement-Sandstone/Shale-Brine-CO₂. *Energy Procedia*, 2011. 4: p. 5186-5194.
103. De Lucia, M., et al., Modelling CO₂-Induced Fluid–Rock Interactions in the Altensalzwedel Gas Reservoir. Part I: From Experimental Data to a Reference Geochemical Model. *Environmental Earth Sciences*, 2012. 67(2): p. 563-572.
104. Peters, C., et al., Basin-Scale Leakage Risks From Geologic Carbon Sequestration: Impact on Carbon Capture and Storage Energy Market Competitiveness. 2013, the Trustees of Princeton University DOE Award DE-FE0000749, Final Technical Report Number DOE/FE0000749-41.
105. Giammar, D.E., R.G. Bruant Jr, and C.A. Peters, Forsterite Dissolution and Magnesite Precipitation at Conditions Relevant for Deep Saline Aquifer Storage and Sequestration of Carbon Dioxide. *Chemical Geology*, 2005. 217(3): p. 257-276.
106. Bergaya, F. and G. Lagaly, Chapter 1 General Introduction: Clays, Clay Minerals, and Clay Science, in *Developments in Clay Science*, B.K.G.T. Faïza Bergaya and L. Gerhard, Editors. 2006, Elsevier. p. 1-18.

107. Lagaly, G., Chapter 5 Colloid Clay Science, in *Developments in Clay Science*, B.K.G.T. Faïza Bergaya and L. Gerhard, Editors. 2006, Elsevier. p. 141-245.
108. Tournassat, C., et al., *Natural and Engineered Clay Barriers*. Vol. 6. 2015: Elsevier.
109. Landais, p. and J.-F. Aranyosy, *Clays in Natural and Engineered Barriers for Radioactive Waste Confinement. Physics and Chemistry of the Earth, Parts A/B/C*, 2011. 36(17): p. 1437.
110. Bildstein, O. and F. Claret, Chapter 5 - Stability of Clay Barriers Under Chemical Perturbations, in *Developments in Clay Science*, C.I.S.I.C.B. Christophe Tournassat and B. Faqza, Editors. 2015, Elsevier. p. 155-188.
111. Lagaly, G., M. Ogawa, and I. Dékány, Chapter 7.3 Clay Mineral Organic Interactions, in *Developments in Clay Science*, B.K.G.T. Faïza Bergaya and L. Gerhard, Editors. 2006, Elsevier. p. 309-377.
112. Sterpenich, J., et al., Experimental Simulation of the Impact of a thermal Gradient on a Clayey Caprock Submitted to the Combined Action of Water and CO₂.
113. Steefel, C.I., L.E. Beckingham, and G. Landrot, Micro-Continuum Approaches for Modeling Pore-Scale Geochemical Processes. *Rev Mineral Geochem*, 2015. 80: p. 217-246.
114. Xu, T., et al., TOUGHREACT--A Simulation Program for Non-Isothermal Multiphase Reactive Geochemical Transport in Variably Saturated Geologic Media: Applications to Geothermal Injectivity and CO₂ Geological Sequestration. *Computers & Geosciences*, 2006. 32(2): p. 145-165.
115. Credo, A., et al., Mixed-Layer Illite–Smectite Reactivity in Acidified Solutions: Implications for Clayey Caprock Stability in CO₂ Geological Storage. *Applied Clay Science*, 2011. 53(3): p. 402-408.
116. Beckingham, L.E., et al., Evaluation of Mineral Reactive Surface Area Estimates for Prediction of Reactivity of a Multi-Mineral Sediment. *Geochimica Et Cosmochimica Acta*, 2016. 188: p. 310-329.
117. Schoonheydt, R.A. and C.T. Johnston, Chapter 3 Surface and Interface Chemistry of Clay Minerals, in *Developments in Clay Science*, B.K.G.T. Faïza Bergaya and L. Gerhard, Editors. 2006, Elsevier. p. 87-113.

118. Olabode, A. and M. Radonjic, Characterization of Shale Cap-Rock Nano-Pores in Geologic CO₂ Containment. *Environmental & Engineering Geoscience*, 2014. 20(4): p. 361-370.
119. Bertier, P., et al., on the Use and Abuse of N₂ Physisorption for the Characterization of the Pore Structure of Shales. *Clay Clay Miner*, 2016.
120. Liu, C., et al., Pore-Scale Process Coupling and Effective Surface Reaction Rates in Heterogeneous Subsurface Materials. *Rev Mineral Geochem*, 2015. 80: p. 191-216.
121. Hong, M. and H.H. Teng, Implications of Solution Chemistry Effects: Direction-Specific Restraints on the Step Kinetics of Calcite Growth. *Geochimica Et Cosmochimica Acta*, 2014. 141: p. 228-239.
122. Golubev, S.V., O.S. Pokrovsky, and J. Schott, Experimental Determination of the Effect of Dissolved CO₂ on the Dissolution Kinetics of Mg and Ca Silicates at 25°C. *Chemical Geology*, 2005. 217(3): p. 227-238.
123. Min, Y. and Y.-S. Jun, Anorthite Dissolution Under Conditions Relevant to Subsurface CO₂ Injection: Effects of Na⁺, Ca²⁺, and Al³⁺. *Environmental Science & Technology*, 2016.
124. Yang, L., et al., CO₂-Induced Geochemical Reactions in Heterogeneous Sandstone and Potential Conditions Causing the Tight Cementation. *Applied Geochemistry*, 2017.
125. Brigatti, M.F., E. Galan, and B.K.G. theng, Chapter 2 Structures and Mineralogy of Clay Minerals, in *Developments in Clay Science*, B.K.G.T. Faïza Bergaya and L. Gerhard, Editors. 2006, Elsevier. p. 19-86.
126. Tournassat, C. and C.I. Steefel, Ionic Transport in Nano-Porous Clays with Consideration of Electrostatic Effects. *Rev Mineral Geochem*, 2015. 80: p. 287-329.
127. Giesting, P., et al., Interaction of Carbon Dioxide with Na-Exchanged Montmorillonite at Pressures to 640bars: Implications for CO₂ Sequestration. *International Journal of Greenhouse Gas Control*, 2012. 8: p. 73-81.
128. Petro, M. Experimental Study of Rock-Fluid Interaction Using Automated Multichannel System Operated Under Conditions of CO₂-Based Geothermal Systems. in *38th Annual Workshop on Geothermal Reservoir Engineering*, Stanford, CA, Feb. 11-13, 2013. 2014.
129. Wan, Y., et al., Experimental and Numerical Simulation Study of the Mineral Sequestration Mechanism of the Shiqianfeng Saline Aquifers in the Ordos Basin, Northwest China. *Environmental Earth Sciences*, 2017. 76(1): p. 43.

130. Labus, K., et al., Preliminary Geochemical Modeling of Water–Rock–Gas Interactions Controlling CO₂ Storage in the Badenian Aquifer within Czech Part of Vienna Basin. *Environmental Earth Sciences*, 2016. 75(14): p. 1-13.
131. Wigand, M., et al., Geochemical Effects of CO₂ Sequestration on Fractured Wellbore Cement at the Cement/Caprock Interface. *Chemical Geology*, 2009. 265(1-2): p. 122-133.
132. Lima, V.D., et al., CO₂ Geological Storage in Saline Aquifers: Paraná Basin Caprock and Reservoir Chemical Reactivity. *Energy Procedia*, 2011. 4: p. 5377-5384.
133. Rosenbauer, R.J., T. Koksalan, and J.L. Palandri, Experimental Investigation of CO₂-Brine-Rock Interactions at Elevated Temperature and Pressure: Implications for CO₂ Sequestration in Deep-Saline Aquifers. *Fuel Processing Technology*, 2005. 86(14-15): p. 1581-1597.
134. Shipton, Z.K., et al., Natural Leaking CO₂-Charged Systems As Analogs for Failed Geologic Storage Reservoirs, in *Carbon Dioxide Capture for Storage in Deep Geologic Formations*. 2005, Elsevier Science: Amsterdam. p. 699-712.
135. Sathaye, K.J., et al., Constraints on the Magnitude and Rate of CO₂ Dissolution at Bravo Dome Natural Gas Field. *Proceedings of the National Academy of Sciences*, 2014. 111(43): p. 15332-15337.
136. Cantucci, B., et al., Geochemical Barriers in CO₂ Capture and Storage Feasibility Studies. *Transport in Porous Media*, 2015. 106(1): p. 107-143.
137. Putnis, A., Transient Porosity Resulting From Fluid–Mineral Interaction and Its Consequences. *Rev Mineral Geochem*, 2015. 80: p. 1-23.
138. Røyne, A. and B. Jamtveit, Pore-Scale Controls on Reaction-Driven Fracturing. *Reviews in Mineralogy and Geochemistry*, 2015. 80(1): p. 25-44.
139. Zoback, M.D. and S.M. Gorelick, to Prevent Earthquake Triggering, Pressure Changes Due to CO₂ Injection Need to Be Limited. *Proceedings of the National Academy of Sciences*, 2015. 112(33): p. E4510-E4510.
140. Navarre-Sitchler, A., S.L. Brantley, and G. Rother, How Porosity Increases during Incipient Weathering of Crystalline Silicate Rocks. *Rev Mineral Geochem*, 2015. 80: p. 331-354.
141. Druhan, J.L., S.T. Brown, and C. Huber, Isotopic Gradients Across Fluid–Mineral Boundaries. *Reviews in Mineralogy and Geochemistry*, 2015. 80(1): p. 355-391.

142. Frery, E., et al., Geochemical Transect through a Travertine Mount: A Detailed Record of CO₂-Enriched Fluid Leakage from Late Pleistocene to Present-Day–Little Grand Wash Fault (Utah, USA). *Quaternary International*, 2016.
143. Mcdermott, C.I., et al., Natural Analogue Studies, in *Geological Storage of CO₂ in Deep Saline Formations*. 2017, Springer. p. 473-520.
144. Mehmani, Y. and M.T. Balhoff, Mesoscale and Hybrid Models of Fluid Flow and Solute Transport. *Rev Mineral Geochem*, 2015. 80: p. 433-459.
145. Johnson, J.W., J.J. Nitao, and K.G. Knauss, Reactive Transport Modeling of CO₂ Storage in Saline Aquifers to Elucidate Fundamental Processes, Trapping Mechanisms and Sequestration Partitioning. *Geological Storage of Carbon Dioxide*, 2004. 233: p. 107-128.
146. Ellis, B.R., et al., Dissolution-Driven Permeability Reduction of a Fractured Carbonate Caprock. *Environmental Engineering Science*, 2013. 30(4): p. 187-193.
147. Keller, A.A., *Single and Multiphase Flow and Transport in Fractured Porous Media*. 1996, Stanford University.
148. Park, Y., et al., Sequestering Carbon Dioxide Into Complex Structures of Naturally Occurring Gas Hydrates. *Proceedings of the National Academy of Sciences*, 2006. 103(34): p. 12690-12694.
149. Lo Ré, C., et al., Fluid–Rock Interactions in CO₂-Saturated, Granite-Hosted Geothermal Systems: Implications for Natural and Engineered Systems From Geochemical Experiments and Models. *Geochimica et Cosmochimica Acta*, 2014. 141: p. 160-178.
150. Noiriél, C., Resolving Time-Dependent Evolution of Pore-Scale Structure, Permeability and Reactivity Using X-Ray Microtomography. *Rev Mineral Geochem*, 2015. 80: p. 247-285.
151. Yoon, H., Q. Kang, and A. Valocchi, Lattice Boltzmann-Based Approaches for Pore-Scale Reactive Transport. *Rev Mineral Geochem*, 2015. 80: p. 393-431.
152. Kampman, N., et al., Observational Evidence Confirms Modelling of the Long-Term Integrity of CO₂-Reservoir Caprocks. *Nature Communications*, 2016. 7.
153. Kim, T.H., J. Cho, and K.S. Lee, Evaluation of CO₂ Injection in Shale Gas Reservoirs with Multi-Component Transport and Geomechanical Effects. *Applied Energy*, 2017. 190: p. 1195-1206.

154. Pawar, R.J., et al., Recent Advances in Risk Assessment and Risk Management of Geologic CO₂ Storage. *International Journal of Greenhouse Gas Control*, 2015. 40: p. 292-311.
155. Goldberg, D.S., T. Takahashi, and A.L. Slagle, Carbon Dioxide Sequestration in Deep-Sea Basalt. *Proceedings of the National Academy of Sciences*, 2008. 105(29): p. 9920-9925.
156. Jenkins, C.R., et al., Safe Storage and Effective Monitoring of CO₂ in Depleted Gas Fields. *Proceedings of the National Academy of Sciences*, 2012. 109(2): p. E35-E41.
157. Sadhukhan, S., P. Gouze, and T. Dutta, A Simulation Study of Reactive Flow in 2-D Involving Dissolution and Precipitation in Sedimentary Rocks. *Journal of Hydrology*, 2014.
158. Ahmad, N., et al., Reactive Transport Modeling of Leaking CO₂-Saturated Brine Along a Fractured Pathway. *International Journal of Greenhouse Gas Control*, 2015. 42: p. 672-689.
159. Algive, L., Et Al. Reactive Transport: Experiments and Pore Network Modelling. in Paper SCA2007-10 Presented at the International Symposium of the Society of Core Analysts, Calgary, Canada. 2007.
160. Neunhauserer, L., et al., Flow and Transport Processes in Fractured Porous Media. *Computational Methods in Water Resources XII. Volume 2*, 1998: p. 101-108.
161. Sarkar, S., M.N. Toksoz, and D.R. Burns, Fluid Flow Simulation in Fractured Reservoirs. 2002, Massachusetts Institute of Technology. Earth Resources Laboratory.
162. Rezaeyan, A., et al., A Laboratory Study on Capillary Sealing Efficiency of Iranian Shale and Anhydrite Caprocks. *Marine and Petroleum Geology*, 2015.
163. Shah, V., D.F. Broseta, and G. Mouronval. Capillary Alteration of Caprocks by Acid Gases. in SPE Symposium on Improved Oil Recovery. 2008. Society of Petroleum Engineers.
164. Farokhpour, R., Akervol I., Torsater O., Bjorkvik B.J.A. CO₂ Capillary Entry Pressure Into Flow Barrier and Caprock. in SCA Symposium. 2013. California.
165. Aggelopoulos, C.A., M. Robin, and O. Vizika, Interfacial Tension Between CO₂ and Brine (NaCl + CaCl₂) at Elevated Pressures and Temperatures: the Additive Effect of Different Salts. *Advances in Water Resources*, 2011. 34(4): p. 505-511.

166. Zhu, H.-Y., et Al. Multiscale Change Characteristics of Chinese Wufeng Shale Under Supercritical Carbon Dioxide. in SPE Annual Technical Conference and Exhibition. 2016. Society of Petroleum Engineers. doi:10.2118/181369-MS.
167. Dávila, G., et al., Interaction Between a Fractured Marl Caprock and CO₂-Rich Sulfate Solution Under Supercritical CO₂ Conditions. *International Journal of Greenhouse Gas Control* 48 (2016): p. 105-119.
168. Schütt, H., M. Wigand, and E. Spangenberg, Geophysical and Geochemical Effects of Supercritical CO₂ on Sandstones, in *Carbon Dioxide Capture for Storage in Deep Geologic Formations*. 2005, Elsevier Science: Amsterdam. p. 767-786.
169. Sidiq, H.H. and R. Amin, Supercritical CO₂/Methane Relative Permeability Investigation, in *SPE International Conference on CO₂ Capture, Storage, and Utilization*. 2010: New Orleans, Louisiana, USA. doi:10.2118/137884-MS.
170. Ishiwatari, H.Y.A.R., Characterization of Organic Matter Generated From Green River Shale by Infrared Laser Pyrolysis. *Geochemical Journal*, 2002. 36: p. 73-82.
171. Selvadurai, A.P.S., Fluid Leakage Through Fractures in An Impervious Caprock Embedded Between Two Geologic Aquifers. *Advances in Water Resources*, 2012. 41: p. 76-83.
172. Jung, H.B., et al., Wellbore Cement Fracture Evolution at the Cement–Basalt Caprock Interface During Geologic Carbon Sequestration. *Applied Geochemistry*, 2014. 47: p. 1-16.
173. Noh, M.H. and L.W. Lake. Geochemical Modeling of Fracture Filling. in *SPE/DOE Improved Oil Recovery Symposium*. 2002. Society of Petroleum Engineers.
174. Yu, D. and A. Ladd, A Numerical Simulation Method for Dissolution in Porous and Fractured Media. *Journal of Computational Physics*, 2010. 229(18): p. 6450-6465.
175. Chappell, B.A., Deformational Response of Differently Shaped and Sized Test Pieces of Shale Rock. *International Journal of Rock Mechanics and Mining Sciences & Geomechanics Abstracts*, 1974. 11(1): p. 21-25.
176. Yasuhara, H., et al., Evolution of Fracture Permeability Through Reactive Flow at Elevated Temperature. *Trans. Geotherm. Res. Council*, 2005. 29: p. 437-441.
177. Yasuhara, H. and D. Elsworth, A Numerical Model Simulating Reactive Transport and Evolution of Fracture Permeability. *International Journal for Numerical and Analytical Methods in Geomechanics*, 2006. 30(10): p. 1039-1062.

178. Weaver, J.D. and R.D. Rickman. Productivity Impact from Geochemical Degradation of Hydraulic Fractures. in SPE Deep Gas Conference and Exhibition. 2010. Society of Petroleum Engineers. doi:10.2118/130641-MS.
179. Weaver, J.D., R.D. Rickman, and H. Luo, Fracture-Conductivity Loss Caused by Geochemical Interactions Between Man-Made Proppants and Formations. SPE Journal, 2010. 15(01): p. 116-124.
180. De Borst, R., J. Réthoré, and M.-A. Abellan, Two-Scale Approaches for Fracture in Fluid-Saturated Porous Media. Interaction and Multiscale Mechanics: An International Journal, 2007. 1: p. 83-101.
181. De Borst, R., J. Rethore, and M.-A. Abellan, A Precis of Two-Scale Approaches for Fracture in Porous Media, in Lecture Notes on Composite Materials. 2009, Springer. p. 149-171.
182. Edlmann, K., et al., Appraisal of Global CO₂ Storage Opportunities Using the Geomechanical Facies Approach. Environmental Earth Sciences: p. 1-22.
183. Kang, Q., D. Zhang, and S. Chen, Simulation of Dissolution and Precipitation in Porous Media. J. Geophys. Res., 2003. 108(B10): p. 2505.
184. Wilson-Lopez, R. and F. Rodriguez. A Network Model for Two-Phase Flow in Microfractured Porous Media. in SPE International Petroleum Conference in Mexico. 2004. Society of Petroleum Engineers. doi:10.2118/92056-MS.
185. Rosen, B. and C. König, Calculation and Interpretation of Interaction Between Fluid Flow and Deformation in Fractured Rock. http://www.delta-h.de/DELTAH/referenzen/ck_veroeffentlichungen/veroeff_fluid.pdf.
186. Yalcinkaya, T., Experimental Study on Single Cement Fracture Exposed to CO₂ Saturated Brine Under Dynamic Conditions, in Petroleum Engineering. 2010, Unpublished Thesis, Louisiana State University: Baton Rouge. p. 105.
187. White, J.A., et al., Geomechanical Behavior of the Reservoir and Caprock System at the in Salah CO₂ Storage Project. Proceedings of the National Academy of Sciences, 2014. 111(24): p. 8747-8752.
188. Ferronato, M., et al., Geomechanical Issues of Anthropogenic CO₂ Sequestration in Exploited Gas Fields. Energy Conversion and Management, 2010. 51(10): p. 1918-1928.

189. David, C. and M. Le Ravalec-Dupin, Rock Physics and Geomechanics in the Study of Reservoirs and Repositories. Geological Society, London, Special Publications, 2007. 284(1): p. 1-14.
190. Kjølner, C., et al., Novel Experimental/Numerical Approach to Evaluate the Permeability of Cement-Caprock Systems. International Journal of Greenhouse Gas Control, 2016. 45: p. 86-93.
191. Bastian, P., et al., Numerical Simulation of Multiphase Flow in Fractured Porous Media, in Numerical Treatment of Multiphase Flows in Porous Media. 2000, Springer. p. 50-68.
192. Bagherieh, A., et al., Drying Response and Effective Stress in a Double Porosity Aggregated Soil. Engineering Geology, 2009. 105(1): p. 44-50.
193. Alfred, D., Modeling Fluid Flow Through Single Fracture Using Experimental, Stochastic, and Simulation Approaches. 2004, Unpublished Thesis, Texas A&M University.
194. Veer, E., S. Van Der Waldmann, and P. Fokker. A Coupled Geochemical-Transport-Geomechanical Model to Address Caprock Integrity During Long-Term CO₂ Storage. in 49th US Rock Mechanics/Geomechanics Symposium. 2015. American Rock Mechanics Association.
195. Smith, J., et al., Carbon Dioxide Storage Risk Assessment: Analysis of Caprock Fracture Network Connectivity. International Journal of Greenhouse Gas Control, 2011. 5(2): p. 226-240.
196. Streit, J.E., A.F. Siggins, and B.J. Evans, Predicting and Monitoring Geomechanical Effects of CO₂ Injection, in Carbon Dioxide Capture for Storage in Deep Geologic Formations. 2005, Elsevier Science: Amsterdam. p. 751-766.
197. Moreno, F.J., R. Chalaturnyk, and J. Jimenez, Methodology for Assessing Integrity of Bounding Seals (Wells and Caprock) for Geological Storage of CO₂, in Greenhouse Gas Control Technologies 7, E.S. Rubin, et al., Editors. 2005, Elsevier Science Ltd: Oxford. p. 731-739.
198. Zhou, X., Z. Zeng, and H. Liu, Laboratory Testing on Pierre Shale for CO₂ Sequestration Under Clayey Caprock, in 44th U.S. Rock Mechanics Symposium and 5th U.S.-Canada Rock Mechanics Symposium. 2010, American Rock Mechanics Association: Salt Lake City, Utah.

199. Heath, J.E., et al., Pore-Lining Phases and Capillary Breakthrough Pressure of Mudstone Caprocks: Sealing Efficiency of Geologic CO₂ Storage Sites. *International Journal of Greenhouse Gas Control*, 2012. 11: p. 204-220.
200. Wu, Y.-S., Numerical Simulation of Single-Phase and Multiphase Non-Darcy Flow in Porous and Fractured Reservoirs. *Transport in Porous Media*, 2002. 49(2): p. 209-240.
201. Hangx, S.J.T., C.J. Spiers, and C.J. Peach, the Effect of Deformation on Permeability Development in Anhydrite and Implications for Caprock Integrity During Geological Storage of CO₂. *Geofluids*, 2010. 10(3): p. 369-387.
202. Hangx, S., C. Spiers, and C. Peach, the Mechanical Behavior of Anhydrite and the Effect of CO₂ Injection. *Energy Procedia*, 2009. 1(1): p. 3485-3492.
203. Vernescu, B., Convergence Results for the Homogenization of Flow in Fractured Porous Media. Unpublished Thesis, University of Minnesota, 1990.
204. Diomampo, G.P., Relative Permeability Through Fractures, Technical Report, Department of Energy and Department of Petroleum Engineering, Editor. 2001: Stanford, California.
205. Macquarrie, K.T.B. and K.U. Mayer, Reactive Transport Modeling in Fractured Rock: A State-Of-the-Science Review. *Earth-Science Reviews*, 2005. 72(3-4): p. 189-227.
206. Chen, Z.M., et al., Appraising Carbon Geological Storage Potential in Unconventional Reservoirs Using Well-Testing Method: Engineering Parameters Analysis. *Society of Petroleum Engineers*. doi:NA
207. Li, P., et al., Assessment of the Effective CO₂ Storage Capacity in the Beibuwan Basin, Offshore of Southwestern P. R. China. *International Journal of Greenhouse Gas Control*, 2015. 37: p. 325-339.
208. Szulczewski, M.L., et al., Lifetime of Carbon Capture and Storage As a Climate-Change Mitigation Technology. *Proceedings of the National Academy of Sciences*, 2012. 109(14): p. 5185-5189.
209. Zhang, R., et al., A Novel Computational Framework for thermal-Hydrological-Mechanical-Chemical Processes of CO₂ Geological Sequestration Into a Layered Saline Aquifer and a Naturally Fractured Enhanced Geothermal System. *Greenhouse Gases: Science and Technology*, 2015.
210. Randolph, J.B. and M.O. Saar, Coupling Carbon Dioxide Sequestration with Geothermal Energy Capture in Naturally Permeable, Porous Geologic Formations: Implications for CO₂ Sequestration. *Energy Procedia*, 2011. 4: p. 2206-2213.

211. Sasaki, S., Characteristics of Microseismic Events Induced During Hydraulic Fracturing Experiments at the Hijiori Hot Dry Rock Geothermal Energy Site, Yamagata, Japan. *Tectonophysics*, 1998. 289(1): p. 171-188.
212. Lyon, T.A., et al., Integrated Study of a Faulted and Fractured Reservoir, in Abu Dhabi International Petroleum Exhibition and Conference. 1998, Society of Petroleum Engineers: Abu Dhabi, United Arab Emirates. doi:10.2118/49453-MS
213. Goodarzi, S., et al., Thermal Aspects of Geomechanics and Induced Fracturing in CO₂ Injection with Application to CO₂ Sequestration in Ohio River Valley, in SPE International Conference on CO₂ Capture, Storage, and Utilization. 2010: New Orleans, Louisiana, USA. doi:10.2118/139706-MS.
214. Mutschler, T., T. Triantafyllidis, and K. Balthasar, Geotechnical Investigations of Cap Rocks above CO₂-Reservoirs. *Energy Procedia*, 2009. 1(1): p. 3375-3382.
215. Verdon, J.P., et al., Comparison of Geomechanical Deformation Induced by Megatonne-Scale CO₂ Storage at Sleipner, Weyburn, and in Salah. *Proceedings of the National Academy of Sciences*, 2013. 110(30): p. E2762-E2771.
216. Gaus, I., Role and Impact of CO₂-Rock Interactions During CO₂ Storage in Sedimentary Rocks. *International Journal of Greenhouse Gas Control*, 2010. 4(1): p. 73-89.
217. Bourg, I.C., Sealing Shales Versus Brittle Shales: A Sharp Threshold in the Material Properties and Energy Technology Uses of Fine-Grained Sedimentary Rocks. *Environmental Science & Technology Letters*, 2015. 2(10): p. 255-259.
218. Haluszczak, L.O., A.W. Rose, and L.R. Kump, Geochemical Evaluation of Flowback Brine from Marcellus Gas Wells in Pennsylvania, USA. *Applied Geochemistry*, 2013. 28: p. 55-61.
219. Oliver, W.C. and G.M. Pharr, Measurement of Hardness and Elastic Modulus by Instrumented Indentation: Advances in Understanding and Refinements to Methodology. *Journal of Materials Research*, 2004. 19(01): p. 3-20.
220. Zhang, G., Z. Wei, and R.E. Ferrell, Elastic Modulus and Hardness of Muscovite and Rectorite Determined by Nanoindentation. *Applied Clay Science*, 2009. 43(2): p. 271-281.
221. Dicman, A., E. Putra, and D.S. Schechter, Modeling Fluid Flow through Single Fractures Using Experimental, Stochastic and Simulation Approaches. 2004, Society of Petroleum Engineers. doi:10.2118/89442-MS.
222. Lee, J. and R.A. Wattenbarger, *Gas Reservoir Engineering*. 1996.

APPENDIX A

EQUIPMENT AND MATERIALS USED FOR SHALE ROCK/CO₂ BRINE EXPERIMENTS



Figure A.1: Core flooding setup showing core holder and instrumentation



Figure A.2: Helium porosimetry unit for estimation of porosity of fractured cores

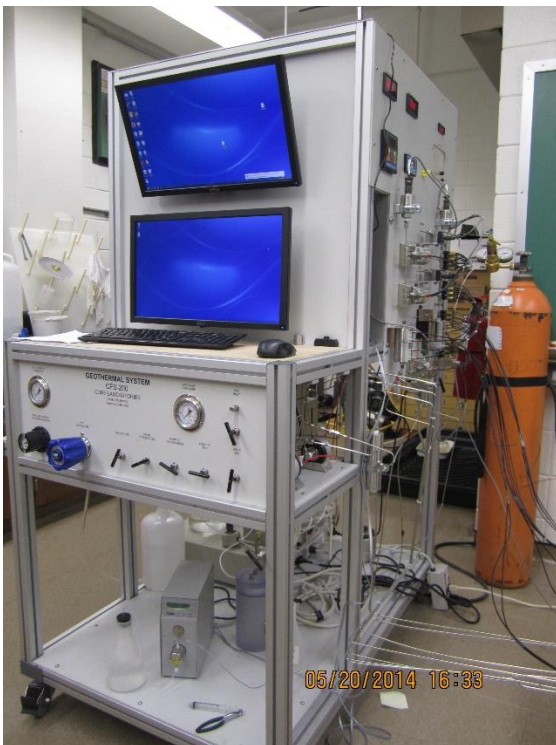


Figure A.3: Core flooding control unit



Figure A.4: Automated oven for temperature control



Figure A.5: Piston pump



Figure A.6: PEEK micro-tubing used in composite

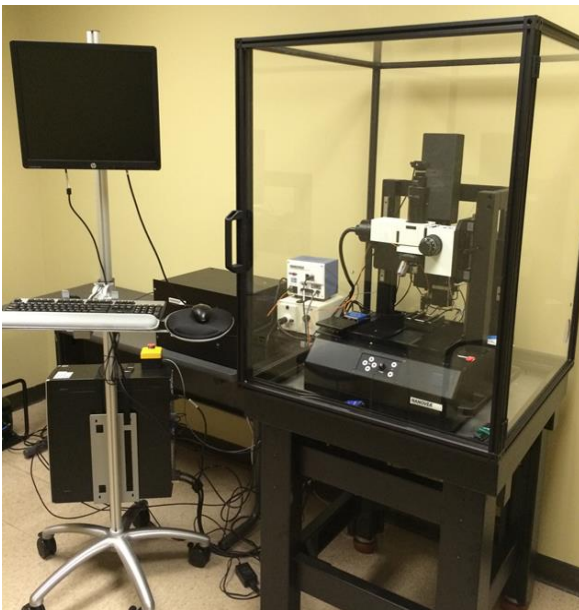


Figure A.7: Micro-indentation Fixture

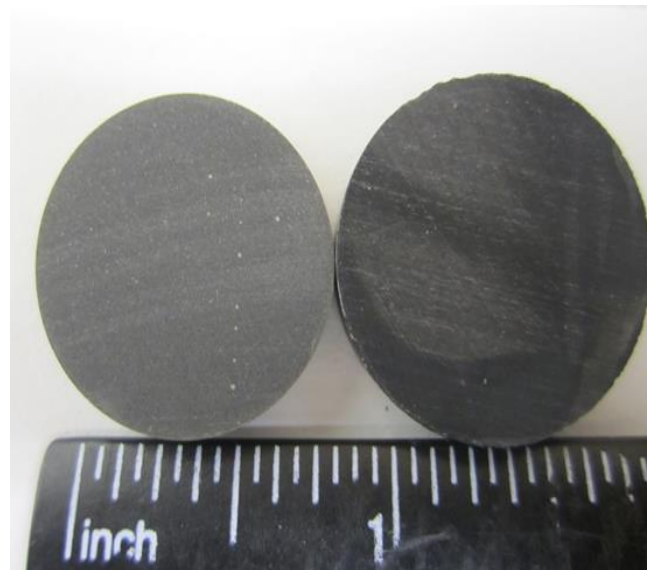


Figure A.8: Example of shale fragment and the indentation points

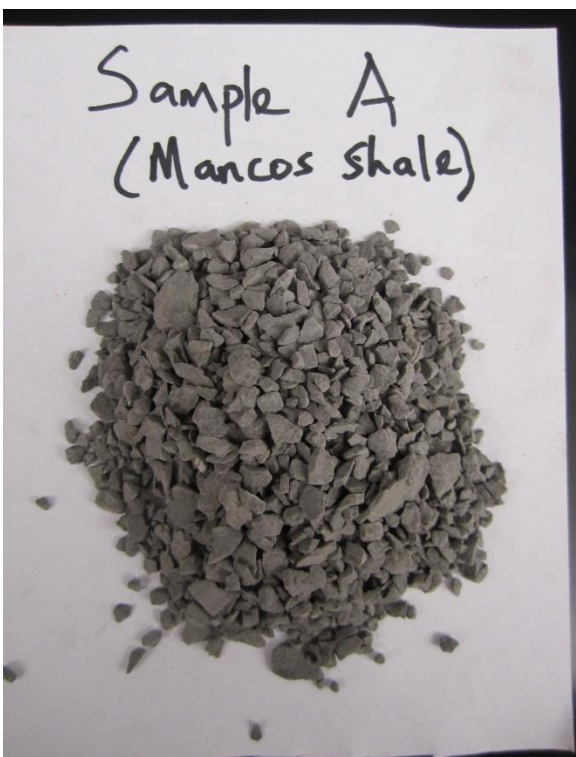


Figure A.9: Crushed shale samples, **pre-flooding** with CO₂-brine; Mancos



Figure A.10: Crushed shale samples, **pre-flooding** with CO₂-brine; Marcellus



Figure A.11: Crushed shale samples, **pre-flooding** with CO₂-brine; Pottsville

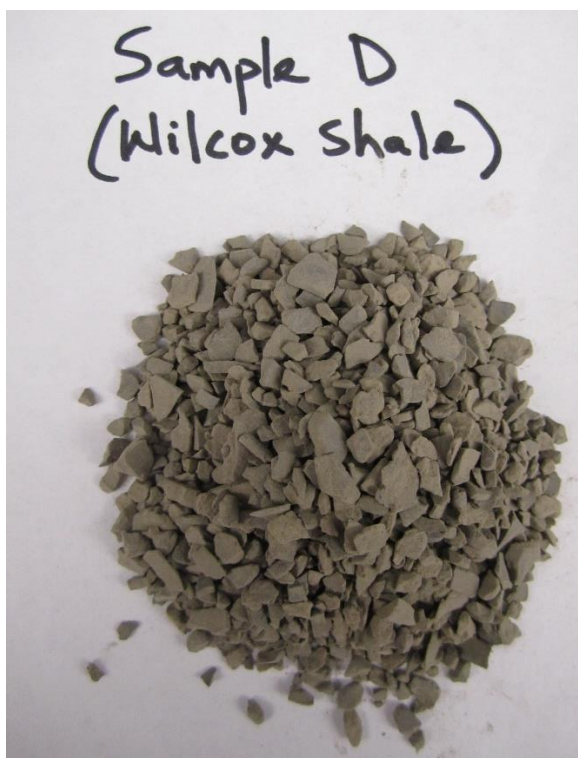


Figure A.12: Crushed shale samples, **pre-flooding** with CO₂-brine; Wilcox

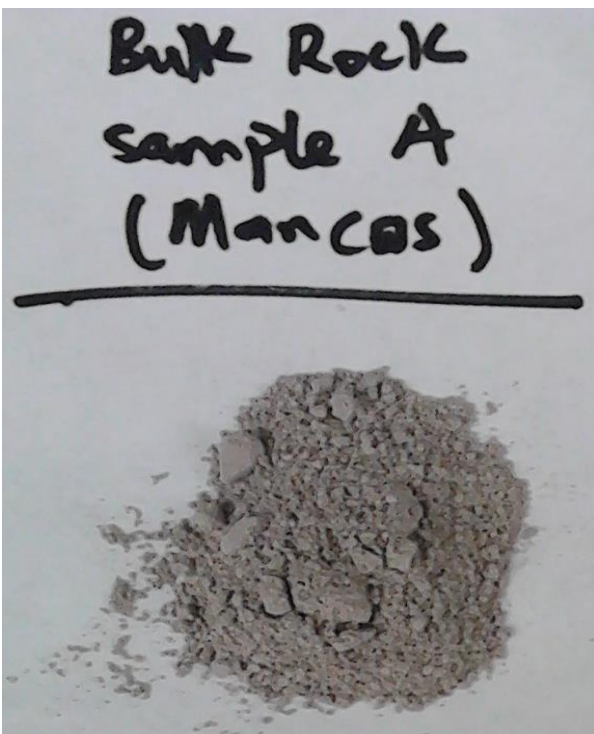


Figure A.13: Crushed shale samples, **post-flooding** with CO₂-brine; Mancos

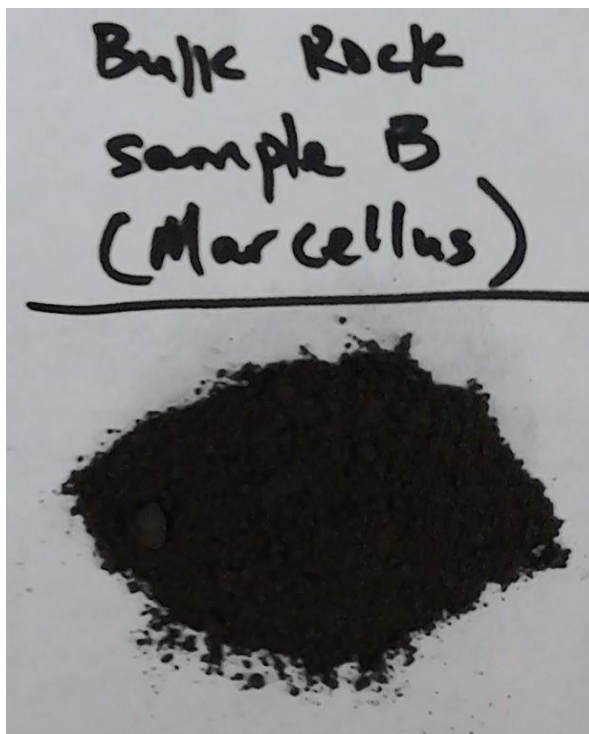


Figure A.14: Crushed shale samples, **post-flooding** with CO₂-brine; Marcellus

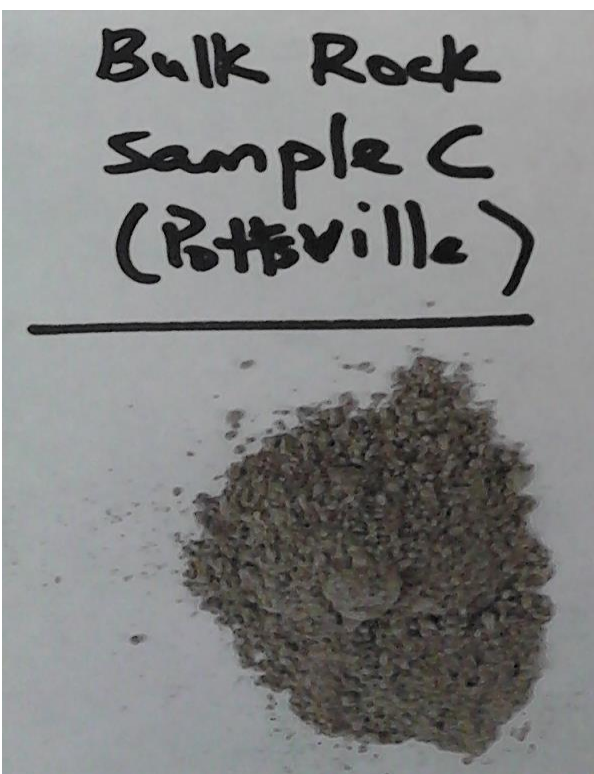


Figure A.15: Crushed shale samples, **post-flooding** with CO₂-brine; Pottsville

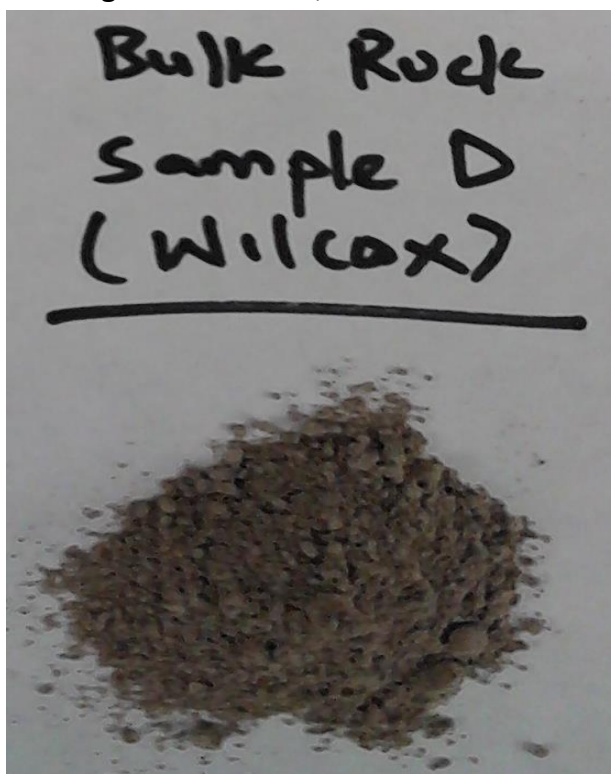


Figure A.16: Crushed shale samples, **post-flooding** with CO₂-brine; Wilcox

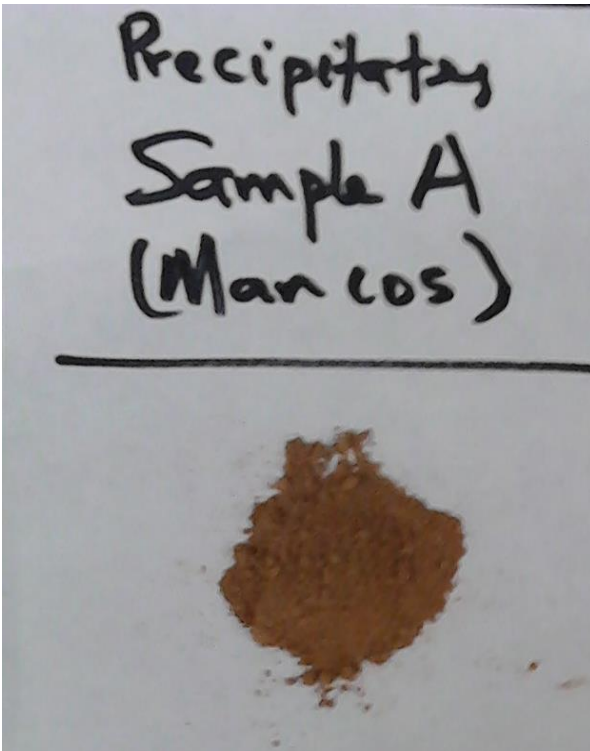


Figure A.17: Recovered effluent **precipitates**, post-flooding with CO₂-brine; Mancos

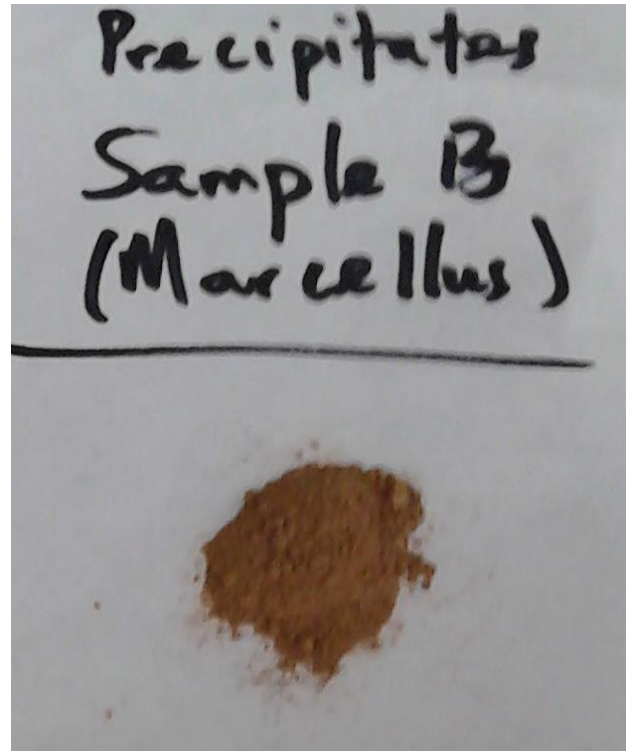


Figure A.18: Recovered effluent **precipitates**, post-flooding with CO₂-brine; Marcellus

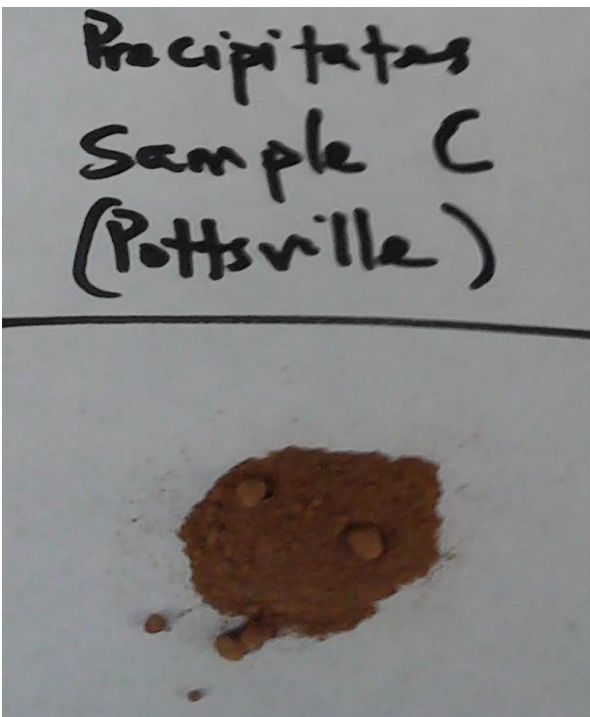


Figure A.19: Recovered effluent **precipitates**, post-flooding with CO₂-brine; Pottsville

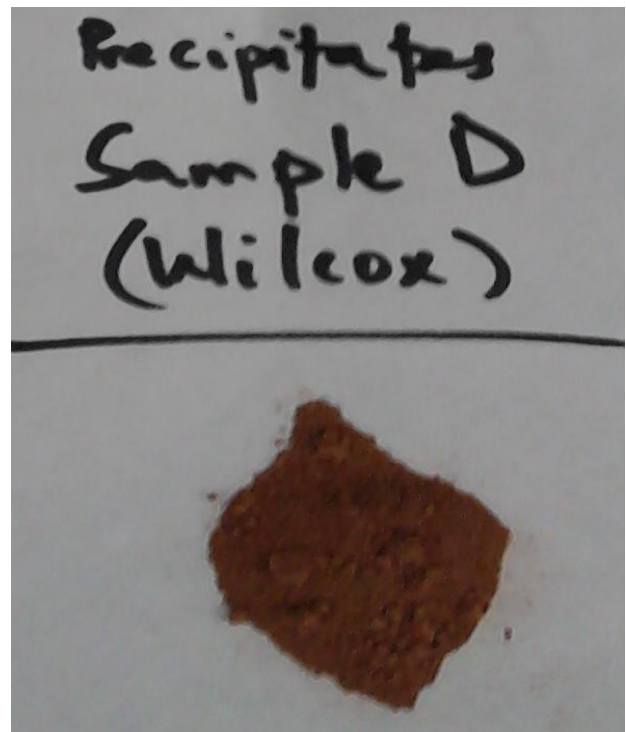


Figure A.20: Recovered effluent **precipitates**, post-flooding with CO₂-brine; Wilcox

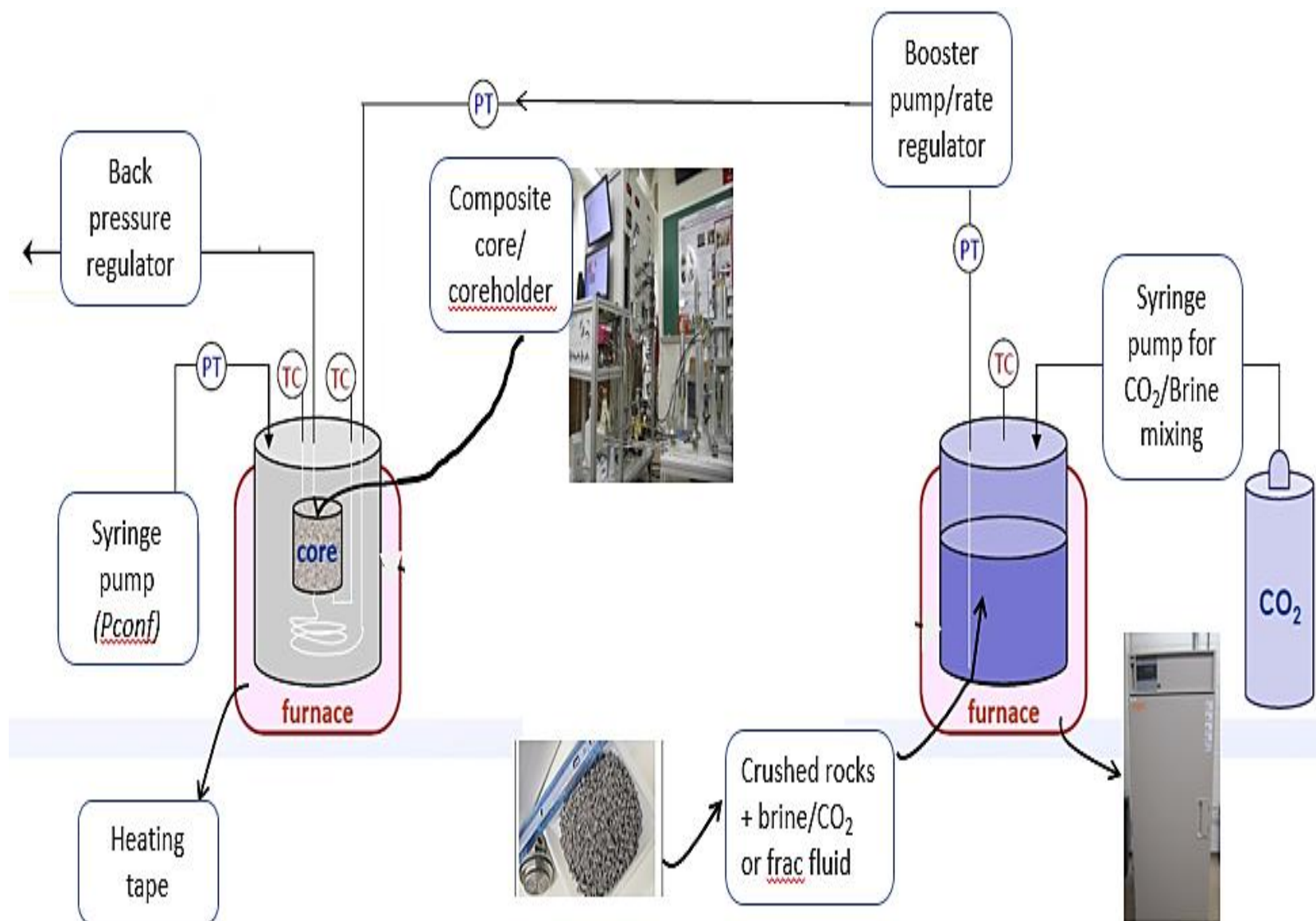


Figure A.21: Process schematics of experimental setup showing materials and equipment used for CO₂-brine flooding and composite core conductivity measurement.

APPENDIX B

EXPERIMENTAL PROCEDURE FOR ROCK-FLUID INTERACTION EXPERIMENTS

The following table and detailed description of steps summarizes the procedures used in conducting the shale rock – aqueous CO₂ interactions:

Table B.1: Pre-injection and Post-injection analysis for each CO₂-brine flooding run

Run X	Type of Analysis
Step 1	Flood crushed shale rock with CO ₂ -brine and transport effluent to composite core under varying axial and radial stress.
Step 2	Take real time measurement of differential pressure drop for changes in conductivity. This will be automatically acquired during injection and transport of CO ₂ -brine.
Step 3	Analyze final and intermediate effluent composition (pH, ICP-OES). Analyze crushed shale rock for morphology, mineral composition, total organic carbon composition and hardness (SEM, EDS, XRD, TOC, Micro-indentation).
Step 4	Measure effective fracture aperture and conductivity.
Step 5	Use geochemical results to bound overall chemo-fracture flow modelling in aqueous CO ₂ -shale interactions.

Description of a Single Experimental Run and the Associated Analyses

For a typical single run of the experiment, the two units of the experimental setup- the packed bed vessel and high pressure coreholder are opened up. The packed bed vessel is filled with sieved crushed shale rock samples up to 350g per experiment. The dimensions of the crushed

rock were about 2mm in diameter. The fractured core samples are placed in the high pressure coreholder and the two vessels capped afterwards. The high pressure coreholder has a heating tape around it for the maintenance of temperature and the packed bed vessel is placed in the oven with regulated temperature. The experiments were run at constant temperature of 50°C. The CO₂-brine reservoir is then connected to the pump for steady injection at 0.5ml/min. The injection pressure is gradually ramped up at 100psi/hr at the start. Minor trouble shootings such as trapped air bleeding and leakage points tightening are done. pH measurements are taken three times a day for each run. The stability of temperature is very important. Sometimes adjustments are made to the heating tape temperature which sometimes shoots above or below the set value. This is due to the analogue nature of the device. The differential pressure measurement is acquired at 15 to 20 sec rate. This yielded a wealth of differential pressure data points that can be averaged over the five day experimental period. These averaged data points are reported in the results and discussion sections for fracture flow characterization. All the effluent fluid is collected and stored for further analyses. Verification runs involving using only brine and/or unfractured cores were carried out to know the source of geochemical species. These runs confirmed that the unique geochemical responses are attributable to the shale rocks.

During the five days experimental run per shale type, one sample per day of the effluent fluid is taken and sent for ICP-OES analysis. This is to be able to obtain geochemical species within the fluid. The precipitates recovered from the effluents as well as the bulk rock were subjected to XRD analysis. The precipitates were fully recovered via concentrated sedimentation and room temperature dried. This is to ensure that no material damage was done to chemical components of the precipitates. About 10g of the post-flooding bulk rock are analysed with bulk and clay XRD

techniques. For total carbon content, about 5g of the rock samples are analysed. Special samples (1 inch cylindrical cuts of about 5mm thickness) which have been placed in the packed bed vessels for indentation analyses are recovered. These special tablets (1 inch diameter) are polished to reduce the impact of surface roughness on measured indentation values. Some of the cylindrical samples are used for thin section slides. These slides were used in data acquisition of surface morphology coupled with geochemical spread or maps (using EMPA technique).

APPENDIX C

pH DATA

Average= Average of six data points, SD= Standard Deviation

Time (days)	Mancos_Average pH	Mancos_SD
0	3.70	0.10
1	7.73	0.047
2	7.70	0.24
3	8.20	0.22
4	8.17	0.21
5	8.07	0.12
Time (days)	Marcellus_Average pH	Marcellus_SD
0	3.70	0.10
1	7.47	0.17
2	7.60	0.16
3	7.93	0.09
4	7.87	0.09
5	7.83	0.05
Time (days)	Pottsville_Average pH	Pottsville_SD
0	3.70	0.10
1	7.83	0.10
2	7.90	0.10
3	8.17	0.09
4	7.97	0.05
5	7.70	0.16
Time (days)	Wilcox_Average pH	Wilcox_SD
0	3.70	0.10
1	6.67	0.12
2	7.00	0.10
3	7.03	0.20
4	7.43	0.05
5	7.00	0.30

APPENDIX D

INDUCTIVELY COUPLED PLASMA EMISSION SPECTROSCOPY (ICP-OES) DATA

Samples No.	Al, ppm	As, ppm	B, ppm	Ca, ppm	Fe, ppm	Mg, ppm	Mn, ppm	Ni, ppm	P, ppm	K, ppm	Se, ppm	S, ppm	Zn, ppm
1(initial)	0.938	0.133	1.018	3.891	0.152	3.890	0.019	2.119	0.189	91.369	0.230	0.224	0.227
Samples No.	Al, ppm	As, ppm	B, ppm	Ca, ppm	Fe, ppm	Mg, ppm	Mn, ppm	Ni, ppm	P, ppm	K, ppm	Se, ppm	S, ppm	Zn, ppm
2	0.758	0.182	1.523	41.434	0.145	34.312	0.012	1.985	0.218	159.566	19.718	18.401	0.156
3	0.836	0.211	0.824	158.029	0.225	54.701	0.017	1.638	0.166	139.844	4.888	6.680	0.163
4	0.931	0.172	0.901	151.769	0.224	63.216	0.020	1.902	0.139	129.423	2.373	4.352	0.161
5	0.963	0.204	0.851	280.687	0.236	61.940	3.527	1.677	0.139	131.376	1.535	5.538	0.165
6	0.937	0.222	0.737	287.855	0.232	58.276	3.674	1.647	0.185	107.804	2.391	6.422	0.163
Samples No.	Al, ppm	As, ppm	B, ppm	Ca, ppm	Fe, ppm	Mg, ppm	Mn, ppm	Ni, ppm	P, ppm	K, ppm	Se, ppm	S, ppm	Zn, ppm
7	0.898	0.111	1.402	99.404	0.212	33.274	2.837	1.974	0.183	133.381	15.503	14.766	0.159
8	0.982	0.231	1.008	62.982	0.235	40.383	0.117	2.040	0.175	128.279	4.871	5.275	0.159
9	0.958	0.153	0.825	158.254	0.237	56.015	3.489	1.771	0.102	146.651	2.105	4.329	0.166
10	0.959	0.135	0.809	135.917	0.244	50.535	4.333	1.701	0.185	100.017	1.165	3.165	0.164
11	0.981	0.066	0.794	137.811	0.224	53.508	4.304	1.651	0.191	116.427	0.918	2.823	0.166
	Al, ppm	As, ppm	B, ppm	Ca, ppm	Fe, ppm	Mg, ppm	Mn, ppm	Ni, ppm	P, ppm	K, ppm	Se, ppm	S, ppm	Zn, ppm

Table Cont'd

12	0.943	0.212	0.783	170.567	0.064	16.609	2.381	1.911	0.197	136.113	11.133	12.307	0.165
13	0.969	0.138	0.838	190.773	0.231	14.309	0.721	1.925	0.158	146.863	6.718	9.065	0.169
14	0.943	0.120	0.727	110.283	0.228	4.929	0.331	1.926	0.134	110.789	2.503	4.009	0.179
15	0.955	0.063	0.622	121.485	0.218	2.533	0.506	1.940	0.138	131.005	1.592	3.148	0.173
16	0.784	0.202	0.885	136.905	0.226	1.423	0.488	1.891	0.187	130.773	1.307	3.024	0.189
Samples No.	Al, ppm	As, ppm	B, ppm	Ca, ppm	Fe, ppm	Mg, ppm	Mn, ppm	Ni, ppm	P, ppm	K, ppm	Se, ppm	S, ppm	Zn, ppm
17	0.992	0.131	1.385	299.766	0.209	155.486	0.026	1.913	0.214	149.931	264.710	252.782	0.180
18	0.850	0.299	0.965	250.543	0.226	43.309	0.154	2.021	0.192	131.438	42.562	43.913	0.170
19	0.925	0.078	0.891	181.867	0.215	19.395	0.179	2.045	0.177	133.871	14.157	15.090	0.170
20	0.861	0.171	0.507	139.011	0.212	11.346	0.130	2.062	0.139	122.004	4.360	5.965	0.182
21	0.936	0.204	0.834	142.500	0.215	7.519	0.179	2.089	0.191	114.017	2.688	4.499	0.183
Samples No.	Al, ppm	As, ppm	B, ppm	Ca, ppm	Fe, ppm	Mg, ppm	Mn, ppm	Ni, ppm	P, ppm	K, ppm	Se, ppm	S, ppm	Zn, ppm
22	0.982	0.117	1.331	341.123	0.216	129.537	0.569	1.964	0.152	133.875	214.068	204.079	0.180
23	0.971	0.105	0.669	280.464	0.241	54.869	0.276	2.021	0.139	143.070	44.862	46.500	0.174
24	0.963	0.160	0.709	124.545	0.234	29.227	0.026	2.076	0.176	113.514	8.541	9.695	0.170
25	0.903	0.113	0.760	231.745	0.222	26.108	0.239	1.966	0.170	133.517	3.840	7.110	0.170
26	0.974	0.223	0.672	224.777	0.230	25.617	0.222	2.043	0.128	127.760	2.930	5.811	0.165
Samples No.	Al, ppm	As, ppm	B, ppm	Ca, ppm	Fe, ppm	Mg, ppm	Mn, ppm	Ni, ppm	P, ppm	K, ppm	Se, ppm	S, ppm	Zn, ppm

Table Cont'd

27	1.005	0.160	1.422	439.562	0.228	163.691	0.544	1.892	0.119	184.273	249.904	238.647	0.173
28	0.955	0.196	0.909	332.542	0.219	43.471	0.321	2.021	0.162	115.198	22.512	25.968	0.167
29	0.980	0.103	0.732	254.728	0.230	33.583	0.299	2.053	0.128	111.499	13.009	15.231	0.169
30	0.972	0.183	0.700	225.436	0.225	35.698	0.235	2.056	0.169	97.375	6.199	9.094	0.171
31	0.792	0.182	0.565	170.797	0.218	29.904	0.372	1.914	0.281	110.092	23.395	24.581	0.184

APPENDIX E

MICRO-INDENTATION OF SHALE ROCKS DATA

Properties	Time(days)	Mancos	Marcellus	Pottsville	Wilcox
Vicker's Hardness	0	48.74	58.47	34.77	11.59
	5	30.56	54.61	36.18	7.39
Young's Modulus	0	13.29	17.12	17.24	4.19
	5	8.02	14.1	11.35	3.05

Rock Type	Original	SD_Original	Runs_AV	SD_Runs_AV
Mancos	48.74	3.19	30.56	4.28
Marcellus	58.47	3.27	54.61	4.39
Pottsville	34.77	1.18	36.18	6.33
Wilcox	11.59	1.01	7.39	1.16

APPENDIX F

ADDITIONAL DATA FOR ELECTRON MICROPROBE ANALYSIS (EMPA)

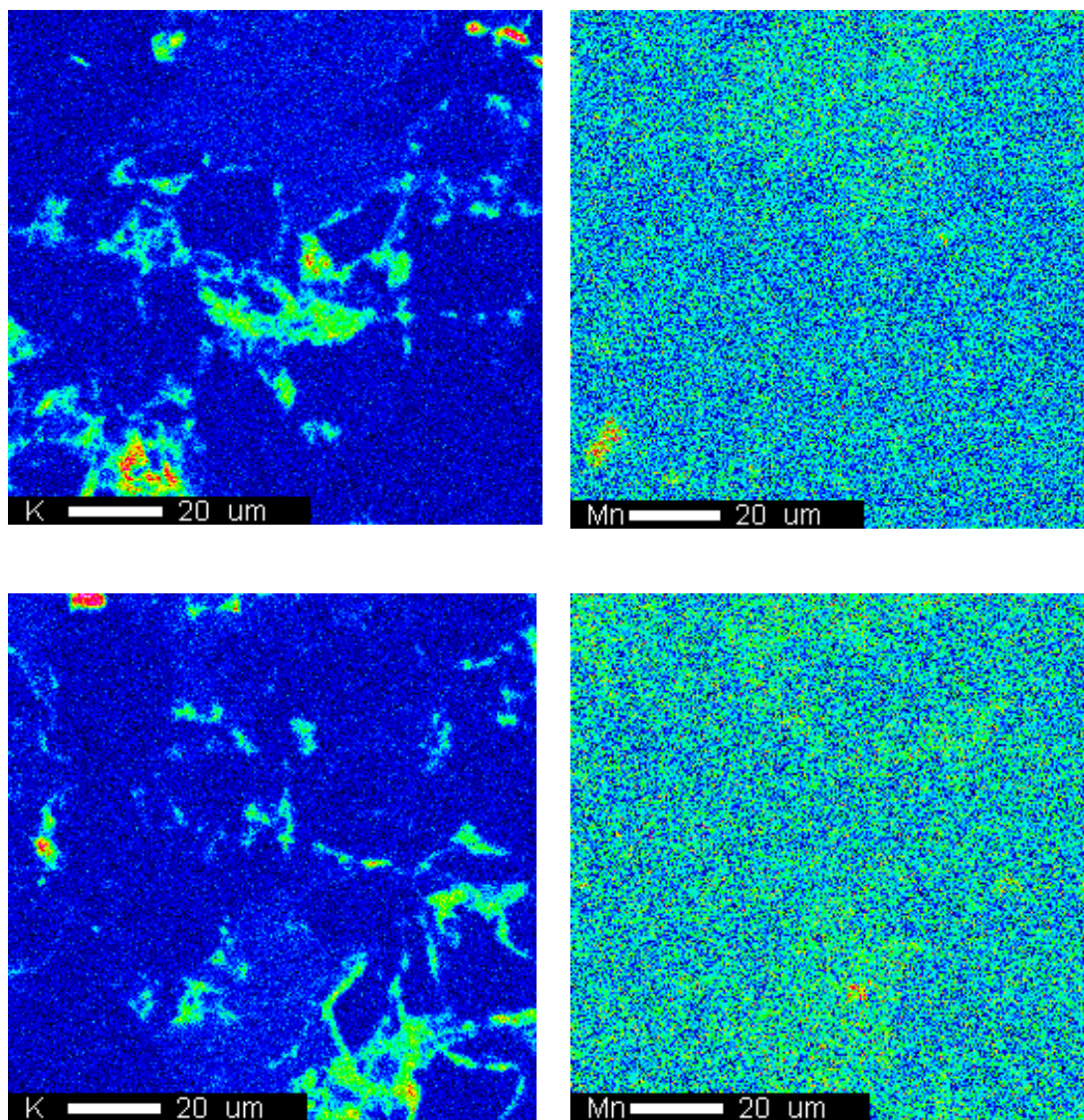


Figure G1: 20μm Electron Micro-Probe Analysis for **Mancos shale** showing **Potassium (K)** and **Manganese (Mn)** surface geochemical profile of the CO₂-reacted sample (top row) compared to control specimen (bottom row). Note the general depletion of elemental components that are associated with minerals that are susceptible to dissolution. These trends are only detected at the lower micron resolution presented above. The Scanning Electron Microscopy (SEM) back scatter image for these profiles is in **figure 4.25**.

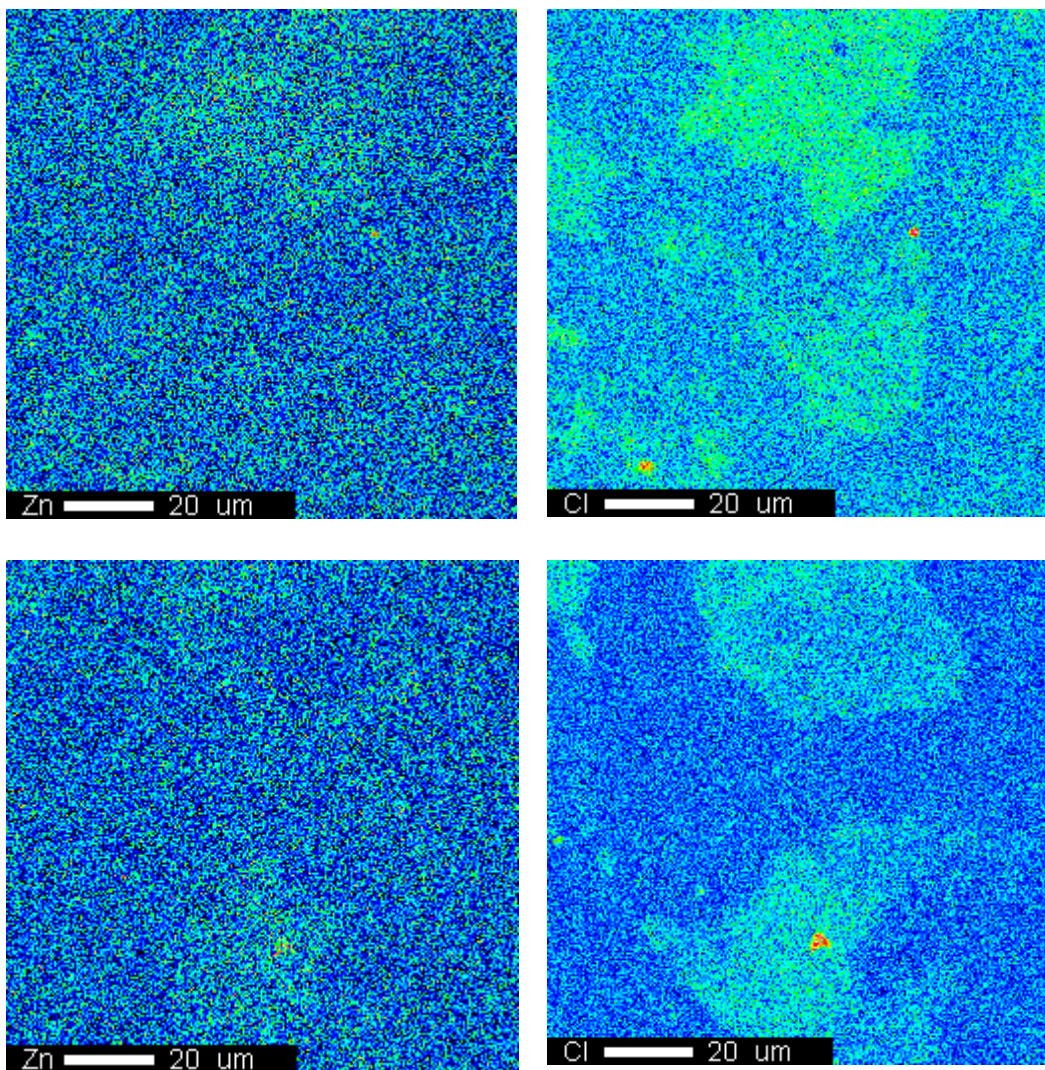


Figure G2: 20μm Electron Micro-Probe Analysis for **Mancos shale** showing **Zinc (Zn)** and **Chlorine (Cl)** surface geochemical profile of the CO₂-reacted sample (top row) compared to control specimen (bottom row). Note the general depletion of elemental components that are associated with minerals that are susceptible to dissolution. These trends are only detected at the lower micron resolution presented above. The Scanning Electron Microscopy (SEM) back scatter image for these profiles is in **figure 4.25**.

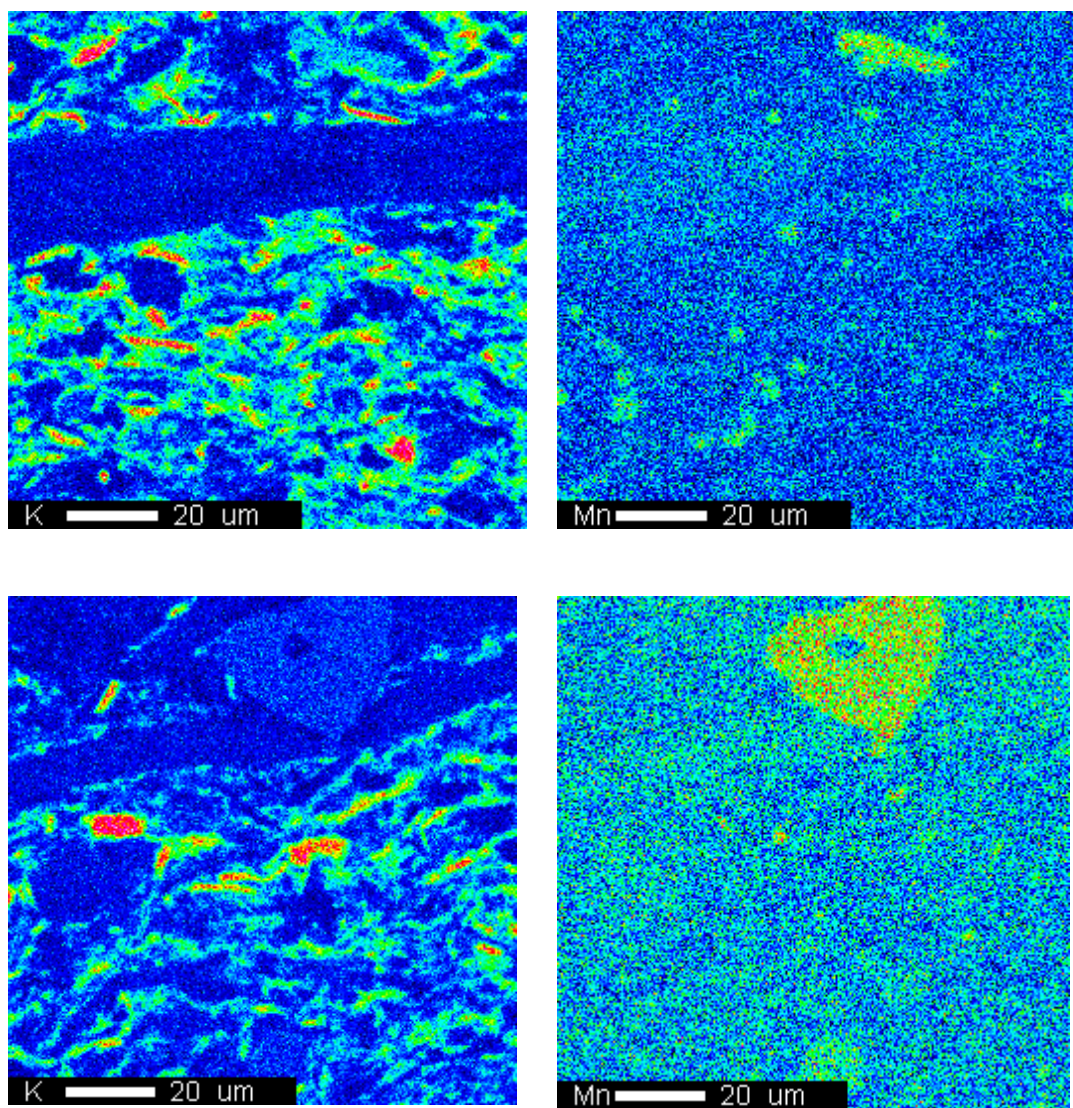


Figure G3: 20μm Electron Micro-Probe Analysis for **Marcellus shale** showing **Potassium (K)** and **Manganese (Mn)** surface geochemical profile of the CO₂-reacted sample (top row) compared to control specimen (bottom row). Note the general depletion of elemental components that are associated with minerals that are susceptible to dissolution. These trends are only detected at the lower micron resolution presented above. The Scanning Electron Microscopy (SEM) back scatter image for these profiles is in **figure 4.28**.

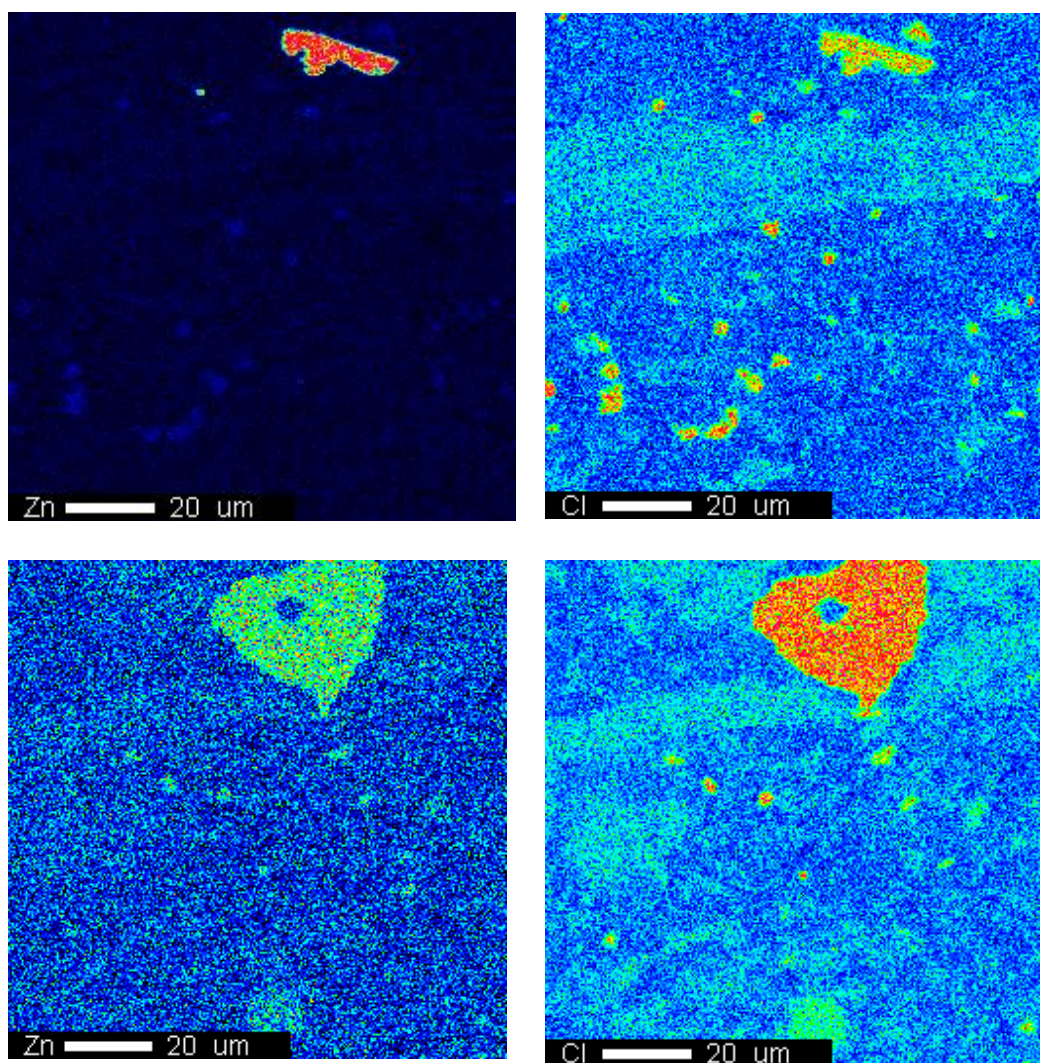


Figure G4: 20μm Electron Micro-Probe Analysis for **Marcellus shale** showing **Zinc (Zn)** and **Chlorine (Cl)** surface geochemical profile of the CO₂-reacted sample (top row) compared to control specimen (bottom row). Note the general depletion of elemental components that are associated with minerals that are susceptible to dissolution. These trends are only detected at the lower micron resolution presented above. The Scanning Electron Microscopy (SEM) back scatter image for these profiles is in **figure 4.28**.

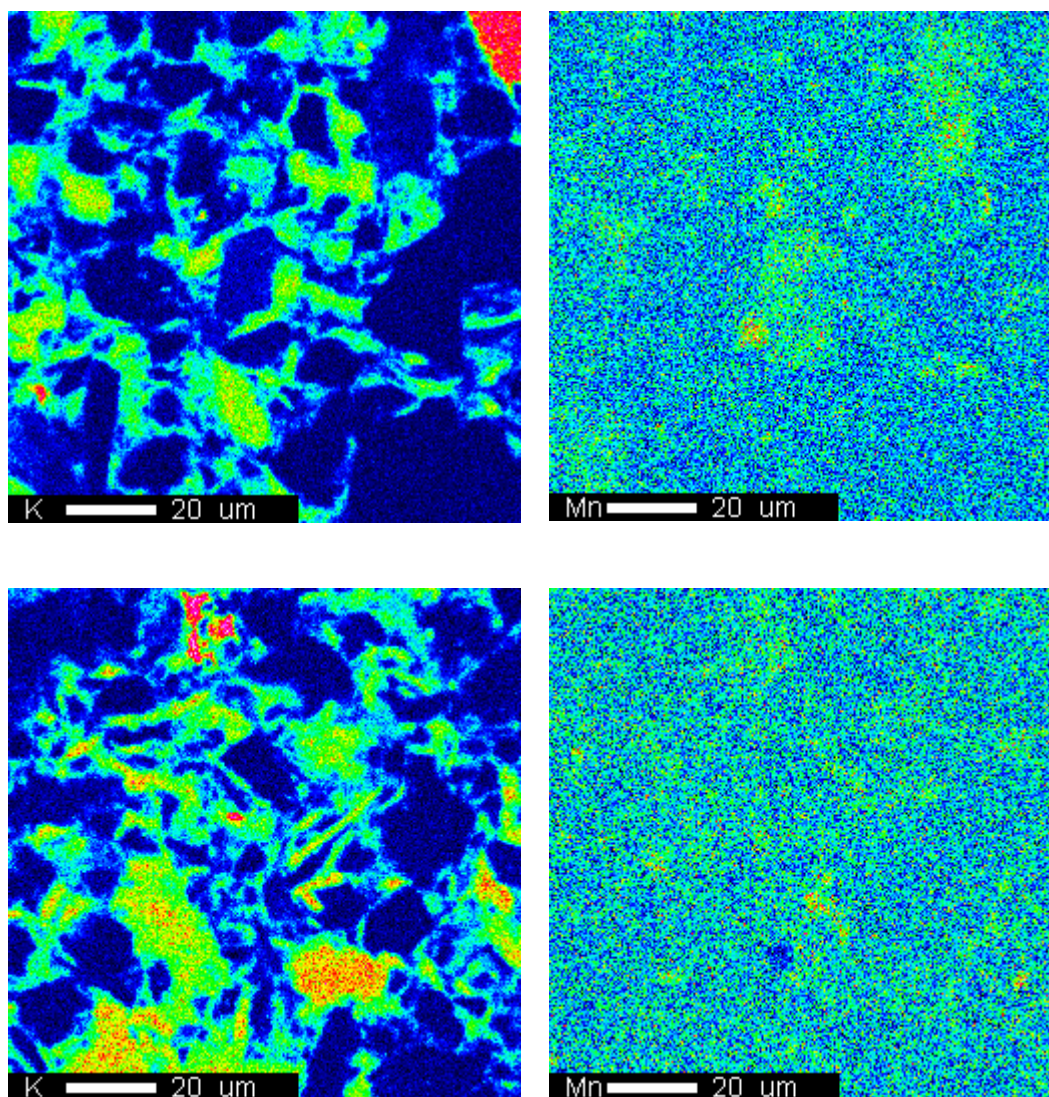


Figure G5: 20μm Electron Micro-Probe Analysis for **Pottsville shale** showing **Potassium (K)** and **Manganese (Mn)** surface geochemical profile of the CO₂-reacted sample (top row) compared to control specimen (bottom row). Note the general depletion of elemental components that are associated with minerals that are susceptible to dissolution. These trends are only detected at the lower micron resolution presented above. The Scanning Electron Microscopy (SEM) back scatter image for these profiles is in **figure 4.31**.

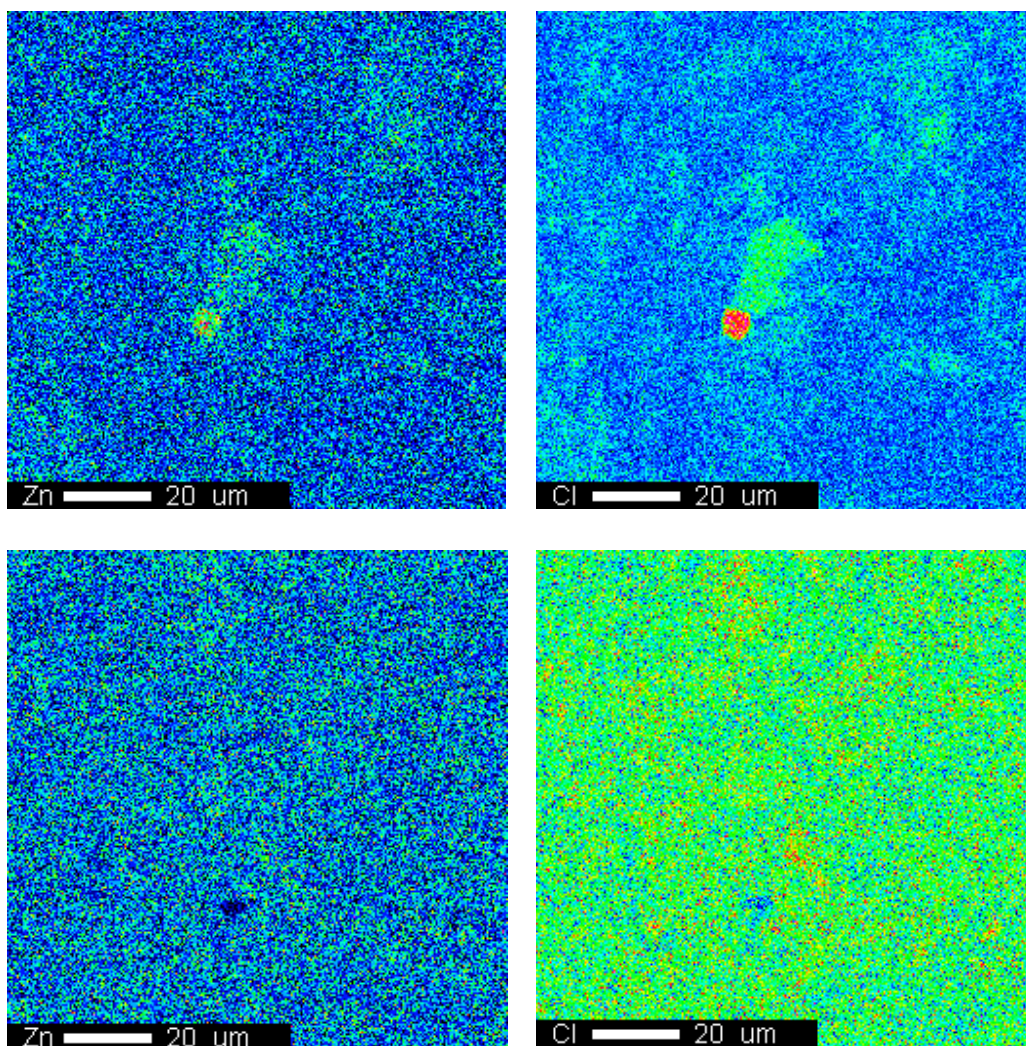


Figure G6: 20µm Electron Micro-Probe Analysis for **Pottsville shale** showing **Zinc (Zn)** and **Chlorine (Cl)** surface geochemical profile of the CO₂-reacted sample (top row) compared to control specimen (bottom row). Note the general depletion of elemental components that are associated with minerals that are susceptible to dissolution. These trends are only detected at the lower micron resolution presented above. The Scanning Electron Microscopy (SEM) back scatter image for these profiles is in **figure 4.31**.

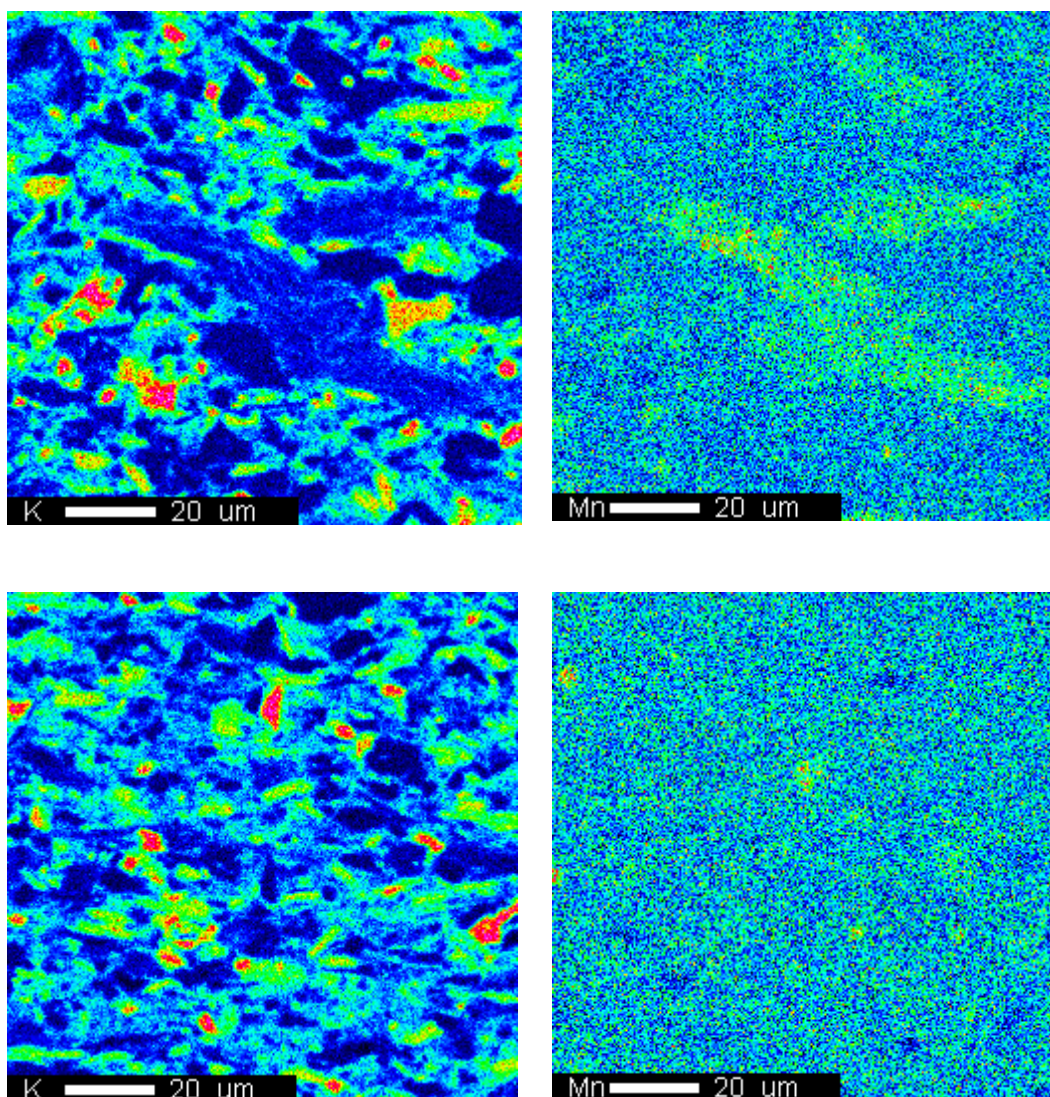


Figure G7: 20μm Electron Micro-Probe Analysis for **Wilcox shale** showing **Potassium (K)** and **Manganese (Mn)** surface geochemical profile of the CO₂-reacted sample (top row) compared to control specimen (bottom row). Note the general depletion of elemental components that are associated with minerals that are susceptible to dissolution. These trends are only detected at the lower micron resolution presented above. The Scanning Electron Microscopy (SEM) back scatter image for these profiles is in **figure 4.34**.

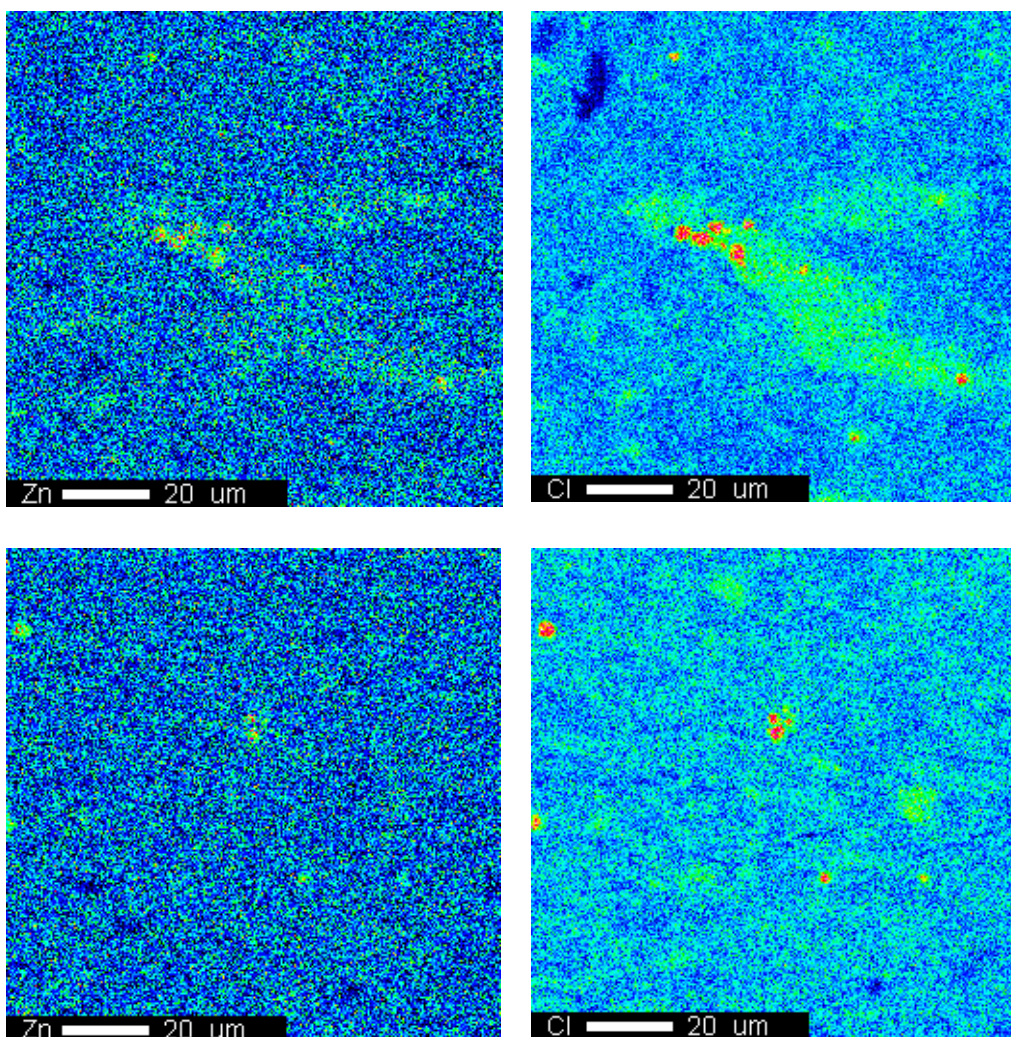


Figure G8: 20µm Electron Micro-Probe Analysis for **Wilcox shale** showing **Zinc (Zn)** and **Chlorine (Cl)** surface geochemical profile of the CO₂-reacted sample (top row) compared to control specimen (bottom row). Note the general depletion of elemental components that are associated with minerals that are susceptible to dissolution. These trends are only detected at the lower micron resolution presented above. The Scanning Electron Microscopy (SEM) back scatter image for these profiles is in **figure 4.34**.

APPENDIX G

FLOW/PRESSURE DATA

Table G.1: Data for differential pressure, dP (psi) across **25µm** fractured core(s) for flow-through experiment using **Mancos shale**.

Time (days)	Run1	Run2	Run3	Average	Standard Deviation
0.00	58.71	29.34	30.90	39.65	13.49
0.25	77.47	34.40	40.24	50.70	19.08
0.50	95.19	152.69	52.59	100.16	41.01
0.75	132.36	153.07	177.63	154.35	18.50
1.00	140.74	154.47	185.84	160.35	18.88
1.25	172.88	156.90	186.99	172.26	12.29
1.50	174.86	157.41	189.98	174.09	13.31
1.75	180.40	159.08	190.12	176.53	12.96
2.00	180.48	159.15	190.67	176.76	13.13
2.25	181.56	163.86	191.70	179.04	11.50
2.50	183.05	166.88	191.78	180.57	10.32
2.75	183.59	168.71	192.84	181.72	9.94
3.00	183.93	170.48	192.86	182.42	9.20
3.25	184.88	171.61	193.17	183.22	8.88
3.50	185.65	173.94	193.52	184.37	8.04
3.75	186.63	175.45	194.17	185.42	7.69
4.00	188.26	176.86	194.45	186.52	7.29
4.25	188.76	177.07	195.19	187.01	7.50
4.50	189.18	178.52	195.84	187.85	7.13
4.75	190.03	179.97	196.46	188.82	6.78
5.00	192.00	181.10	196.49	189.86	6.46

Table G.2: Data for differential pressure, dP (psi) across **25µm** fractured core(s) for flow-through experiment using **Marcellus shale**.

Time (days)	Run1	Run2	Run3	Average	Standard Deviation
0.00	158.92	131.91	163.16	151.33	13.84
0.25	159.02	172.53	163.25	164.93	5.64
0.50	176.55	172.62	172.18	173.78	1.97
0.75	177.33	178.09	172.52	175.98	2.47
1.00	178.29	178.42	175.22	177.31	1.48
1.25	178.69	178.62	178.52	178.61	0.07
1.50	178.72	178.65	180.00	179.12	0.62
1.75	179.64	179.09	181.88	180.20	1.21
2.00	179.97	179.86	183.66	181.17	1.77
2.25	180.25	181.42	184.99	182.22	2.02
2.50	180.94	181.46	187.02	183.14	2.75
2.75	181.73	181.51	187.10	183.45	2.58
3.00	182.39	182.55	187.79	184.25	2.51
3.25	182.50	182.64	187.98	184.37	2.55
3.50	182.77	183.21	189.16	185.05	2.91
3.75	183.30	183.58	189.31	185.40	2.77
4.00	184.89	184.10	189.83	186.27	2.53
4.25	185.25	184.49	193.29	187.68	3.98
4.50	185.96	184.96	193.86	188.26	3.98
4.75	185.98	185.42	195.11	188.83	4.44
5.00	187.33	186.42	197.24	190.33	4.90

Table G.3: Data for differential pressure, dP (psi) across **25µm** fractured core(s) for flow-through experiment using **Pottsville shale**.

Time (days)	Run1	Run2	Run3	Average	Standard Deviation
0.00	41.89	41.89	32.55	38.78	4.40
0.25	85.83	85.83	118.89	96.85	15.58
0.50	99.79	99.79	121.19	106.93	10.09
0.75	125.53	125.53	137.63	129.56	5.70
1.00	126.54	126.54	157.07	136.72	14.39
1.25	126.84	126.84	164.56	139.41	17.78
1.50	128.18	128.18	166.09	140.81	17.87
1.75	128.35	128.35	167.68	141.46	18.54
2.00	128.96	128.96	168.34	142.09	18.56
2.25	129.45	129.45	168.49	142.47	18.40
2.50	130.22	130.22	168.58	143.01	18.08
2.75	147.43	147.43	169.07	154.65	10.20
3.00	147.68	147.68	169.30	154.88	10.19
3.25	148.83	148.83	169.59	155.75	9.79
3.50	149.65	149.65	170.37	156.56	9.77
3.75	149.69	149.69	172.03	157.14	10.53
4.00	150.23	150.23	172.73	157.73	10.60
4.25	150.78	150.78	172.90	158.15	10.43
4.50	152.48	152.48	175.72	160.22	10.95
4.75	153.50	153.50	175.98	160.99	10.60
5.00	154.35	154.35	177.79	162.17	11.05

Table G.4: Data for differential pressure, dP (psi) across **25µm** fractured core(s) for flow-through experiment using **Wilcox shale**.

Time (days)	Run1	Run2	Run3	Average	Standard Deviation
0.00	33.00	65.00	95.35	64.45	25.46
0.25	55.57	92.51	132.29	93.46	31.33
0.50	70.02	93.07	132.40	98.50	25.75
0.75	88.35	94.76	132.48	105.20	19.47
1.00	108.34	126.32	132.56	122.41	10.27
1.25	116.50	126.89	132.67	125.35	6.69
1.50	120.75	131.84	132.77	128.45	5.46
1.75	121.69	140.15	132.87	131.57	7.59
2.00	124.95	150.25	132.99	136.06	10.55
2.25	143.06	152.59	133.41	143.02	7.83
2.50	143.51	153.17	139.45	145.38	5.75
2.75	157.23	158.46	139.91	151.87	8.47
3.00	163.60	158.99	141.91	154.84	9.33
3.25	164.59	160.21	143.64	156.15	9.02
3.50	164.90	170.15	143.90	159.65	11.34
3.75	166.16	171.86	147.42	161.81	10.44
4.00	167.47	173.48	165.33	168.76	3.45
4.25	167.75	173.74	166.63	169.37	3.12
4.50	172.22	178.07	166.82	172.37	4.59
4.75	176.49	180.72	169.39	175.53	4.68
5.00	179.42	180.83	170.63	176.96	4.51

Table G.5: Data for differential pressure, dP (psi) across **150 μ m** fractured core(s) for flow-through experiment using **Mancos shale**.

Time (days)	Run1	Run2	Run3	Average	Standard Deviation
0.00	23.78	21.48	25.88	23.72	5.40
0.25	36.95	34.65	39.05	36.88	7.63
0.50	56.63	54.33	58.73	56.56	8.20
0.75	82.37	80.07	84.47	82.30	7.40
1.00	103.23	100.93	105.33	103.16	7.55
1.25	110.11	107.81	112.21	110.05	4.92
1.50	114.98	112.68	117.08	114.91	5.32
1.75	122.99	120.69	125.09	122.92	5.19
2.00	125.74	123.44	127.84	125.67	5.25
2.25	129.78	127.48	131.88	129.72	4.60
2.50	131.06	128.76	133.16	130.99	4.13
2.75	133.09	130.79	135.19	133.02	3.98
3.00	134.64	132.34	136.74	134.57	3.68
3.25	136.49	134.19	138.59	136.42	3.55
3.50	137.10	134.80	139.20	137.03	3.22
3.75	137.67	135.37	139.77	137.60	3.08
4.00	140.27	137.97	142.37	140.20	2.91
4.25	140.60	138.30	142.70	140.53	3.00
4.50	142.00	139.70	144.10	141.93	2.85
4.75	143.50	141.20	145.60	143.43	2.71
5.00	145.70	143.40	147.80	145.63	2.58

Table G.6: Data for differential pressure, dP (psi) across **150 μ m** fractured core(s) for flow-through experiment using **Marcellus shale**.

Time (days)	Run1	Run2	Run3	Average	Standard Deviation
0.00	32.81	30.92	34.52	32.75	6.92
0.25	52.25	50.36	53.96	52.19	7.90
0.50	91.80	89.91	93.51	91.74	2.75
0.75	127.10	125.21	128.81	127.04	3.45
1.00	135.08	133.19	136.79	135.02	2.07
1.25	139.68	137.79	141.39	139.62	1.28
1.50	143.17	141.28	144.88	143.11	1.29
1.75	144.10	142.21	145.81	144.04	1.69
2.00	145.30	143.41	147.01	145.24	2.47
2.25	146.70	144.81	148.41	146.64	2.83
2.50	147.20	145.31	148.91	147.14	3.86
2.75	148.90	147.01	150.61	148.84	3.61
3.00	149.10	147.21	150.81	149.04	3.51
3.25	149.80	147.91	151.51	149.74	3.57
3.50	149.90	148.01	151.61	149.84	4.08
3.75	150.30	148.41	152.01	150.24	3.87
4.00	150.50	148.61	152.21	150.44	3.55
4.25	150.60	148.71	152.31	150.54	5.57
4.50	150.90	149.01	152.61	150.84	5.58
4.75	151.30	149.41	153.01	151.24	6.22
5.00	151.60	149.71	153.31	151.54	6.86

Table G.7: Data for differential pressure, dP (psi) across **150 μ m** fractured core(s) for flow-through experiment using **Pottsville shale**.

Time (days)	Run1	Run2	Run3	Average	Standard Deviation
0.00	27.28	24.23	29.95	27.15	2.20
0.25	42.50	39.45	45.17	42.37	7.79
0.50	68.18	65.13	70.85	68.06	5.04
0.75	88.72	85.67	91.39	88.60	2.85
1.00	97.55	94.50	100.22	97.43	7.20
1.25	103.40	100.35	106.07	103.28	8.89
1.50	108.55	105.50	111.22	108.42	8.94
1.75	110.22	107.17	112.89	110.09	9.27
2.00	111.40	108.35	114.07	111.27	9.28
2.25	111.90	108.85	114.57	111.77	9.20
2.50	113.00	109.95	115.67	112.87	9.04
2.75	113.80	110.75	116.47	113.67	5.10
3.00	114.30	111.25	116.97	114.17	5.10
3.25	114.90	111.85	117.57	114.77	4.89
3.50	115.50	112.45	118.17	115.37	4.89
3.75	115.90	112.85	118.57	115.77	5.26
4.00	116.20	113.15	118.87	116.07	5.30
4.25	116.80	113.75	119.47	116.67	5.21
4.50	117.50	114.45	120.17	117.37	5.48
4.75	117.80	114.75	120.47	117.67	5.30
5.00	118.00	114.95	120.67	117.87	5.52

Table G.8: Data for differential pressure, dP (psi) across **150 μ m** fractured core(s) for flow-through experiment using **Wilcox shale**.

Time (days)	Run1	Run2	Run3	Average	Standard Deviation
0.00	25.78	24.54	27.89	26.07	14.76
0.25	39.03	37.79	41.14	39.32	9.40
0.50	65.40	64.16	67.51	65.69	14.94
0.75	87.00	85.76	89.11	87.29	11.29
1.00	91.94	90.70	94.05	92.23	5.96
1.25	94.30	93.06	96.41	94.59	3.88
1.50	95.74	94.50	97.85	96.03	3.17
1.75	99.25	98.01	101.36	99.54	4.40
2.00	100.94	99.70	103.05	101.23	6.12
2.25	102.00	100.76	104.11	102.29	4.54
2.50	103.90	102.66	106.01	104.19	3.34
2.75	105.00	103.76	107.11	105.29	4.91
3.00	106.40	105.16	108.51	106.69	5.41
3.25	107.10	105.86	109.21	107.39	5.23
3.50	108.00	106.76	110.11	108.29	6.58
3.75	108.50	107.26	110.61	108.79	6.05
4.00	108.90	107.66	111.01	109.19	2.00
4.25	109.70	108.46	111.81	109.99	1.81
4.50	110.10	108.86	112.21	110.39	2.66
4.75	111.00	109.76	113.11	111.29	2.71
5.00	111.90	110.66	114.01	112.19	2.62

APPENDIX H

FRACTURE CONDUCTIVITY DATA AND CALCULATIONS

Table H.1: Steps, equations and assumptions were made in calculating the fracture conductivity of the cores used during the experiments.

Steps	Equations	Assumptions
1. Put averaged values of dP from three experiments /per core in tabular form.	$k_f = 8.45 \times 10^9 w_f^2$	1. Flow is primarily through fractures
2. Declare and specify parameters (in approximate units) such as viscosity, fracture length, flow rate	$k_f = \frac{k_{av}A - k_m(A - w_f l)}{w_f l}$ $8.45 \times 10^9 w_f^3 l - k_{av}A + k_m(A - w_f l) = 0$	2. Bulk fracture flow properties are captured in the experimental differential pressure measurements
3. Calculate average fracture width from experimental data	$q_m = \frac{k_m A \Delta P}{\mu L}$	3. CO ₂ -brine viscosity is constant throughout the experiment
4. Estimate dimensionless fracture conductivity over time from fracture width and fracture length using the relationship shown in the list of equations	$q_f = 9.86 \times 10^9 \frac{w_f^3 l \Delta P}{12 \mu L_f}$ $w_f k_f = \pi C_r k L_f$ $w_f = \sqrt[3]{\frac{q_f \times 12 \mu}{9.86 \times 10^9 \Delta P}}$ $C_r = \frac{w_f k_f}{\pi K_{av} L_f} \approx \frac{w_f}{\pi L_f}$	4. Length of the core(s), for each experimental run, approximates the fracture length. 5. Tortuosity of fracture geometry is unity 6. Effect of fracture surface roughness is negligible 7. Microtubes are made of polymeric materials (PEEK), does not interfere at all with dissolution-precipitation process

VITA

Abiola Olabode is the third child of a family of three children. He attended Government College Ibadan and Command Day Secondary School Odogbo for his secondary education. He later proceeded to Obafemi Awolowo University, Ile Ife where in 2008, he earned a Bachelor's degree in Chemical Engineering with honors. Abiola worked with Pan Ocean Oil Corporation in Lagos, Nigeria between 2008 and 2010 as a natural gas Process Engineer helping with the design of multi-stage NGL recovery systems. He joined the graduate program of the Craft & Hawkins Department of Petroleum Engineering in 2010 and obtained a Master of Science degree with Thesis in December 2012. His doctoral program began in January of 2013. He has co-authored several peer-reviewed research articles and conference papers during his graduate studies (<https://scholar.google.com/citations?user=TrkUbtQAAAAJ&hl=en>).